Failure Inducing Features at Lithium Battery Interfaces

Submitted in partial fulfillment of the requirements for

the degree of

Doctor of Philosophy

in

Materials Science and Engineering

Sarah Linnell Frisco

B.S., Chemistry Department, Rochester Institute of Technology
M.S., Materials Science and Engineering Department, Carnegie Mellon University

Carnegie Mellon University
Pittsburgh PA

February, 2019

ACKNOWLEDGEMENTS

I would like to thank my co-advisors, Jay Whitacre and Shawn Litster, for their support and guidance over the years. Having their dual perspectives on my work has challenged me to continually broaden my understanding. Further thanks are owed to my thesis committee, Christopher Bettinger, B. Reeja Jayan, and Chris Pistorius. I greatly appreciate your time and feedback during this process.

Research can be a very isolating task, but I have been buoyed by the great lab mates I've had here. Particularly Alex and Pratiti, who were instrumental in helping me getting started in my first year. The labs have expanded significantly since then, so I also have to thank Sneha, Han, Paul, Jon, Leiming, and a continually growing list of others that I get to interact with. Thanks for the conversations, the collaborations, and the laughs.

Thanks to my family, who let batteries into their lives. Thanks to my found family of friends here in Pittsburgh and beyond for making these years rich. Thanks to my partner, Cassie, for supporting me. Thanks to Julia for everything, but also for promising to at least skim this document one day. Big picture, thanks to all the marginalized people who worked to expand access to STEM. I'll do everything I can to open the door for more people to come after me.

This work was made possible through the support of the Naval Research Laboratory, and a Seed Grant from Carnegie Mellon's Scott Institute for Energy Innovation and an ARPA-E award under the IONICS program. The acquisition of the nano-CT was supported by the National Science Foundation under grant No. 1229090.

ABSTRACT

Next generation rechargeable lithium metal battery chemistries have the potential to revolutionize energy storage. However, they remain stymied by the same potentially catastrophic failure mechanisms that caused the lithium metal anode to be removed from commercial rechargeable batteries in the first place: the formation of the solid electrolyte interphase (SEI) and dendritic lithium growth. This document is concerned with characterizing the morphology of these failure modes and implementing new strategies in their prevention. Here, we investigated a cycled graphite anode and found that the build-up of SEI could be seen not only clogging the surface of the electrode, but also closing the internal pores. Additionally, lithium electrodes cycled at varying temperatures and current densities show significantly different internal void morphology, which affects the dendrite deposition volume. A challenge in characterizing lithium failure in general and dendrites in particular is that there is no established set of conditions at which cells are meant to be tested in order to observe their growth or test prevention strategies. A proposed method of standardization was created in the form of a baseline of bare lithium performance at particular temperatures and current densities. Rather than test long term cycling, this baseline measured the extent of stable lithium deposition before signs of dendritic growth were observed. This metric has the advantage of being quick and accessible to any lab involved in electrochemical testing. Its viability as a means of predicting cell cyclability was tested by comparing the performance of different polymer coatings on the lithium electrodes. An increase in the extent of stable lithium deposition occurred in parallel to increased long term cycling performance.

Table of Contents

LIST OF TABLES

LIST OF FIGURES

1. Introduction

1.1 Motivation

Rechargeable lithium ion batteries have been instrumental in the proliferation of personal electronic devices and are at the forefront of development in the hybrid transportation and renewable energy storage fields. Lead acid batteries have historically been used in transportation due to their low cost and durability, but are an unlikely candidate for fully electric or even hybrid vehicles due to their poor cyclability – not to mention their toxicity[10]. Nickel based batteries can be costly and also suffer from relatively poor cycle life and toxicity issues[10]. The leftmost section of Figure 1.1 looks more specifically at currently available chemistries in terms of the distance that a battery pack could power an electric vehicle and what such a battery pack would cost, as calculated by Bruce et al based on a model of the Nissan Leaf[1]. Compared to these other established battery technologies, Li-ion batteries are desirable for their high energy density and efficiency; however, they are not without their faults. When discussing which battery chemistries to develop, one must take a balance of safety, performance and cost into consideration.

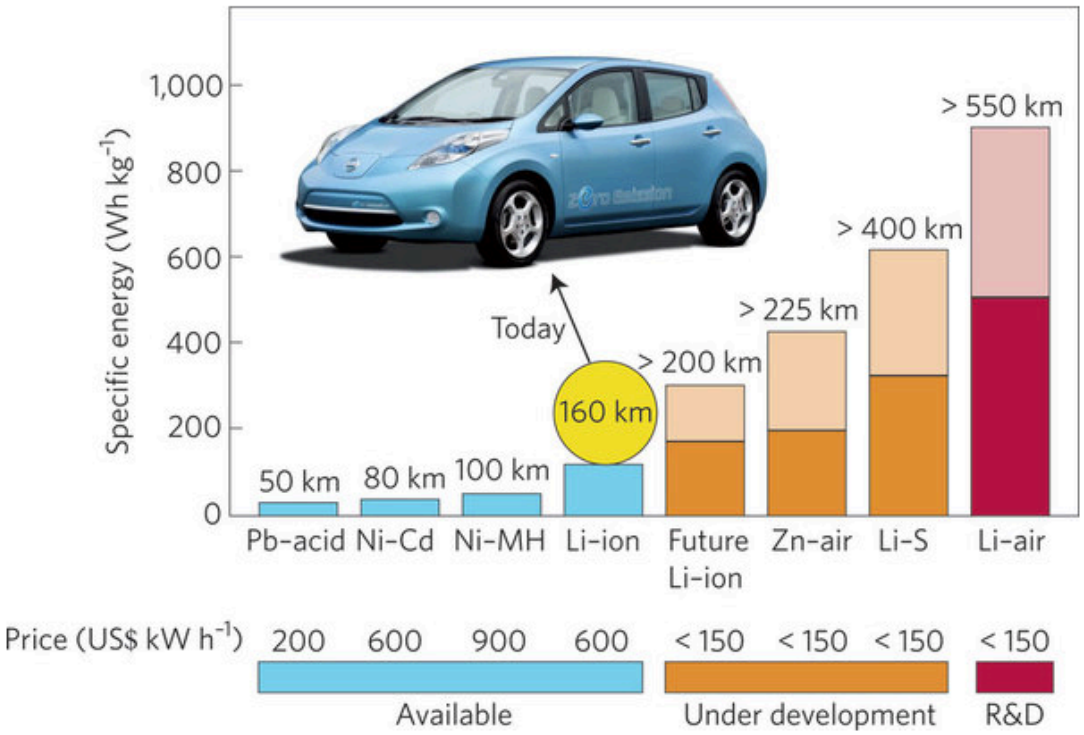

Figure 1.1. Driving range and cost of current and projected battery technologies, relative to the specific energy of Li-ion cells and the range of the Nissan Leaf, from Bruce et al.[1]. For the technologies still under development there is a potential range of predicted specific energies, which is represented by the lighter shaded area of those bars.

The first attempt to commercialize lithium batteries with solid lithium metal anodes had to be discontinued after multiple field failures occurred as a result of the formation of dendrites, which internally short-circuited the batteries and resulted in catastrophic failure[11]. Current commercial lithium ion batteries use inactive storage frameworks (e.g. graphite) for the electrochemically active lithium. This results in a lower overall energy density of the cell in exchange for dendrite growth being significantly less likely under most conditions, due to the fact that lithium is stored as the less reactive Li_xC_6 instead of deposited as solid lithium[11, 12]. Unfortunately, dendrites and, consequently, internal short

circuits can still occur on graphite anodes at higher charging rates and lower temperatures[5, 13], which limits the incorporation of lithium batteries into technologies that demand faster charging and more versatile performance.

Even in more moderate conditions of temperature and charging rates, limitations still exist to lithium ion battery lifetime performance. The standard nonaqueous electrolyte in Li-ion batteries operates across a voltage range that surpasses its thermodynamically stable range, which results in various species from the electrolyte reducing on the surface of the electrodes, particularly the anode[14]. The formation of these reduced species, collectively referred to as the Solid Electrolyte Interphase (SEI), correlates to an irreversible capacity loss for the battery. As cycling continues, the SEI can grow until it chokes off ion transport completely, causing total "brick" failure of the cell[15, 16], or irregularities in the thickness/makeup of the SEI can create local variations in the current density across the anode surface, which can result in dendrites[17, 18]. Ultimately, the inherent faults of the anode will reveal themselves sooner or later, and so are better addressed head on. Reexamining the lithium battery chemistries in Figure 1.1 in terms of what is possible instead of what is currently practical, one can see that there is significant potential in returning to the lithium anode if the inherent safety issue of dendrites could be circumvented. Solid lithium has an order of magnitude increase in theoretical specific capacity versus graphite[19, 20], which could be the key to the expanded range of electric vehicles (EV) needed to make them more competitive in a larger section of the market.

Another major hurdle to the penetration of EVs into the market is cost. Although increased scale and development of lithium battery manufacturing has led to an impressive reduction in cost over the last decade[21], there are limits to cost reduction that arise purely from economies of scale[22]. In order to meet the target of $150/kWh, considered to be the limit at which EVs are competitive with the internal combustion engine (ICE)[21], work must be done to change the makeup of the battery itself to more efficiently use cell components such as the current collectors and cell casing. Along these lines, commercial interest exists in increasing the thickness of electrodes[23, 24], and reducing electrode porosity[25]. A thicker coating of electrode will require fewer cell hardware components overall for the same energy content, but these efforts must be balanced against the rate-limiting factor of Li transport and side reactions that occur during cycling (SEI growth). Even if electrode design were perfected to overcome these issues, there still remains the base cost of the electrodes themselves - particularly the cathode, wherein the most promising materials contain the more expensive elements of nickel and cobalt. At this impasse, the significance of reintroducing the lithium anode emerges again, given the potential for development of future state of the art battery chemistries such as Li air and Li sulfur[26-28], which propose to use cheaper and more energy dense electrode materials.

Thus, in the interest of improving the safety, performance and cost of our future energy storage infrastructure, this project seeks to better understand the causes of failure in lithium battery chemistry. By focusing on the initiation of these failures (ie the growth of the SEI and dendrites) at interfaces, I seek a better understanding of the underlying

morphological features that trigger them. Armed with this knowledge and acknowledging the variability of an inherently chaotic growth mechanism, even at a given set of conditions, I propose a method for creating a baseline against which dendrite prevention methods can be tested to determine the most promising candidates for future study.

1.2 Objectives

1. Develop techniques using nano-resolution X-ray computed tomography (nano-CT) to study morphological features of failure in lithium batteries

    a. Investigate the growth of the SEI within internal pores of graphite anodes

    b. Probe the internal volume of lithium dendrites to determine how subsurface morphology influences their formation and growth.

2. Develop an accessible and repeatable test to determine the effectiveness of dendrite prevention methods

    a. Create a baseline tracking the probability of dendritic/irregular growth in a standard set of cell conditions

    b. Compare relative likelihood of irregular lithium deposition with and without the presence of a particular dendrite prevention method

1.3 Hypotheses

SEI

1. The higher Z components of the SEI will increase the local X-ray absorption signal of a cycled graphite anode (versus an as received anode) enough that SEI growth in the internal anode pore structure can be observed by comparison of the absorption and phase contrast nano-CT data. (see §3.1.2)

2. The SEI forms on and clogs the surface pores of the anode, leaving the internal pore structure unaffected. (see §2.2.1)

Lithium Dendrites

3. Despite the low Z of lithium, the phase contrast mode of the nano-CT will be able to observe significant sub-micron morphological features of lithium dendrite morphology. (see §3.1.2).

4. Both the surface and subsurface features of the lithium anode contribute to the growth of dendrites. (see §2.2.3)

5. A repeatable and significant increase in stable continuous deposition without irregular growth in a cell, compared to an established baseline, is indicative of improved long term cell performance. (see §2.3.1)

2. Background

2.1 Electrochemistry Fundamentals

2.1.1 Lithium Batteries

Batteries are devices that store and convert electrical energy and chemical energy. Two electrodes are selected such that there exists a spontaneous driving force (the electrochemical potential, the specifics of which will be discussed in later sections) for a redox reaction to occur between them. These electrodes are then electrically isolated so that the flow of electrons taking part in the reaction is diverted outside of the cell itself to power an external load. When this external load is disconnected, the reaction is largely prevented from taking place (although it's unlikely the battery will be completely free of some small amount of self-discharge), leaving the battery to store the potential electrical energy until it is required. In primary cells, this exchange can only occur once; the reaction is irreversible. Secondary cells are designed with a reversible reaction that can be recharged and these batteries can be used for up to hundreds or thousands of cycles.

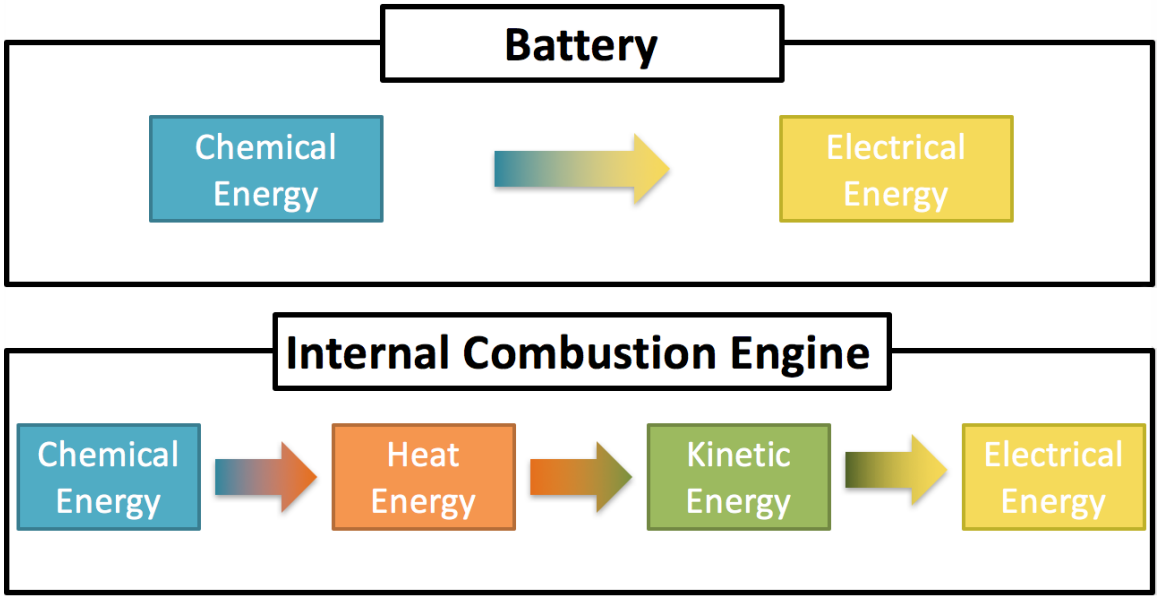

Figure 2.1. Energy production in a battery versus in an internal combustion engine system, adapted from O'Hayre[2].

The direct conversion of chemical to electrical energy is desirable in a power source as it is more efficient than other methods, such as the ICE. Figure 2.1 is a schematic look at the different energy conversions that occur in each system. When the ICE has to convert the heat generated by burning gasoline into useable work, significant amounts of energy are lost, and the overall efficiency of the ICE hovers at 20-25%[29]. Conversely, as the batteries do not involve a temperature change, they are not bound by the Carnot limitation[30]. Battery efficiency is tracked via the coulombic efficiency, which is a measurement of the difference between the energy used to charge the cell versus the amount of energy that can be effectively discharged into useable energy. Although there will always be some internal resistance in the battery that prevents it from achieving 100% coulombic efficiency, such as the ohmic loss during charge transport, modern lithium batteries have efficiencies around 90%[31].

Primary lithium metal batteries were first commercialized in the 1970s and their high energy density made lithium based chemistry a desirable candidate for secondary batteries. When John Goodenough discovered that $LiCoO_2$ could reversibly store and discharge lithium in 1982[32], this paved the way for early commercialization of lithium metal secondary batteries from Moli Energy. Unfortunately, these early cells were plagued with safety issues as dendrites inevitably caused shorting, resulting in cells catching fire and customer injury. Within a few years of this failure, the technology was reimagined with a nonreactive graphite as the anode, which acts as a framework to store the lithium. Thus, the cells came to be known as lithium ion batteries, instead of lithium metal batteries, as lithium is never meant to be in a metallic state at any point of the charging/discharging process.

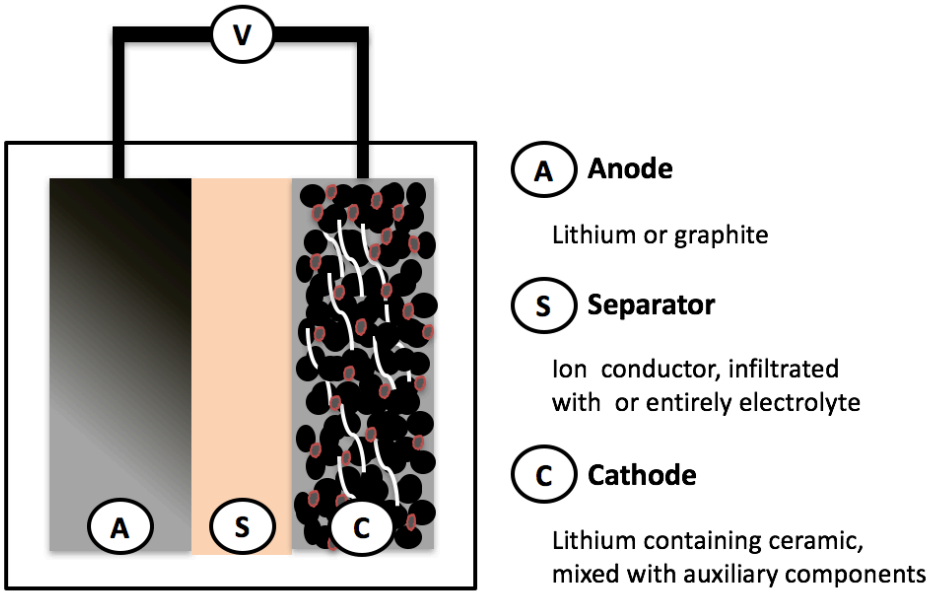

Figure 2.2. Schematic of a lithium (ion) battery.

Figure 2.2 shows the basic makeup of a lithium (ion) battery. The anode is most commonly graphite, as discussed previously, until safety concerns can be dealt with to allow the reintroduction of a metallic lithium anode. The separator acts as a physical barrier to prevent shorting between the electrodes. It must be ionically conducting, to allow the transport of lithium ions, but electrically insulating so that all current passes through the external load. In a cell with liquid electrolyte, which is also most common, the separator is a polymer material infiltrated with organic electrolyte (for example, ethylene carbonate containing lithium salt). In solid state batteries, the electrolyte material is one solid component that acts both as the transport medium and the physical barrier between electrodes (see §2.3.1). Finally, the cathode is a composite material made up of (i) a lithium containing ceramic ($LiCoO_2$, $LiMnO_2$, $LiFePO_4$, etc), (ii) high surface area conductive carbon and (iii) a polymer binder that keeps the former two components together. Most commonly, both electrodes are coated on a metal current collector, which gathers and transports the electrons through the external load.

2.1.2 Thermodynamics

The electrochemical potential between the two electrodes of the cell is a reflection of the difference in the relative affinity that each electrode has for electrons. An electron moving from a higher to a lower chemical potential will be in a lower energy state, thus reducing the overall energy of the system. From thermodynamics, it is known that this negative change in the energy of the system available to do work (the Gibbs free energy) results in a spontaneous reaction. A battery is only a useful power source if its reaction occurs spontaneously once the external load is applied. Gibbs free energy

cannot be measured directly, but must rather be derived from more physical parameters, such as the electric potential of the cell. The electric potential, then, can be used to determine if a cell reaction will occur spontaneously.

$$\Delta G^o = -nFE^o$$

Here ΔG^o is the standard change in Gibbs free energy, n is the moles of electrons transferred in the reaction, F is Faraday's constant (96,485 Coulombs per mole of electrons) and E^o is the standard potential of the cell. Potential must be reported for the cell as a whole because it is not possible to completely isolate the chemical potential of one electrode – rather it must be determined in reference to another electrode. The general standardization technique used by electrochemists to determine the potential of a single electrode reaction is to report it relative to the standard hydrogen electrode (SHE). The reduction potential of hydrogen in the SHE is taken to be zero, as shown below, with a few other reduction potentials relevant to lithium batteries. Species with a lower E^o than zero are harder to reduce (easier to oxidize) than hydrogen and vice versa. Lithium has one of the highest propensities to oxidize, being an alkali metal, which is part of the reason why it is such a promising battery material.

Reduction	E^o (V)[33]
$Cu^{2+} + 2e^- \rightarrow Cu$	0.3419
$2H^+ + 2e^- \rightarrow H_2$	0.000
$Al^{3+} + 3e^- \rightarrow Al$	-1.662
$Li^+ + e^- \rightarrow Li$	-3.040

These standard potentials are only relevant at standard temperature, pressure, and activity of the cell components. The Nernst equation can be used to adjust this standard potential to different cell conditions.

$$E = E^{\circ} - \frac{RT}{nF} \ln (Q)$$

Where R is the ideal gas constant, T is the temperature in Kelvin and Q is the reaction quotient, an adjusted ratio of products and reactants that can indicate whether the reaction is more or less likely to occur than in standard conditions. The resulting potential (E) describes equilibrium under these conditions. Battery reactions do not occur at equilibrium and so this value must be adjusted further to take kinetics into account, as discussed in the next section.

Although the SHE is the most important reference standard in electrochemistry, the SHE itself is very difficult to set up and so in practice it is more common to use other reference electrodes (Ag/AgCl, Hg/Hg_2SO_4, etc), with known potentials. Within a particular field of electrochemistry (ie lithium batteries), potentials can also be reported with respect to another relevant reduction potential, such as Li^+/Li.

Finally, thermodynamics is what allows us to calculate the theoretical specific capacity of lithium.

$$\frac{1\,(e^-) * \ 96{,}485\frac{C}{mol\ e^-}}{6.941\frac{g}{mol\ Li} * 3.6\ \frac{C}{mAh}} = 3{,}861\frac{mAh}{g}$$

This value is only concerned with the peak theoretical capacity of the lithium anode itself, and does not take into account the additional mass of necessary and inert battery components such as the current collectors, casing, separator, etc. Even ignoring this mass, it is not practically possible to reach the above theoretical capacity, as it would require the anode to completely oxidize. Rather, this value is used as a baseline against which other prospective anodes are compared.

2.1.3 Kinetics

As mentioned above, batteries do not function practically in an equilibrium state, and so the observed potential will vary from that predicted by the Nernst equation. This variation is referred to as the overpotential (η) and it can be broken down into three different types, representing different resistance losses that exist in the cell: activation overpotential (η_{act}), ohmic overpotential (η_{ohm}), and concentration overpotential (η_{conc}). The activation overpotential arises from needing to overcome the activation energy barrier of the reaction, and can vary as the surface morphology varies. Deposition could occur more easily at a defect site, for instance, and have a lower activation energy

barrier. The ohmic overpotential reflects the ohmic losses that occur due to physical resistances in the cell, as the electrons move through the cell components and connections, and the ions move through the electrolyte. This can evolve with cycling as contact between components shift and reactions cause local temperature change, but is considered to be relatively constant when compared to the other two losses. The concentration overpotential arises from what is otherwise known as the mass transport loss. Most simply, there is a limit to how fast the reactant can be transported to the electrode surface in order for the reaction to take place. Once this limiting current is reached, the reactant is immediately consumed as soon as it reaches the electrode surface – the reaction cannot sustain this pace and the voltage drops precipitously. To find the potential of the cell (V), one must take into account all three.

$$V = E - \eta_{act}(i) - \eta_{ohm}(i) - \eta_{conc}(i)$$

Furthermore, each overpotential is a function of current and will be more or less relevant depending on the conditions the cell is being run at. A qualitative comparison of the effects that these three overpotentials have on the cell potential can be seen in Figure 2.3. Activation losses dominate at lower currents, whereas transport losses dominate as the limiting current is approached. This balance of the various losses can also be affected by cell conditions such as the concentration of the electrolyte, the temperature, etc.

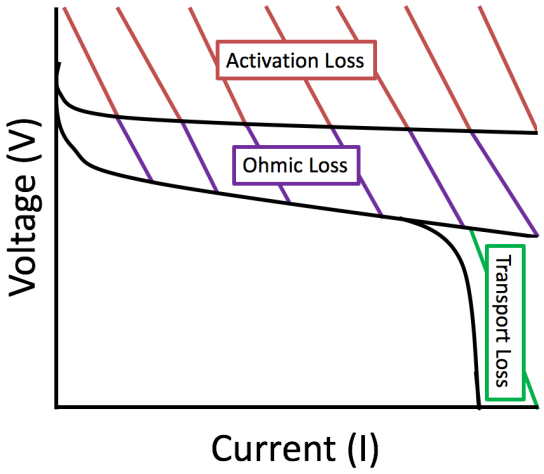

Figure 2.3. Relative qualitative effects of activation, ohmic and transport losses as a function of current.

2.1.4 Activation Overpotential and the Butler Volmer Equation

Under conditions where activation overpotential dominates (ie where charge transfer is the limiting step in the reaction), the Butler Volmer equation shows the approximate relationship between current and overpotential on a particular electrode.

$$i = i_o \left\{ \exp\left(\frac{\alpha_a z F \eta_{act}}{RT}\right) - \exp\left(\frac{\alpha_c z F \eta_{act}}{RT}\right) \right\}$$

Here, α_a and α_c are the anodic and cathodic charge transfer coefficients, respectively (representing the overall symmetry of the reaction backwards and forwards – often assumed to be 0.5, or fully symmetric), z is the number of electrons involved in the reaction, F is Faraday's constant, R is the ideal gas constant, T is the temperature, and η is the activation overpotential, or the deviation from the thermodynamically calculated equilibrium potential that is required to cause the reaction to happen. This is

significantly tied to i_o, the exchange current density, which is a measure of how freely the reaction can proceed backwards and forwards on the surface of the electrode. Essentially, when no current flows through the system, there is still some equilibrium exchange of electrons back and forth – this is the exchange current. A high exchange current density indicates that the barrier to charge transfer is low, therefore the activation overpotential will also be low, and vice versa.

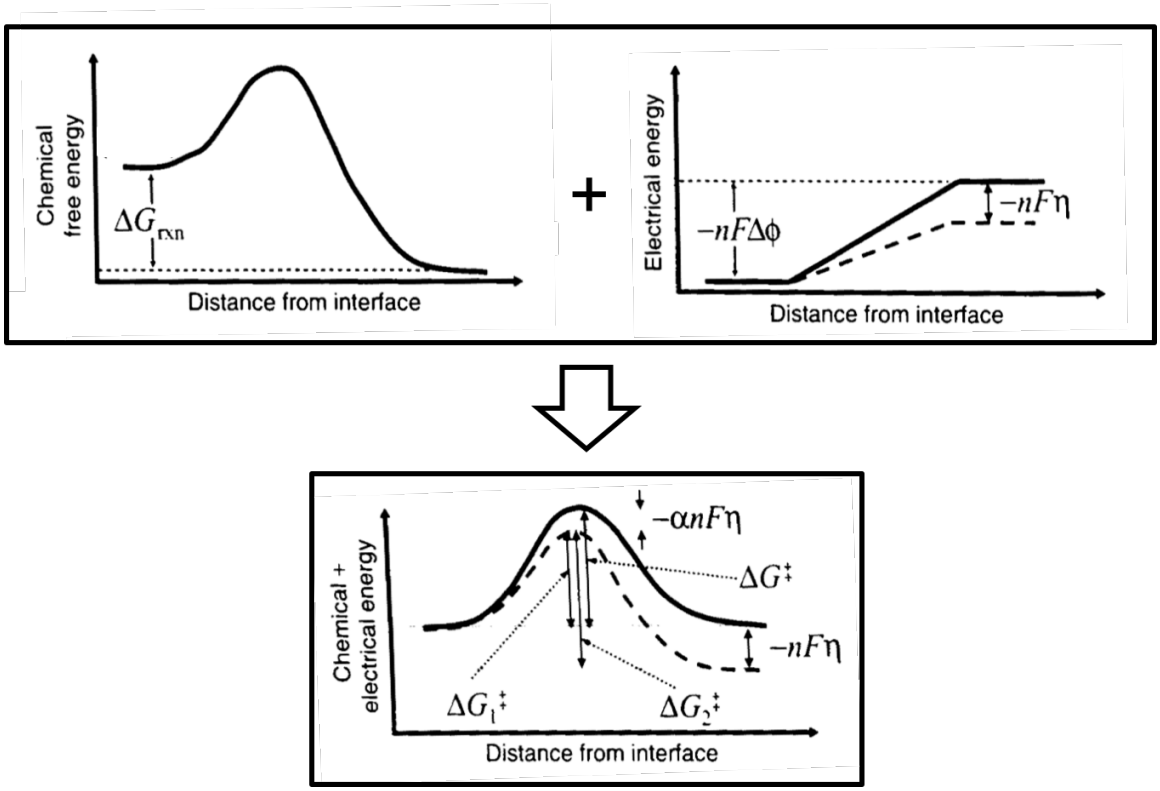

Figure 2.4. The combined effect of chemical and electrical energy on the activation energy barrier, adapted from O'Hayre[2].

Figure 2.4 shows how an applied potential can affect the likelihood that a reaction will occur. When one considers only chemical potential of neutral species, the difference in the Gibbs free energy between the reactants and products is only significant if the

system has enough energy to surpass the activation energy in the first place. In the case of charged species, however, the potential of the system is a crucial factor in determining the relative free energy of the reactant and product. By applying an overpotential in a particular direction, the activation energy barrier can be manipulated so that it is lower in the forward direction and higher in the backwards direction, as shown. This overpotential is a loss as far as our overall power is concerned, since it lowers the voltage available for useful work, but it is necessary to drive the reaction forward.

A more drastic deviation from ideal performance arises from the fact that potentials are not applied equally across the surface. Surface roughness leads to a variation in sites available for deposition, which will have different exchange current densities associated with them and thus different required activation energy barriers that must be overcome for deposition to occur. If deposition is favored in a few highly concentrated areas rather than spread more evenly across the entire surface, dendrites or other irregular growth can occur, resulting in cell failure. Dendrites will be discussed more fully in future sections. First, conditions relevant to the other two types of overpotentials (concentration and ohmic), will be discussed.

2.1.5 Deposition Conditions at a Surface: the Debye Length

In order to discuss the concentration overpotential, one must first discuss the interface of the electrolyte and the electrode. A significant factor in electrodeposition is the distribution of ions at the surface of the electrode and the resulting shielding effect they

have between the electrode and the rest of the electrolyte. This shielding effect is characterized by the Debye Length (K_D^{-1}), which is a measurement of how far the potential at the electrode surface penetrates into the solution. The Gouy-Chapman theory of the diffuse double layer approximates this distance.

$$K_D^{-1} = \left[\frac{1000 N_A q^2}{K_B T \epsilon} \sum_{i=1}^{n} c_i z_i^2\right]^{-\frac{1}{2}}$$

From this, one sees that higher concentrations and higher valencies of solvated ions will result in a shorter K_D^{-1}. This solution requires a linearization of the Poisson-Boltzman equation which is only valid for cases in which the potential at the surface is a significantly smaller than the thermal energy of the solution. When an electrode is at a higher potential relative to the thermal energy, this approximation does not provide a strictly accurate estimation of the Debye Length. This approximation also assumes a single, symmetric electrolyte (ions of the same valence), and so it must be corrected for mixed asymmetric electrolytes to take ion interaction into account. Further, Gouy-Chapman treated ions in solution as point charges, and so did not consider how ion-ion interactions would create resistance in an approach to the electrode surface. The development of a model to correct for these deviations in the experimental system used in this work is nontrivial.[34]

A prevailing model used to provide a simplified physical understanding of this fairly complex system is the Stern correction to the Gouy-Chapman model. Stern theorized

the existence of a rigid layer of ions with finite size in close proximity to the electrode surface – typically understood to largely consist of solvent molecules that have oriented themselves in the direction of the electric field coming from the electrode. The potential drops linearly across this Stern layer and then decays exponentially outward into solution, as seen in Figure 2.5. This corresponds to a concentration gradient in the solvent, with solvated counter ions existing in significantly higher concentrations close to the electrode/electrolyte interface and then dropping off to the bulk concentration at distances closer to K_D^{-1}.

In order to undergo charge transfer during electrodeposition, the solvated ions must reach the electrode surface despite the presence of solvent molecules strongly interacting with the surface. The extra driving force required to allow the ions through is part of what makes up the overpotential associated with the reaction.

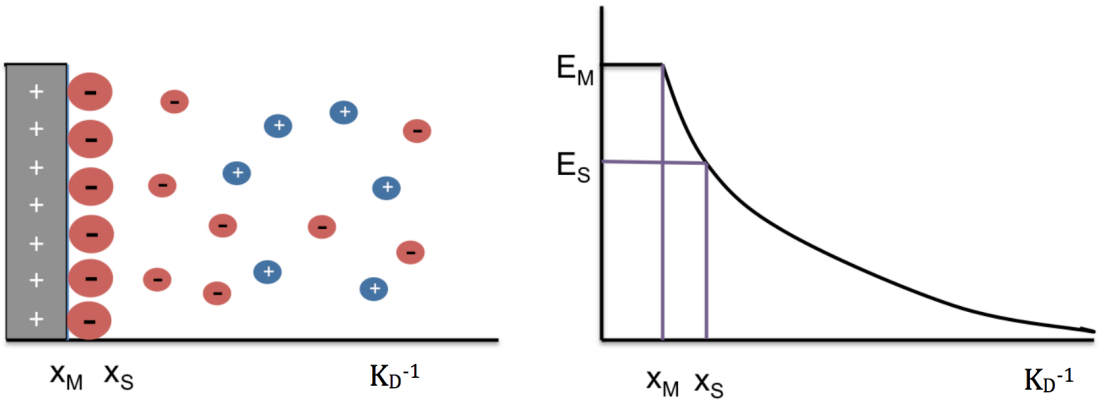

Figure 2.5. Depiction of ion distribution at an electrode surface (left) and the resulting exponentially decay in potential from that surface (right). M denotes the metal surface and S denotes the Stern layer.

2.1.6 Concentration Overpotential

The Butler Volmer model of electrokinetics can only be applied to a specific set of circumstances where activation control is in effect, because it does not take into account the concentration effects at high rates. These arise because the reaction can only be successfully driven at rates up to a particular rate, known as the limiting current, i_L. At currents approaching the limiting current, the system is under mixed control conditions, as the concentration of the reactant is severely diminished at the electrode surface up to the limiting current condition, where it is completely depleted. At this point the exponential behavior predicted by the Butler-Volmer model levels off and the voltage drops precipitously.

$$i_L = \frac{2eDC_0}{t_a L}$$

The limiting current was found by Brissot et al[35] to be determined by the elementary charge (e), the diffusion constant (D), the initial concentration of the electrolyte (C_0), the anionic transfer number (t_a), and the distance between the electrodes (L). The anion transference number represents the relative amount of charge carried by anions compared to the total amount of charge carried by anions and cations, represented by the ion mobilities μ_a and μ_c, respectively.

$$t_a = \frac{\mu_a}{\mu_c + \mu_a}$$

The diffusion constant becomes more complex when the electrolyte must move through a porous material, where one must consider the porosity and tortuosity of the reacting surface. Lithium battery electrolytes have to contend with not only intercalating electrode materials, but also a complex resistive layer on the surface of the electrodes: the Solid Electrolyte Interphase (SEI), which will be discussed in §2.2.1. Another important factor to consider is the effect of temperature on the diffusion coefficient. Lower temperatures slow down diffusion, which lowers the limiting current threshold and exacerbates the effects of an uneven distribution of current along the surface, as will be shown in the dendrites section. The diffusion layer exists beyond the diffuse layer of the double layer, discussed above, where there is no gradient in potential but a possible gradient of concentration. Its length is affected by the transport conditions of the system, such as the effective diffusivity, the bulk concentration, and other factors that affect the double layer, as discussed above. The shorter the diffusion layer, which would correspond to facile transport conditions, the larger the threshold that exists to hit the limiting current.

2.1.7 Effects of Combined Losses: Series Resistance

When performing tests on an electrochemical system, it can be difficult to distinguish the individual contributions of each type of overpotential to the overall loss in voltage. Rather, one must consider the gross change in cycling performance and determine the likelihood of one particular loss mechanism dominating, or the mixed presence of multiple overpotentials. One way to check how the resistive elements of the cell change

with cycling is to calculate the series resistance of the cell. This is found by tracking the voltage drop (or jump) that occurs when the current direction is switched between plating and stripping, denoted as states 1 and 2 in the equation below. This equation allows one to track how relative resistance changes in the cell and how they evolve with cycling.

$$R_{series} = \left|\frac{V_2 - V_1}{i_2 - i_1}\right|$$

2.2 Lithium Battery Failure

This work is primarily concerned with two types of battery failure: the continuous formation of a Solid Electrolyte Interphase (SEI) layer on the electrodes, and the growth of dendrites. The former is an impediment to the durability of cells with long cycle lives, and the latter is a serious safety hazard that stands in the way of implementation of lithium ion batteries in a wider range of conditions and developments in battery chemistries beyond lithium ion.

2.2.1 Solid Electrolyte Interphase (SEI)

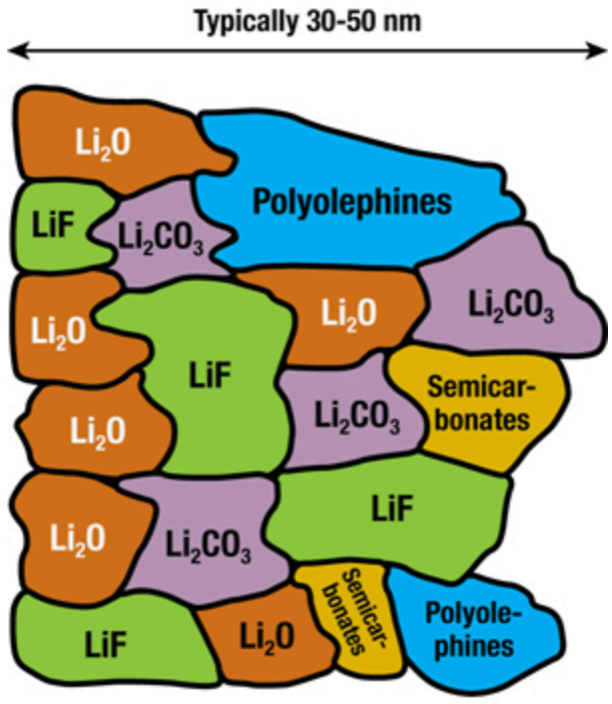

Figure 2.6. A schematic representation of the SEI's mosaic makeup, from Peled et al.[3], adapted by Argonne National Labs.[4]

Standard non-aqueous electrolyte Li-ion batteries operate across a voltage range that, at times, surpasses the thermodynamic stability limit of the organic solvents used in the electrolyte. This results in various species decomposing and coating the surface of the electrodes, a process commonly called SEI formation. The composition of the SEI depends on the cell conditions, such as the electrolyte makeup and the electrochemical parameters used in the first formation cycle of the battery. An example is shown in Figure 2.6. In general, the SEI must be an ionic conductor, to allow lithium ion transport, and an electronic resistor, to prevent further side reactions that cause SEI build up. A stable SEI film is important to the long term cyclability of the battery, as an SEI that

grows too thick can cause high internal resistance in the battery and an SEI that doesn't have good mechanical strength and flexibility can break – leaving the anode surface bare to further side reactions/SEI build up and potentially leading to dendrite formation, as will be discussed in §2.2.3. A proposed method of dendrite prevention, discussed in §2.3.1, is the introduction of an artificial SEI with more stable long-term properties than the native SEI that forms when the electrode contacts the electrolyte.

The bulk of SEI growth has been found to occur mainly on the surface of the anode, and historically has been attributed to electrolyte breakdown occurring only on the anode side of the cell,[14, 36] but as higher voltage cathode materials have been developed, there is increasing evidence that oxidized products of the electrolyte can increase the resistance of the cathode,[37, 38] and, more significantly, migrate to the anode where they undergo a reduction/precipitation reaction.[39, 40] This movement of oxidized species created at higher voltage cathodes under high states of charge is thought to explain the formation of passivation layers on anodes that operate at less extreme potentials, such as the lithium titanium oxide anode electrode that exhibits no SEI formation when paired with the lower potential $LiFePO_4$ cathode material, yet shows significant build up when paired with higher operating potential cathodes.[41, 42] As such, battery products that use higher capacity and higher voltage cathode systems combined with thick and dense anode structures, such as the graphite anodes used for consumer electronics and/or long range electric vehicles, will likely be more prone to catastrophic SEI build up. The excessive build up fills pores to the extent that lithium ion transport through the

electrode becomes highly resistive, generating large overpotential and reducing capacity at a given C-rate[40].

The accumulation of the reduced precipitate species that compose the SEI correlates to an irreversible capacity loss for the battery for two reasons: (1) lithium ions are consumed during SEI formation and (2) electrode pores are blocked, creating a less porous and more resistive path for lithium ion transport.[15, 16] Although conclusive work has been done proving that uninhibited growth of the SEI will lead to cell failure,[43, 44] more work needs to be done to characterize the nature of SEI growth throughout the electrode. The simulation work of Pinson and Bazant[45] suggested that the thickness of the electrode is a significant factor: thinner electrodes would grow SEI uniformly in their pores, whereas thicker (and also more dense, less porous) electrodes would tend to build up SEI on the surface. Chattopadhyay et al.[46] suggested that the rate of SEI formation is anisotropic and depends on the underlying surface orientation. This work was particularly interested in the proposed schematic mechanism of Burns et al.[40], wherein oxidized species from the cathode migrated to and were reduced at the anode, primarily blocking the pores at the surface. Hypothesis 2 seeks to determine the extent to which this proposed mechanism is borne out in the observed morphology of a cycled electrode.

Hypothesis 2: The SEI forms on and clogs the surface pores of the anode, leaving the internal pore structure unaffected.

2.2.2 Dendrites: Theoretical Introduction

Dendrites are irregular depositions on an electrode/electrolyte interface that arise from mass transport limiting effects. When the concentration of the reducing ion (Li^+, Cu^{2+}, etc) drops to zero at the surface of the electrode that is being deposited on, there is significant resistance against thermodynamically favorable homogeneous plating and kinetics considerations dominate, resulting in non-uniform highly anisotropic deposition morphologies. Irregularities on the electrode surface alter the local diffusion gradient of the reducing ion from the simplified linear model to a spherical one (Figure 2.7). This diffusion concentrates deposition at the tip of the protrusion and causes it to grow out from the electrode surface at angles determined by the metal's closest packed directions[47]. As the tip of the dendrite moves from the surface through the diffusion boundary layer, it encounters higher concentrations of metal salt, which promote its growth even further[13]. Ultimately, the surface of the dendrite itself can induce a nucleation site for dendritic growth, causing the single (primary) dendrite filament to branch – hence the name, from the tree like appearance in some traditional metal systems (lead, copper).

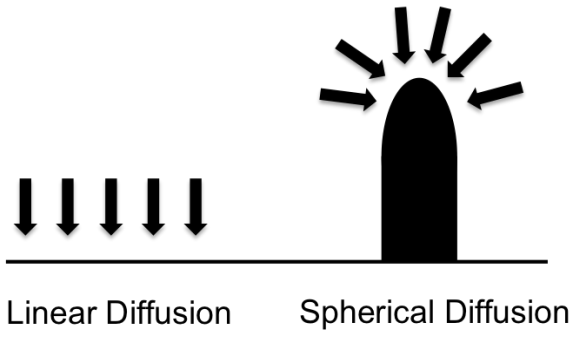

Figure 2.7. Comparison of linear and spherical diffusion gradients, adapted from Akolkar[5].

The time it takes for the local ion concentration to drop to the point that dendritic growth initiates is called the Sand's time, from Henry J. Sand's work with copper deposition[48]. An equation for Sand's time (τ_s) was reported by Rosso et al[49] as a function of the ambipolar diffusion constant (D), initial electrolyte concentration (C_0), the elementary charge (e), the cation charge # (z_c), the current density (i), and the anion (μ_a) and cation (μ_c) mobilities.

$$\tau_s = \pi D \left(\frac{C_0 e z_c}{2i}\right)^2 \left(\frac{\mu_a + \mu_c}{\mu_a}\right)^2$$

Clearly, one can conclude that dendrites are favored in conditions that would slow mass transport kinetics at the surface of the electrode, such as low electrolyte concentration, conductivity, and temperature, in addition to high currents and overpotentials[50-52]. Additionally, one sees that cation vs anion mobility is significant: specifically, a lower anion mobility leads to a longer Sand's time.

2.2.3 Dendrites in Lithium Batteries

When lithium primary (or single use) cells were introduced onto the market in the 1970s, their impact was immediately felt due to their impressive energy density compared to other energy storage technologies. Within the next couple decades, significant work was undertaken to investigate a secondary (or rechargeable) lithium battery that would allow for more efficient use of the cells. However, attempts to commercialize batteries with lithium metal anodes had to be discontinued after multiple field failures occurred as

a result of the formation of dendrites, which internally short-circuited the batteries and resulted in catastrophic failure[12, 53]. This led to the production of alternative anode materials to replace solid lithium, mostly notably graphite in the majority of commercial cells used today. Graphite acts as an inactive storage framework for the lithium ions, which are stored as the less reactive Li_xC_6 instead of being deposited as solid lithium. This results in a lower overall energy density of the cell in exchange for dendrite growth being significantly less likely under most conditions. Unfortunately, dendrites and, consequently, internal short circuits can still occur at higher charging rates and lower temperatures, which limits the incorporation of lithium ion batteries into technologies that demand faster charging and more versatile performance. In this work, the author develops new methods to better understand dendrite nucleation and growth in order to ultimately design strategies of prevention. This is important both to (1) improve the performance and safety of our current energy storage infrastructure but also (2) to pave the way for the development of future state of the art battery chemistries such as lithium air and lithium sulfur[26-28], which reintroduce the lithium metal anode and regain its energy capacity.

Decades of studies have proven that irregular or dendritic growth in lithium batteries is ultimately more complicated that the traditional aqueous metal dendrite systems. There are more factors to consider, most notably the SEI, that can lead to a variety of different growth mechanisms and morphologies. Terms like “needle-like”, “whisker”, and “mossy” are used to distinguish between morphologies, but there is no established consensus on how to delineate these categories[54, 55]. Most often, any irregular growth

is referred to as dendritic and any cell short during cycling is assumed to have been caused by dendrites. The battery community is currently in the liminal stages of recognizing it has to be more specific in the discourse of this phenomena. Until consensus is reached, this thesis will largely refer to such growth as dendritic when discussing the work of others who have used such terminology or cases where dendrites can clearly be seen, and irregular when discussing the general issues of unfavorable deposition.

Previously, several innovative methods have been developed to investigate in-operando dendrite propagation. Howlett et al.[56] created a sealed transparent cell and used optical microscopy to record the growth of mossy “dead” lithium on the surface of lithium metal electrodes. Crowther et al.[53] designed a microfluidic cell which also used optical microscopy to track the growth of lithium dendrites in liquid electrolytes. Optical microscopy naturally suffers from lower resolution (on the micron scale) and so dendrites cannot be observed in these conditions until they have grown to a fairly significant size. Dollé et al[57] used live scanning SEM to observe the lithium surface interface with the polymer electrolyte as dendrites grew and delaminated the electrode from the electrolyte. However, the electron beam itself caused the polymer to degrade, which limited the time scale and conditions that this phenomenon could be tracked.

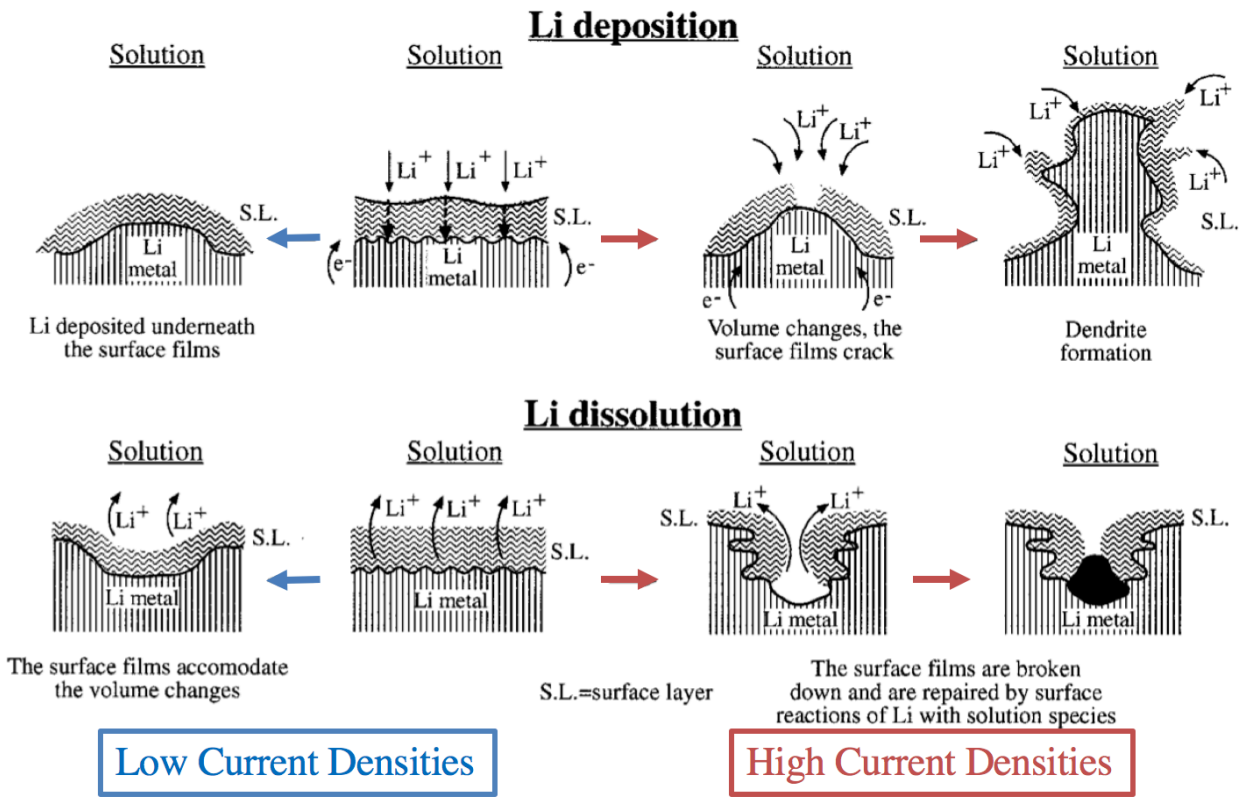

Figure 2.8. A schematic of how SEI cracking can cause dendrite growth, modified from the work of Cohen et al.[6]

In the absence of a technique that allows for the high-resolution view of dendrite growth, several mechanisms have been suggested for dendrite nucleation. Early work by Yamaki et al.[58] indicated that the non-uniform deposition and dissolution of lithium onto the anode during cycling resulted in increased strain on the SEI. This pressure would ultimately lead to cracks in the SEI layer, exposing bare lithium to the electrolyte for preferential deposition with dendritic behavior. Figure 2.8 shows that SEI cracking as a major onset cause of dendrites has been supported in further AFM studies by Cohen et al.[6] (as well as SEM studies by Stark et al.[59]). However, these techniques are limited to

surface observations and so cannot observe the initial lithium build up under the SEI until the metal is extruded from these cracks.

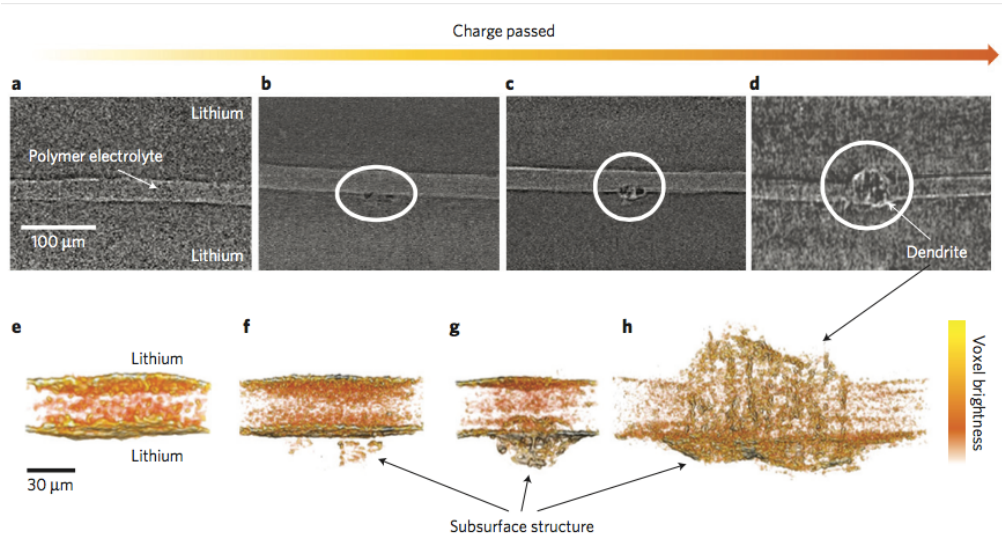

Figure 2.9. Micro-CT radiographs and 3D reconstructions showing subsurface growth in lithium films during electrochemical charging, taken from work by Harry et al.[7]

Further studies report other methods for imaging the morphology of Li electrodes with the intent of tracking dendrites formed during charging. Some of these methods include: scanning transmission electron microscopy (STEM) for 2D images with resolution in the nanometer regime[60, 61], scanning electron microscopy-focused ion beam (SEM-FIB) where the sample cross-sections are obtained through destructive ion milling[62, 63], ^{7}Li magnetic resonance imaging (MRI) and nuclear magnetic resonance (NMR) where the Li chemical shifts are correlated and used to determine the local microstructures[64, 65], and micro-scale resolution x-ray computed tomography (micro-CT)[7, 66-69]. Micro-CT

allows for the 3D morphologies of internal structures to be non-destructively reconstructed with a resolution of 1 μm and can be performed on samples sealed in gas or liquid environments. It was with this last technique that Harry et al.[7] discovered that understanding dendrite nucleation is not just an issue of being able to observe the surface of the lithium under the passivating SEI layer. In fact, significant activity under the surface of the lithium itself needs to be tracked in order to fully understand lithium dendrite nucleation (Figure 2.9). Unfortunately, the resolution of the micro-CT was not sufficient to adequately resolve these subsurface growths in order to fully understand them, leaving the path open for further study. This is the basis of Hypothesis 4.

Hypothesis 4. Both the surface and subsurface features of the lithium anode contribute to the growth of dendrites

2.2.4 Dendritic Failure

By expanding the category of what is considered dendritic growth, one must reconsider certain conclusions that were made about dendrites in traditional aqueous systems. For instance: is a lithium battery more likely to experience dendritic failure at higher or lower temperatures? Akolkar's modeling work[13] on lithium dendrites predicted that there is a critical lower bound of temperature, under which uncontrolled dendrite growth will occur. Lithium deposition studies have shown more dendritic growth at lower temperatures. Ota et al.[70] found that lithium deposited at 0 °C was more dendritic than at 25 or 50 °C. Love et al.[50] saw significantly more irregular growth at -10 °C compared to 5 or 20 °C. However, it was the deposition at 5 °C that shorted the cell fastest. Additionally, Park et

al.[71] showed that it took the longest for deposition at -5 °C to short a symmetrical lithium coin cell, when compared to deposition at 15 and 35 °C with the same current density. It appears that it is not only relevant that dendritic growth occurs, but what type of dendritic growth is occurring.

One way of categorizing dendrites is by acknowledging the different mechanisms and morphologies that arise from where the growth is being driven from. Tip growth most closely resembles the behavior of traditional metal dendrite deposition, driven by mass transport phenomena. Akolkar predicted that even at 40% of the limiting current density, the local current density experienced by the tip of the dendrite is 60% greater than that of the surface[13]. Bai et al.[72] showed that tip growth was required to short a ceramic separator in their cell. Cheng et al.[48] also discuss how dendrites driven by tip growth are the primary cause of shorting in batteries.

Tip growth cannot explain all dendritic behavior, as lithium dendrite growth is more complicated than traditional diffusion and mass transport models. Crowther et al[53] observed that lithium dendrites still grew in their microfluidic flow cells – conditions where concentration depletion is no longer an issue – and in fact, the growth was observed to initiate faster in conditions where the limiting current density was increased. Similarly, Steiger at al.[73] observed side growth initiating from kinks in the dendrite while the tip remained unchanged, although the current density was low enough that no concentration gradient was expected. Here we must return to the concept of lithium deposition below the SEI causing it to crack outward, extruding the lithium from the

crack. Since the proposed mechanism shown in Figure 2.8[6], further studies have shown that SEI cracking can occur at lower current densities as well, depending on the cell conditions[48, 55]. This can account for both root growth and the above described side growth, if the SEI is thin enough at a particular kinked section of the dendrite[73]. Although this mechanism for dendrite growth is not considered to be responsible for cell shorting, shorting is not the only way a battery can fail. Exposing more bare lithium to the electrolyte incurs more SEI growth and thus a depletion of the cell's capacity. Furthermore, this new SEI growth will be thinner than the SEI that has built up on the previously exposed lithium. When lithium is stripped during cycling, it will preferentially be removed from the area of thinnest SEI[74, 75]. In the case of root growth, this can lead in significant sections of lithium dendrite that are electronically insulated from the cycling process, as shown in Figure 2.10. This isolated lithium is often referred to as "dead lithium" and is a significant drain on the cell's capacity that can ultimately lead to failure.

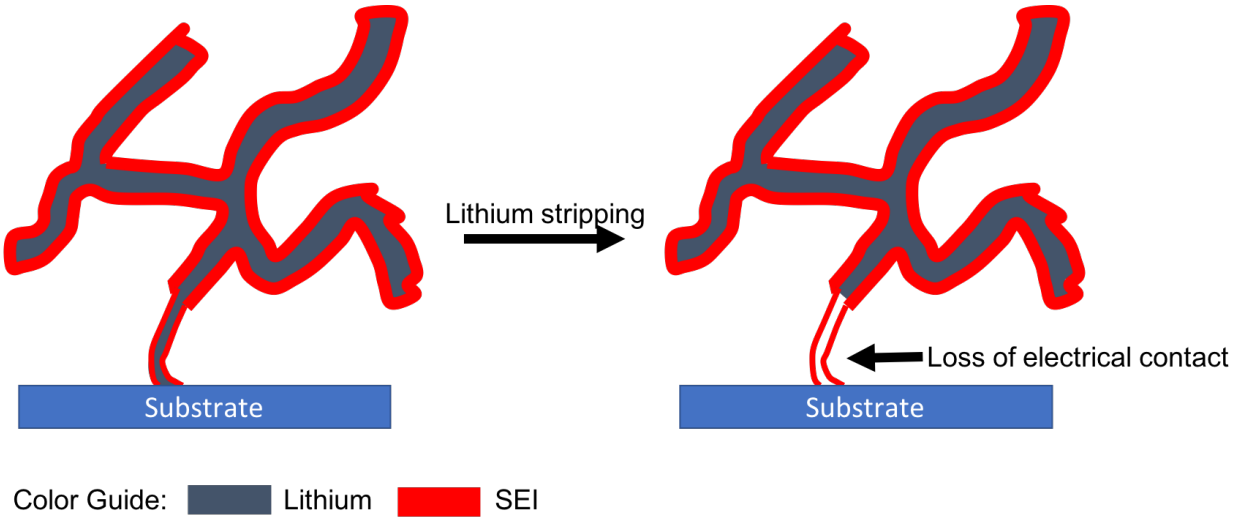

Figure 2.10 Selective dissolution of lithium near the substrate during lithium stripping results in electronic isolation of the rest of the dendrite network, resulting in "dead lithium"

In the testing conditions of a full cell, mixed variables can cause different types of dendrite growth to occur concurrently. The relative presence of different growth types and their likelihood to cause cell failure depends on a wide variety of cell conditions including current density, temperature, pressure, electrolyte concentration, solvent, and salt. The only constant is that any irregular dendritic growth can ultimately lead to failure, and therefore, one must try to prevent all modes of dendritic growth from occurring. Before an effective prevention strategy can be implemented, however, one must conclusively determine the likelihood of irregular or dendritic growth to occur in a particular set of conditions – standardizing all cell parameters listed above as much as possible. Then one can compare the performance of a particular dendrite prevention method to an established baseline. One concern is that the array of variables that affect

dendrite growth is so complex that not all of them are able to be accounted for in replicate experiments.

2.3. Dendrite Prevention Methods

The long-term interest in preventing dendrites has resulted in a wide assortment of proposed prevention methods. Some involve changing the cell components themselves. For instance, the current collector in the cell is typically a flat sheet of copper. By increasing the surface area of the copper, either as copper microchannels[76], or copper nanowires[77], the local current densities on the surface of the anode will decrease and thus the likelihood for dendrites to form due to mass transport restrictions. A further high surface area electrode framework was introduced in the work of Zhamu et al.[78], who plated lithium onto graphene sheets. Another avenue of dendrite prevention is changing the cell cycling conditions. Increased pressure has been widely shown to increase cyclability[48, 55, 70, 79], ostensibly by suppressing dendritic growth. This is relevant to consider when one acknowledges that many studies observing dendrites are done outside of a typical coin cell or battery enclosure and so do not take typical pressure conditions into account. Mayers et al.[80] used coarse grained simulation to arrive at their suggestion to charge the lithium electrode in pulses, as opposed to constant charging. These interruptions in charging would be intended to allow the system to recover from any accumulating mass transport overpotential as the lithium ion concentration at the electrode dropped.

Electrolyte conditions play a major role in cell performance and the likelihood of dendrite growth. A straightforward way to attempt dendrite prevention is to increase the concentration of the lithium salt, thus making ion depletion less likely. Jeong et al.[81] found improved coulombic efficiency at higher salt concentrations, and also used TEM to determine a noticeable difference in the SEI thickness depending on electrolyte conditions (the higher concentration had a thinner SEI). Qian et al.[82] investigated some of the highest salt concentrations in the literature (4 M compared to the typical 1 M in commercial electrolytes) and reported a continuing trend of improved performance at higher concentrations. A cautionary result was exhibited in the work of Park et al.[83], which showed that the increased viscosity from higher salt concentrations led to a decrease in the time it took for their cells to short. Rather than adjust the lithium salt concentration, Ding et al.[18] added small concentrations of Cs and Rb salts (0.0001-0.1M). The model was that the cations would be drawn toward developing protrusions on the lithium surface and there form an electrostatic shield, making it more favorable for lithium to reduce elsewhere on the electrode surface. Experimental results showed an improvement of deposited film homogeneity with the added alkali salts, but a reduction in coulombic efficiency. Solid state electrolytes are also of interest and will be discussed in §2.3.1.

From the Sand's time equation, one can see that a lower anion mobility will increase the stable deposition time before dendrites occur. A lower mobility means the anions remain near the electrode during charging, increasing the pull of cations to the surface[55] and alleviating some concentration overpotential issues. Additionally, Tikekar et al.[84]

found in their model that by immobilizing anions at the electrode surface, a lower bound to local conductivity was established and this led to more stable growth during deposition. Lu et al.[85] used ionic liquid tethered inorganic nanostructures on the electrode surface not only to immobilize anions, but also to create a porous network that dendrites would have difficulty growing through. They reported a significant increase in the time to dendrite growth onset when compared to a bare electrode. Another way of conceptualizing a system with low anion mobility is to maximize the lithium mobility towards the goal of a single ion conducting electrolyte. Schaefer et al.[86] added inorganic nanoparticles with tethered organic components to battery electrolytes, which resulted in a lithium transference number of 0.7-0.96.

The SEI plays a crucial role in the stability of lithium deposition, since it has a significant role in determining the current distribution on the electrode's surface. Basile et al.[87] showed that replacing the typical formation cycle of the SEI with a twelve-day soak of the lithium electrodes in ionic liquid led to stable cycling for 1000s of cycles. Such a long formation procedure isn't commercially desirable, and so more groups have focused on electrolyte additives that can influence the SEI to form in more desirable configurations. Zhang et al[88] used small concentrations of Cs salt to induce lithium deposition as compact nanorods rather than dendrites. This improved stability was credited to the fact that the Cs salt addition enriched the LiF content in the SEI. Taking a more direct approach, Lu et al.[89] added halogenated salts to increase the halogen content in the SEI. Adding LiF improved capacity retention over 100+ cycles. Guo et al.[90] investigated VC-$LiNO_3$ as an additive and found that the coulombic efficiency increased and the

resistance of the SEI was stable as cycling continued – compared to a bare lithium electrode where the resistance of the SEI increased with cycling. By forming a more stable SEI, these methods are avoiding hot spots of particularly high current density on the electrode surface that lead to dendrite growth, but trace water in the organic solvents could still cause undesirable side reactions[91].

A more direct approach to improving the SEI's properties is to apply an artificial SEI to the surface of the lithium electrode. This can take many forms. Alumina coatings have been broadly investigated[92-94] for their potential to prevent hot spots of irregular lithium deposition early on. Other groups have studied the dendrite prevention potential of silanes[95], chlorosilanes[17], tetraethoxysilane[96], Li_3N[97], graphite[98], hollow carbon nanospheres[99], or LiF applied directly to the surface via magnetron sputtering[100]. What this work is particularly interested in is the application of solid electrolyte as an artificial SEI. Solid electrolyte as a dendrite prevention strategy have the potential to (1) create a more stable interface between electrolyte and electrode, (2) work as a single ion conductor and (3) act as a physical barrier to stymie dendrite growth.

2.3.1 Solid Electrolyte

The lithium battery community has been motivated for some time to find an alternative electrolyte to the standard liquid organic solvents due to their innate flammability, particularly when paired with the potential for dendrite growth in the battery. Solid electrolytes are a proposed alternative, having been in development since the initial work on secondary lithium ion cells and are used in current technological applications

that don't require high rate capability. They offer benefits in the form of increased safety, as they are both less reactive and their mechanical properties allow them to potentially act as a physical barrier to stymie dendrite growth across the membrane, in addition to increased durability and geometrical flexibility[101]. There are many different classes of solid electrolyte, including inorganic ceramics[102], "dry" polymer electrolytes where a lithium salt is incorporated into the solid polymer, gel electrolytes where a lithium salt containing organic solvent (or combination of solvents) is mixed with the solid polymer, and composite electrolytes where various fillers or nanoparticles are combined with the solid polymer[103].

In general, solid electrolytes have a significant burden of expected properties they must aspire to: good conductivity and transport of lithium ions, stability over a wide electrochemical range, durable to various thermal and chemical environments, safety, and good contact with the electrodes. A perennial detractor of solid electrolytes is their lower conductivity compared to liquid electrolytes. Polyethylene oxide (PEO), a common polymer electrolyte, had a room temperature conductivity of 10^{-8} S/cm when it was first developed[104], compared to an order of 10^{-2} S/cm for liquid organic solvents. This has improved over time, but it's an ongoing balancing act. Ion transport is easiest in amorphous sections of polymer, as the interaction between the lithium and the polymer is less rigid. However, the lower the crystallinity, the mechanical stability of the polymer suffers. Slower transport properties also mean that concentration polarization is more of an issue in solid polymers. Immobilizing anions could potentially fix this, but reducing the mobility of charged particles will also reduce the conductivity of the system overall.

Even after one finds a balance between the amorphous and crystalline phases, the conductivity and the mechanical stability, one must still concern themselves with the regular distribution of crosslinking within the polymer. Irregularity within the polymer can cause inhomogeneity in the current distribution across the electrode, which can cause uneven growth in the SEI and/or the nucleation of dendrites.

The interface between the electrode surface and the electrolyte is also a significant factor in the cyclability of the cell for this reason, because it needs to be good enough (here meaning low impedance and high homogeneity) to prevent inhomogeneous current distribution, but hopefully not so strong that it immobilizes a layer of polymer near the electrode surface and hinders ion transport. Although solid electrolytes can be more stable than liquid electrolytes in certain circumstances, they can also break down at the lithium surface. To increase conductivity in solid polymer electrolytes, gel electrolytes are often used[104] – incorporating organic liquid electrolytes into the cell. With these liquid electrolytes come the same undesirable SEI products as before: LiOH, ROLi (where R is an alkyl group), $LiCO_3$, RCOOLi, etc. Solid polymer electrolyte on its own is stable at a higher voltage, but if that is exceeded lithium salts have been shown to build up on the lithium surface[103]. Although a lithium salt rich SEI was shown to suppress dendrites, these cells can still fail. With ceramic electrolytes, high valence state components in the ceramic can become unstable at the lithium surface and reduce[105] – forming what is referred to as a mixed conducting interphase.

Many of these issues arise from bulk properties of the solid electrolytes acting for the whole cell. Used at the appropriate voltages, a pure solid polymer can be stable against the surface of the lithium, but it suffers from conductivity issues and is more likely to lose contact with the electrodes as it simultaneously shifts against the anode and cathode during cycling. The surface of the lithium anode is the most relevant area for the solid electrolyte to be in contact with to prevent dendrites. It follows that there is increasing interest in the application of a protective layer of solid electrolyte to the lithium surface to act as an artificial SEI in a cell that primarily contains liquid electrolyte. By significantly decreasing the thickness of the polymer, one also decreases the conductivity drop as the ions travel through it. Selecting polymers with the right mechanical properties allows the artificial SEI to compensate for volume changes in the electrode and maintain contact during cycling, unlike ceramic solid electrolytes which can fracture in these conditions[106]. To compensate Yang et al.[106] mixed garnet and polymer for its increased stability against the lithium. Zheng et al.[107] showed their polymer able to withstand significant distortion from the point of a needle without the needle piercing through. Acting on the surface of a lithium electrode, cycling stability was increased when compared to a bare lithium electrode. Similar improvements were shown when polydimethylsiloxane (or silly putty) was used as the coating[108, 109]. In these cases, the polymer is applied directly to the copper and the lithium is deposited between the two layers. Other groups have chosen to apply the coating directly to the surface of the lithium electrode. Li et al.[110] used in-situ AFM to show that a lithium polyacrylic acid (LiPAA) coated lithium electrode had a significantly smoother surface during plating and stripping when compared to a bare electrode. Tu et al[111] directly

applied their ionomer to the lithium surface at different thicknesses to find the ideal for cycling. The thinnest coating had the lowest impedence and highest coulombic efficiency overall.

Having established that a polymer coating on lithium has the potential to be an effective dendrite prevention strategy, significant work remains to optimize the technique. In addition to determining the best polymer coating for a particular system, one must also consider the parameters of polymer molecular weight, coating application process, coating thickness, etc. Cycling a matrix of cells with these parameters for a significant number of cycles can take hundreds of hours per cell. Here, I intend to show how the performance of different polymer coatings can be predicted using the baseline established in the course of this work, saving researchers the need to perform long term cycling on every variation of their dendrite suppression technique. This leads to Hypothesis 5.

Hypothesis 5. A repeatable and significant increase in stable continuous deposition without irregular growth in a cell, compared to an established baseline, is indicative of improved long term cell performance.

3. Experimental Techniques

3.1 Morphological Characterization

3.1.1 Scanning Electron Microscopy (SEM)

Scanning electron microscopy allows scientists to image the morphology of their samples down to the nanometer scale. It works by passing a focused beam of high energy (5-30 kV) electrons over a sample in a vacuum environment, which causes various effects within the sample – most importantly the emission of secondary and backscattered electrons. These electrons travel through the vacuum to reach one of two detectors, depending on the mode of interest. Secondary electrons are created by the inelastic collision of the primary beam electron with an atom, emitting a low energy (~50 eV) electron from the k shell of the atom. This electron has a low enough energy that it can be electrostatically collected by an Everhart-Thornley detector without disturbing the main beam of electrons. Secondary electrons are harvested from relatively close to the sample's surface and are best used to give a finely detailed picture of surface morphology. Backscattered electrons result from the elastic collision of a beam electron with an atom and can have energies up to the operating voltage. This is too high energy for the Everhart-Thornley to attract them and so a solid state detector is in place instead. Heavier Z elements are more likely to backscatter electrons and therefore, this technique can be used to show relative elemental composition in addition to general surface morphology

3.1.2 Nano-resolution X-ray Computed Tomography (nano-CT)

The Zeiss Xradia UltraXRM-200 nano-CT is an X-Ray imaging technique notable for its ability to nondestructively investigate materials at a subsurface level with high resolution. A diagram of the system's internal optics is shown in Figure 3.1. Cu K alpha X-Rays are generated and passed through a chromium filter to remove lower energy X-Rays that would otherwise result in beam hardening artifacts. After passing through the sample, the photons encounter the zone plate lens, which is made up of precisely spaced high aspect ratio gold rings. The diffraction from the outermost rings of the zone plate lens is responsible for the high resolution of the instrument.[8]

The Zeiss system has two zone plate lenses, corresponding to the two scales of imaging possible with this instrument: Large Field of View (LFOV) and High Resolution (HRES). The former has a 65 μm field of view and an optical resolution of 150 nm and the later has a 16 μm field of view and an optical resolution of 50 nm. In addition, there are two imaging modes to choose from: absorption and phase contrast. For absorption mode, which only considers the X-Ray attenuation through the sample, only the zone plate lens is required – the light is diffracted directly from the lens onto the detector. As with the backscatter electron technique, absorption mode can be used to determine the relative elemental composition, as higher Z elements are more likely to absorb X-rays. Certain SEI components, such as LiF and Li_2O, contain higher Z elements than graphite and thus the build-up of SEI could hypothetically be tracked using the nano-CT. Especially when overlaid with the phase contrast data, which more clearly images the graphite itself, as explained further in this section. This forms the basis of Hypothesis 1.

Hypothesis 1. The higher Z components of the SEI will increase the local X-ray absorption signal of a cycled graphite anode (versus an as received anode) enough that SEI growth in the internal anode pore structure can be observed by comparison of the absorption and phase contrast nano-CT data.

A limitation of absorption mode nano-CT is that even if it is used to track SEI growth through a marked increase in absorption, it cannot directly identify the SEI species in question. Each SEI is uniquely formed depending on the cell setup and electrochemical conditions, made up of a wide range of potential components in different configurations. The nano-CT can only report the cumulative attenuation of the X-Ray beam from all of these components as it moves through the entire volume in question. Disentangling how much attenuation could have come from one potential SEI species over another at different weight percentages and/or densities is incredibly nontrivial.

Phase contrast mode is used to image less attenuating materials with lower Z and/or density, such as graphite and lithium. Here, the boundaries between material phases are highlighted by the introduction of a gold Zernike phase ring between the sample and the detector. This phase shifts undiffracted light with reference to the photons which are diffracted by phase boundaries, making those phase boundaries significantly more apparent. Therefore, one can distinguish the outline of graphite particles or, hypothetically, the surface morphology of a lithium electrode. At the start of this work, no group had published a successful attempt to image lithium using nano-CT. However,

preliminary phase-contrast X-ray radiographs of lithium samples showed some lithium distinguishable from a copper wire, and thus Hypothesis 3 seemed possible.

Hypothesis 3. Despite the low Z of lithium, the phase contrast mode of the nano-CT will be able to observe significant sub-micron morphological features of lithium dendrite morphology.

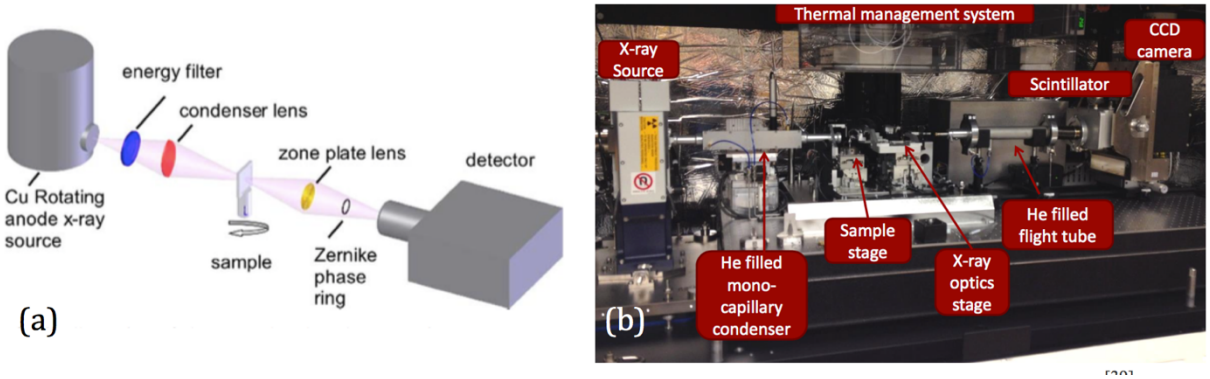

Figure 3.1. (a) X-ray optical components of the nano-CT in phase contrast mode, from Tkachuk et al.[8] (b) Internal view of the nano-CT[9].

During imaging, the sample rotates 180°, stopping to take a 2D radiograph at a set number of angles determined by imaging parameters. This collection of 2D radiographs is then reconstructed to a 3D dataset. When preparing a sample for the nano-CT, it is important to choose a sample that fits within the field of view, as reconstruction is only possible for the subsection of the sample that was present within the field of view for the entire rotation. Samples that are too large can also overattenuate the X-ray beam, decreasing the signal to noise ratio.

4. How SEI Growth Alters Graphite Anode Pore Morphology

This work has been published in The Journal of the Electrochemical Society.[112]

4.1 Introduction

The first degradation mechanism we investigated was the formation of SEI, where we were specifically interested in understanding how the internal pore structure of the graphite anode was affected. The surface of SEI layers has been thoroughly studied using a variety of techniques, such as SEM, XPS, FTIR, etc.[14, 113, 114] In order to investigate the structure of the SEI inside the anode, the most likely methods would be focused ion beam SEM (FIB-SEM) or X-ray computed tomography (XCT). FIB-SEM has the potential to probe the depth of the SEI, but the technique itself is destructive and has previously had issues with regards to graphite based anodes due to the resistance of the graphite to ion milling[115, 116] and contrast issues between the carbon of the electrode and the filling epoxy.[117] It can be used with alternative anode materials, however: recently, Etiemble et al.[118] probed the morphological effects of cycling on Si particles, and found varying effects on the porosity of the cell and the percentage of the anode volume that could be estimated to come from SEI due to the combined effects of sample expansion and cracking and SEI growth.

XCT is a nondestructive X-ray microscopy technique that collects 2D radiographs of the sample as it rotates and then reconstructs those into a 3D representation of the sample and its internal structure. The optional use of a Zernike phase contrast ring enables the instrument to resolve low atomic number (Z) elements, such as carbon, that have low X-

ray absorption contrast. Micron resolution XCT (micro-CT) was used by Lim et al.[119] to compare two commercial mesocarbon microbead (MCMB) anodes – one as received and one that had cycled until its capacity had decreased by 10%. Their findings were that the porosity increased with cycling, but their instrument lacked the resolution to fully explain this and they did not examine the change in X-ray absorption between the two samples to investigate the build up of SEI.

Nano-CT has been used previously to characterize various cathode[117, 120-123] and anode materials[124-126] for Li ion batteries, as well as materials relevant to other battery chemistries such as Zn air[127], and Sn.[128] Work specifically on graphitic electrodes has focused on the morphology of pristine commercial cells[115,116]. To our knowledge, no study has characterized the porosity of a graphite anode before and after failure-inducing cycling to determine the effect of SEI build up not only on the surface of the graphite, but also within its internal pores. In this chapter, we demonstrate for the first time that nano-CT can be used to probe the internal formation of these SEI layers, and that the data indicate a significant decrease in the relative pore volume and pore size between as-received and deeply and continuously cycled commercial graphite anodes that have been harvested from off the shelf cells.

In order to conduct this study, we exposed our sample to the atmospheric air within the nano-CT. Previous X-ray photoelectron spectroscopy (XPS) studies have looked at the effect of air exposure on SEI layers of graphite and found that although lithiated graphite exposed to air shows an increased signal from SEI species on the surface[129], delithiated

graphite had an increased graphite signal after air exposure – as the SEI components reacted with air to form volatile species that left the sample[130]. These studies were concerned with analyzing a change in the chemical speciation of the SEI layer on a scale of nanometers to tens of nanometers, whereas in this study we image and evaluate changes in the electrode morphology before and after cycling at length scales of 150 nm and larger. For this experiment, the anodes were completely delithiated prior to disassembly, and as such we would not expect a significant solid volume change upon exposure to air.

4.2 Experimental

We have studied two commercial 18650 cells (NCR18650B, Panasonic, Japan) from the same production lot, one in the as received state (referred to as the "pristine sample") and one after it had been cycled under galvanostatic charge/discharge conditions at +/- 1 A (approximately a C/3 rate) between 2.5 and 4.2 volts (with no constant voltage or open circuit dwelling) until cell failure (referred to as the "cycled sample"). The last step was a discharge one to delithiate the graphite as much as possible. A battery tester (BT200, Arbin Instruments Inc, USA) was used for this test, and all cycling was done under lab-ambient temperature conditions of 23 to 25˚C. The failure mode consisted of the cell exhibiting extremely high polarization and thus the inability to be cycled through any appreciable capacity within the specified voltage range. The cycled and pristine cells were then fully discharged and carefully cut open under air atmosphere and the graphite anodes were separated from the other battery components by peeling them apart with tweezers. Attempts were made to evaluate the

density of fresh and cycled electrodes based on sample mass and volume. Unfortunately, the cycled electrodes were not mechanically stable enough to allow for accurate external volume measurements for calculating density. Subsections of the pristine and cycled anodes were cut with razor blades to a pointed tip of an appropriate size for the nano-CT field of view (65 μm).

The samples were analyzed using a laboratory-scale nano-CT (UltraXRM-L200, Zeiss, USA) with an 8 keV rotating copper anode X-ray source. Large field of view tomography data was collected in the absorption and phase contrast imaging modes with an optical resolution of 150 nm and a voxel resolution of 65 nm. The absorption contrast imaging relies on the attenuation of the signal from higher Z material, and thus it can highlight the presence of electrolyte salts depositing on the anode. The absorption data was normalized relative to the signals of a gold fiducial marker and the air atmosphere surrounding the sample for both data sets, such that they could be quantitatively compared. The fiducial was applied using a single horsehair lightly coated with gold powder (1.5-3 μm in diameter) controlled through a micromanipulator to lightly brush the surface of the graphite sample. The resolution was such that it was possible to see when a single gold fiducial had transferred from the horsehair to the graphite. The field of view of the nano-CT was manipulated so that the fiducial stayed within the field during the full imaging process.

Unfortunately, the features of the low Z graphite anode are difficult to resolve by absorption at 8 keV. Therefore, we used the instrument's Zernike phase contrast mode that uses a phase contrast ring that phase shifts the undiffracted X-rays after the sample, such that they interfere with the sample diffracted waves, creating characteristic light and dark halos at said boundaries and making them significantly more apparent to the eye. The sample was rotated 180° with radiographs collected at regular intervals (for a total of 901 images). In absorption mode, each radiograph required a 60 second exposure, while the phase contrast mode radiographs required 120 seconds. The collected radiographs were reconstructed using Zeiss's commercial filtered back projection algorithm into 3D data that could be visualized using Avizo Fire (FEI Visualization Sciences Group, USA) software. Segmentation of the Zernike phase contrast images into pore and solid domains requires special consideration because the image is composed of halos at interfaces rather than bulk attenuation. Thus, standard segmentation algorithms that use absorption intensity are ineffective. Herein, we use our custom code developed in Kumar et al.[131] to correct the phase contrast artifacts and provide an image that can be segmented based on thresholding. The code does this by computationally inverting a model of the diffraction optics to obtain the volumetric sample shape. The pore size distribution was based on a distance transform method with a spherical Kernel.

4.3 Results

Figure 4.1 shows the electrochemical performance of the cycled sample. The cell steadily decreased in discharge capacity as a function of cycling until an erratic drop off

occurred, corresponding to complete cell failure. Figure 4.1b shows that this behavior is linked to an increased series DC resistance with cycling. Figures 4.1c and 4.1d indicate how the charge/discharge profiles and differential capacity of the cell evolved through the 1st, 200th, and 400th cycle. There is a more distinct shift to lower discharge capacity between the 200th and 400th cycles than between the 1st and 200th cycles. This is also apparent in the differential discharge capacity, where the peak shifts to a significantly lower voltage for the 400th cycle compared to the 1st and 200th cycles. The manifested losses are most consistent with a mode wherein a potential-limited charge termination condition increasingly limited the amount of capacity able to be charged prior to reaching the maximum voltage setting. This reduced capacity is consistent with an increased internal resistance of the cell.

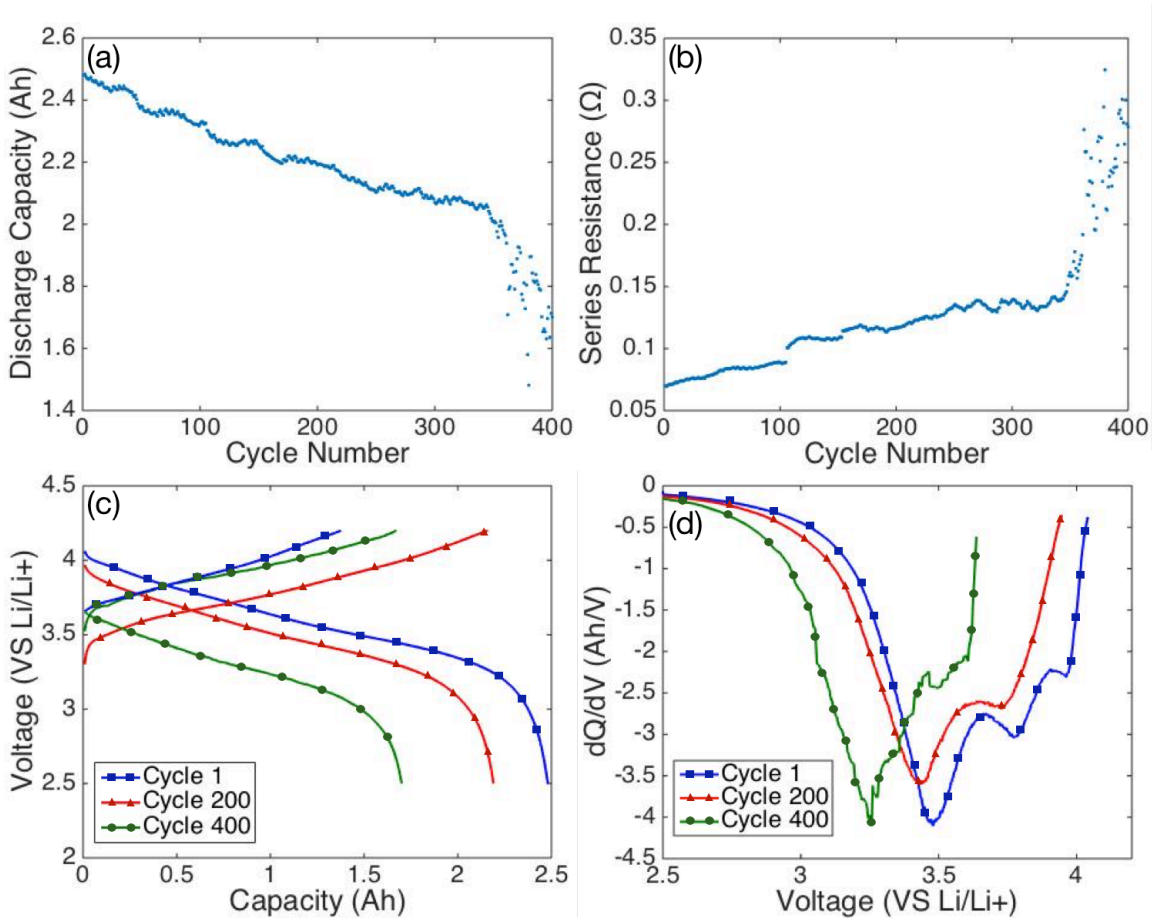

Figure 4.1. Electrochemical performance data of the cycled cell. (a) Discharge capacity fade as a function of cycle number and (b) series resistance increase as a function of cycle number. (c) Charge and discharge curves at the 1st, 200th, and 400th cycles. (d) Differential discharge capacity for the 1st, 200th, and 400th cycles.

Figures 4.2a and 4.2b show SEM images of the pristine and cycled anode surfaces. In the pristine sample, the graphite sheets are distinct, whereas in the cycled sample, the surface is thickly covered by a smooth, continuous SEI layer, restricting Li transport and resulting in the failure seen in Figure 4.1. These data are consistent with other surface observations of SEI formation.[40, 132, 133]

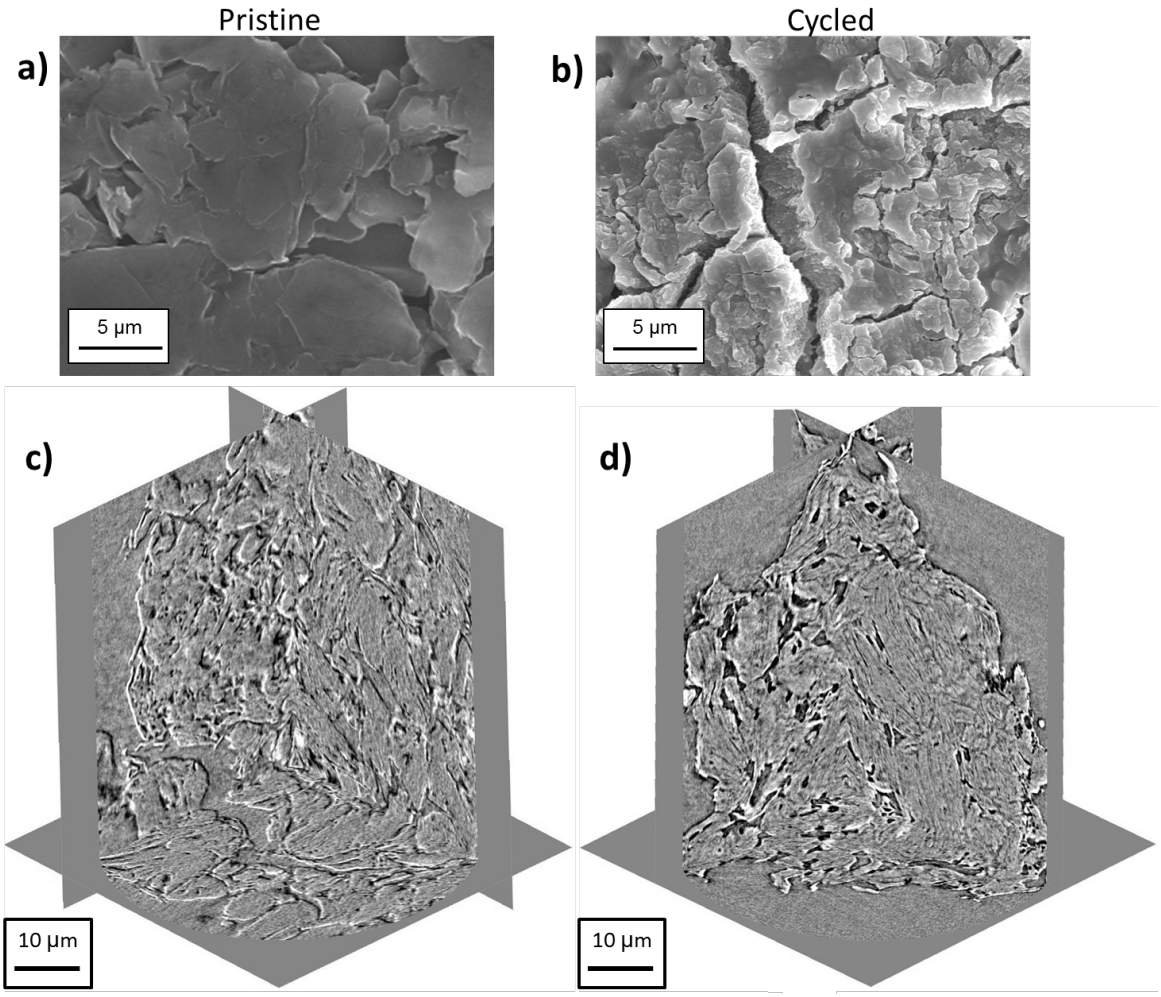

Figure 4.2. Comparison of the pristine and cycled sample morphologies from raw images. SEM images of the (a) pristine and (b) cycled samples. Orthogonal virtual slices of the reconstructed X-ray phase contrast 3D images for the (c) pristine and (d) cycled anodes.

Figures 4.2c and 4.2d show X-ray micrographs of the pristine and cycled samples. As was observed in the SEM images, the graphite particles are distinct before cycling. In addition, the nano-CT shows the pore channels running through the electrode. After cycling, these pore channels have decreased in size and the graphite particles appear more tightly packed. The SEI layer cannot be distinguished from the graphite in these

phase contrast images. The Zernike phase contrast imaging mode reveals the internal morphology of the samples, but due to its lower Z-contrast it cannot distinguish the graphite and the more X-ray absorbing elements (i.e., fluorine) in the SEI layer. For that, we rely on the X-ray absorption mode images shown in Figures 4.3d-g. From those images we observe that it is not merely the surface morphology and pore structure that is affected by cycling, but the elemental composition has also changed. In order to quantitatively analyze this affect, internal subsections of these samples were segmented separately to ensure that external void surrounding the sample was not erroneously counted as pore volume. For adequate statistical comparison, the sub sample sizes were approximately four orders of magnitude larger than the average volume of pore we examined. Semi-transparent volume renderings of the solid in these subsections are shown in Figure 4.3a and 4.3b, clearly highlighting a reduction in internal pore volume. Figure 4.4 shows surface renderings of the segmented pore volume in the same subsections.

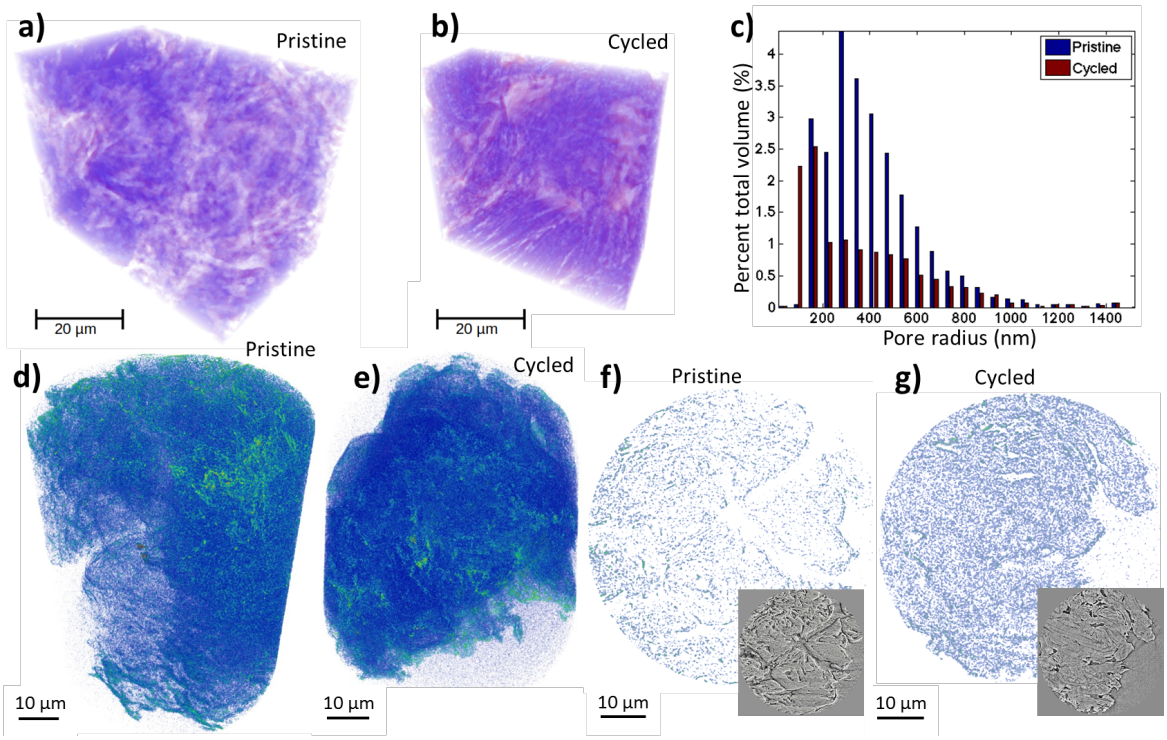

Figure 4.3. (a,b) 3D volume renderings of subsections from the (a) pristine and (b) cycled anodes' phase contrast images that are used for quantitative analysis. The images have been corrected for phase contrast artifacts with solid shown as purple. (c) Pore size distributions of the pristine and cycled sample subsections. (d,e) Volume renderings of 3D absorption data for the full (d) pristine and (e) cycled anodes. (f,g) Virtual slices of the higher intensity (higher Z) signal for the (f) pristine and (g) cycled anodes with insets showing the corresponding phase contrast virtual slices.

Figure 4.3c shows the quantitative size distributions for the segmented pore volume of the subsections (see Figure 4.4). The pristine sample was comprised of 25% pore volume, whereas only 12% of the cycled sample volume was pore. One can also see that the pristine sample has a larger percentage of bigger pores relative to its total pore volume when compared to the cycled sample. A potential cause of this is suggested by

comparing the absorption data of the two samples. Figures 4.3d and 4.3e show the 3D reconstruction of the absorption data from the full field of view for the pristine and cycled samples, while Figures 4.3f and 4.3g emphasize the difference between the two data sets by showing virtual slices (325 nm thick) of the absorption contrast from both. There is a shift between the pristine and cycled samples to a much denser high Z signal throughout the anode. The volume integral of the absorption signal within the same sub-volumes as Figures 4.3a,b was 50% higher in the cycled anode relative to the pristine anode.

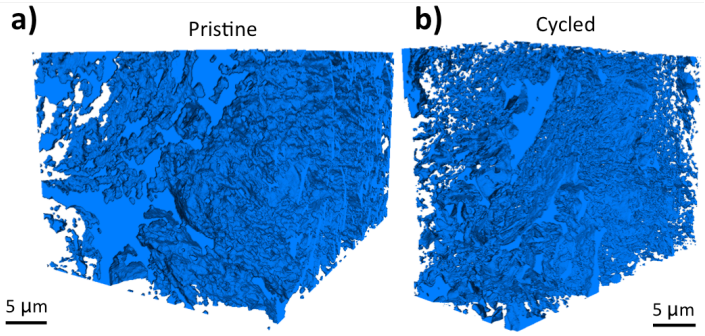

Figure 4.4. Surface renderings of the segmented pores for the a) pristine and b) cycled graphite anodes.

4.4 Discussion

We now discuss these results, correlating the electrochemical data with the nano-CT imaging to better understand the anode degradation. Figure 4.1 shows the correlation between an increase in series resistance within the cell and capacity fade, a connection that has been previously linked to the growth of passivation films on the electrodes.[16] Recent work proposed that material reduced on the anode originated as a side oxidation product (e.g., F^- species) at the cathode.[39, 40] This could suggest that the

buildup occurs primarily at the interface of the anode with the separator. From Figure 4.2a and 4.2b, one can see a clear accumulation of less conductive material at the graphite surface. However, surface characterizations, such as SEM, do not allow us to see how the internal structure of the anode is affected.

The 3D X-ray micrographs of Figure 4.2c and 4.2d depict a general collapse of pore structure throughout the volume of the cycled anode compared to the pristine anode. Looking specifically at internal subsections of the two samples, this reduction in pore volume can be seen qualitatively in Figures 4.3a and 4.3b and quantitatively in Figure 4.3c, possibly caused by the growth of a solid layer extending beyond the surface of the graphite. Figure 4.3c also shows that the difference in the pore size is on the order of hundreds of nanometers – indicating the difference between the two samples is indeed a large morphological change beyond any effects of exposing the sample to air that were observed at the nanometer length-scale in prior XPS studies. By comparing the relative amounts of higher absorption (and thus higher Z material) signal in the pristine and cycled samples in Figures 4.3d-g, one can see a significant increase in the absorption signal in the cycled sample (50% higher). This suggests that the pore closing phenomenon is, at least partially, caused by the buildup of deposited material within the sample itself. Cycling may also have a role in compacting the structure.

4.5 Conclusions

For the first time, nano-CT tomography was used to investigate the structure of SEI build up in commercially produced Li-ion cells that experienced complete failure as a

result of continuous deep cycling. The nano-CT analysis resulted in well resolved 3D reconstructions of the anode structures with indications of SEI materials in addition to the graphite host structures. It was found that the SEI material extended into the internal structure of the graphite anode, with a marked decrease in internal pore diameter when comparing the cell before and after cycling to failure. The sudden failure of commercial cells was linked to a dramatic increase in series resistance, which we link here, at least in part, to the growth of SEI both on the surface and within the pore structure of the graphite anode. Separating the relative contribution of the increased anode resistance to the total increased resistance at end of life is an important avenue of ongoing work within the community. A comparison between the relative amount of build up at the surface of the anode and within the pores was beyond the scope of this analysis and remains open as a topic of further study.

5. Effect of Cycling Conditions on Lithium Deposition Morphology

This work has been published in ACS Applied Materials & Interfaces.[134]

5.1 Introduction

In this work, we intend to build upon the discovery of Harry et al.[7], who used micro-CT to reveal subsurface growth in lithium films during deposition that ultimately lead to dendrites. When we started this project, it had not yet been shown that a laboratory scale nano-CT technique could be used to successfully image low Z lithium, let alone in its less dense dendritic form. Therefore, the first objective of this study was to demonstrate that the nano-CT with the aid of Zernike phase contrast optics for low Z materials can resolve Li at this scale. The second objective of this study is to gain insight into the effect of temperature (5 vs 33 °C) and current density (2.4 vs 40 mA cm^{-2}) on the morphology of cycled Li electrodes. The two current densities are chosen to reflect a low current density (LCD) where Li-stripping and deposition should be uniform and high current density (HCD) where there can be mass transport and kinetic limitations. Rather than studying a single constant current electrodeposition typical of prior imaging work, the lithium morphologies are the result of 30 galvanostatic charging and discharging cycles in order to mimic Li-metal battery operation. In our HCD experiments, we encountered significantly increased impedance with stripping that have been previously attributed to the formation of 'dead lithium'. In these cases, the cell voltage was allowed to rapidly rise from the stable potential (~1 V vs. Li/Li^+) to high potentials (3-6 V vs. Li/Li^+) over 1-2 s before the Li stripping portion of the cycle was terminated. This is consistent with abusive charging, particularly in battery packs, which

can induce electrolyte decomposition and copper current collector dissolution. The resulting samples were then analyzed with the nano-CT, and the data was processed to correlate the effects of temperature and current density on the external and internal morphology of the deposited Li films.

5.2 Experimental

5.2.1 Sample preparation

As shown in Figure 5.1, the cycles of electrodeposition and stripping of Li were carried out on 80 μm diameter copper wire working electrodes (99.9%, McMaster-Carr) that were submerged to a wetted length of 0.5 cm in a beaker cell (20 mL) filled with 1M $LiPF_6$ in battery grade EC:DEC 1:1 v/v (Aldrich). The counter/reference (CE/RE) electrode was a strip of 0.75-mm thick lithium metal (99.9%, Aldrich). An Ar-filled glovebox with continuous H_2O and O_2 monitoring was used to store all materials and contain the electrochemical experiments. H_2O and O_2 levels were measured to be <0.5 ppm through the deposition/cycling processes. The experiments were either performed at ambient temperature of the electrolyte bath (33°C) or with the bath cooled to a temperature of 5°C using a Peltier cooling assembly (Laird Technologies) powered by a DC power supply (E3611A, Agilent). The temperature of the electrolyte was measured with a Hg thermometer. The electrochemical measurements were performed using a potentiostat/galvanostat (PAR 263A) connected to a frequency response analyzer (Solartron 1260). Prior to cycling, an initial Li electrode was formed by *in-situ* electrodeposition of Li at a stable low current density of -2.4 mA/cm^2 for 1200 s to produce uniform non-porous Li coatings on the 80 μm diameter copper wire current

collectors. Subsequently, additional Li was electrodeposited and/or stripped over 29 cycles at different current densities between 33 and 5°C, as summarized in Table 1. In all samples the final (or only) step is a deposition step. After completion of the lithium deposition and cycling experiments, the lithium coated copper samples were removed from the electrolyte and sealed within a 320-μm inner-diameter polyimide tube (Kapton) with a 76-μm wall thickness using a two-component quick set epoxy glue (Loctite), thereby storing the sample in argon environment for transfer and imaging.

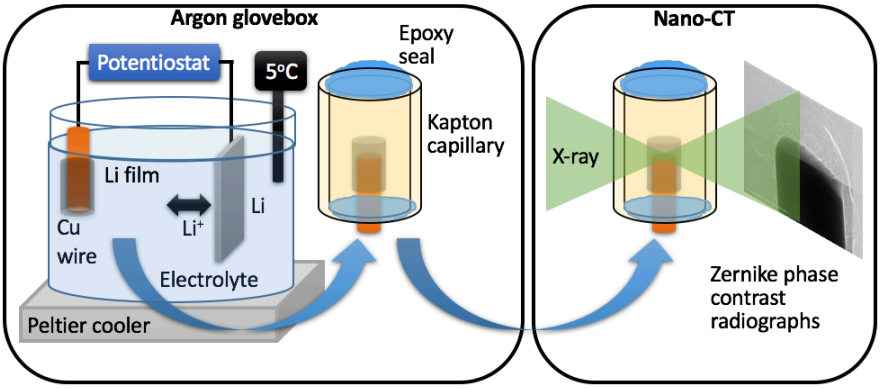

Figure 5.1. Lithium is electrodeposited in an Argon glovebox on 80-μm-diameter copper wire working electrodes submerged 0.5 cm into a temperature controlled Li-electrolyte and then cycled at different rates. The Li-coated wires are transferred to Ar-filled Kapton capillary tubes and sealed with epoxy. The samples are then transferred to nano-CT for X-ray imaging with Zernike phase contrast.

5.2.2 Nano-CT imaging and image processing

The samples were imaged using a nano-CT (UltraXRM-L200, Xradia, Inc., Pleasanton, CA) with a laboratory-scale 8 keV rotating copper anode X-ray source. The instrument uses a monocapillary condenser to focus the X-rays onto the sample with high efficiency. Following the sample, the image was magnified by a Fresnel zone plate

objective. The optics used here offer 150 nm resolution with a larger 65 μm field of view. In this work, a gold phase ring for Zernike phase contrast was inserted following the Fresnel zone plate objective to provide image contrast for low Z Li. The gold ring phase shifts the wave not diffracted by the sample, converting phase shift information into amplitude that can be detected by the scintillator and detector. Some of the diffracted wave also passes through the phase ring (the leaked diffracted wave), generating the characteristic halos of phase contrast. These halos are the bright-dark contrast found at material interfaces with significant differences in phase shift, including the Li and Ar interface.

For imaging, the samples encapsulated in the Kapton tube were vertically mounted using a simple clip-type sample holder. During the tomography scan, 451 radiographs with 2x2 binning for 130 nm pixels were collected over a 180° rotation with exposure times of 90 s. The collected radiographs were reconstructed using the instrument's filtered back projection algorithm software to produce the 3D image. One notable challenge of phase contrast imaging is the lack of volumetric contrast of low Z samples versus their surroundings. In Kumar et al.[131], a diffraction physics based algorithm that models the phase contrast optics was derived to retrieve an artifact-free version of the sample image than can be readily segmented. That algorithm and custom code were used herein to generate 3D volumes that can be segmented into Li, Cu, and void volumes presumably filled with Ar. Subsequently, the raw 3D tomography images and artifact corrected images were visualized using commercial software (Avizo, FEI Corporation) and analyzed using custom Matlab codes (Mathworks, Inc., Natick, MA).

Void size distributions were computed using a common combination of image erosion and dilation operations with a spherical kernel.

5.3 Results

5.3.1 Imaging of Li foundation layer on Cu wire

We first confirm that nano-CT can be used effectively to image a thin Li electrode foundation layer electrodeposited on a copper wire. The potential-time series is shown in Figure 5.2a for the electrodeposition of lithium at 30 μA onto the Cu wire (2.4 mA/cm^2) for 1200 s at 33°C. Quantitatively, 30 μA applied to the 0.013 cm^2 of wetted wire surface in the electrolyte is equivalent to 0.036 C over 1200 s and the deposition of 3.7×10^{-7} moles of Li. Using the density of 0.534 g/cm^3 for Li metal and its molecular weight of 6.941 g/mol, this corresponds to 4.8×10^{-6} cm^3 of Li, or a theoretical 4-μm-thick film over the submerged surface of the wire (see Table 5.1). Within the first 20 s, the potential exhibits a sharp drop from a positive value towards a minimum at approximately -0.3 V. The potential minimum is observed only during the first lithiation of the Cu substrate and has been attributed to the additional overpotential required to overcome the heterogeneous nucleation barrier[135 136]. Stark et al. have suggested that the initial stages of lithium nucleation are substrate independent and involve hemispherical nuclei morphologies, which grow and eventually overlap[59]. Subsequently, the potential monotonically increases to a less negative value, reaching a steady state plateau of approximately -0.1 V at 1200 s. This potential is representative of the minimum overpotential required to maintain the electrodeposition process at this current density.

Table 5.1. Samples and cycling conditions

Sample ID	Deposition temperature (°C)	Deposition conditions	Theoretical deposition thickness (μm)
Formation layer	33 °C	1200 s at -2.4 mA/cm^2	4
10°C/CC	10 °C	1200 s at -2.4 mA/cm^2 + 476 s at -5 mA/cm^2	7
5°C/CC	5 °C	1200 s at -2.4 mA/cm^2 + 476 s at -5 mA/cm^2	7
33°C/LCD	33°C	1200 s at -2.4 mA/cm^2 + 29 cycles 60 s at ±2.4 mA/cm^2 + 60 s at -2.4 mA/cm^2	4.2
33°C/LCD-HCD	33°C	1200 s at -2.4 mA/cm^2 + 29 cycles 60 s at ±2.4 mA/cm^2 + 60 s at -40 mA/cm^2	7
33°C/HCD	33°C	1200 s at -2.4 mA/cm^2 + 29 cycles 60 s at ±40 mA/cm^2 + 60 s at -40 mA/cm^2	7
5°C/HCD	5°C	1200 s at -2.4 mA/cm^2 + 29 cycles 60 s at ±40 mA/cm^2 + 60 s at -40 mA/cm^2	7

Figure 5.2b shows the raw orthogonal virtual slices of the initial Li foundation layer from the reconstructed Zernike phase contrast tomography measured from nano-CT. The virtual slices show the distinct absorption contrast of Cu, but the Li can only be distinguished from the surrounding argon by dark/bright phase contrast halos at the interfaces. Figure 5.2c shows surface renderings of the Li and Cu obtained after correcting the Zernike phase contrast image using our diffraction optics model[131] and image processing to segment the Li, Cu, and surrounding Ar. The imaging shows that this initial electrodeposition leaves an approximately 8 μm thick layer of Li on the end of

the Cu wire. The layer is rough but without any notable voids or dendrites. Given the apparent variations in thickness over the roughened copper surface, there is reasonable agreement between the observed thickness and the theoretical uniform film thickness of 4 μm. Based on the thickness of the Li layer, the local time-average current density during deposition may have been as high as 5 mA/cm^2 at the tip of the wire.

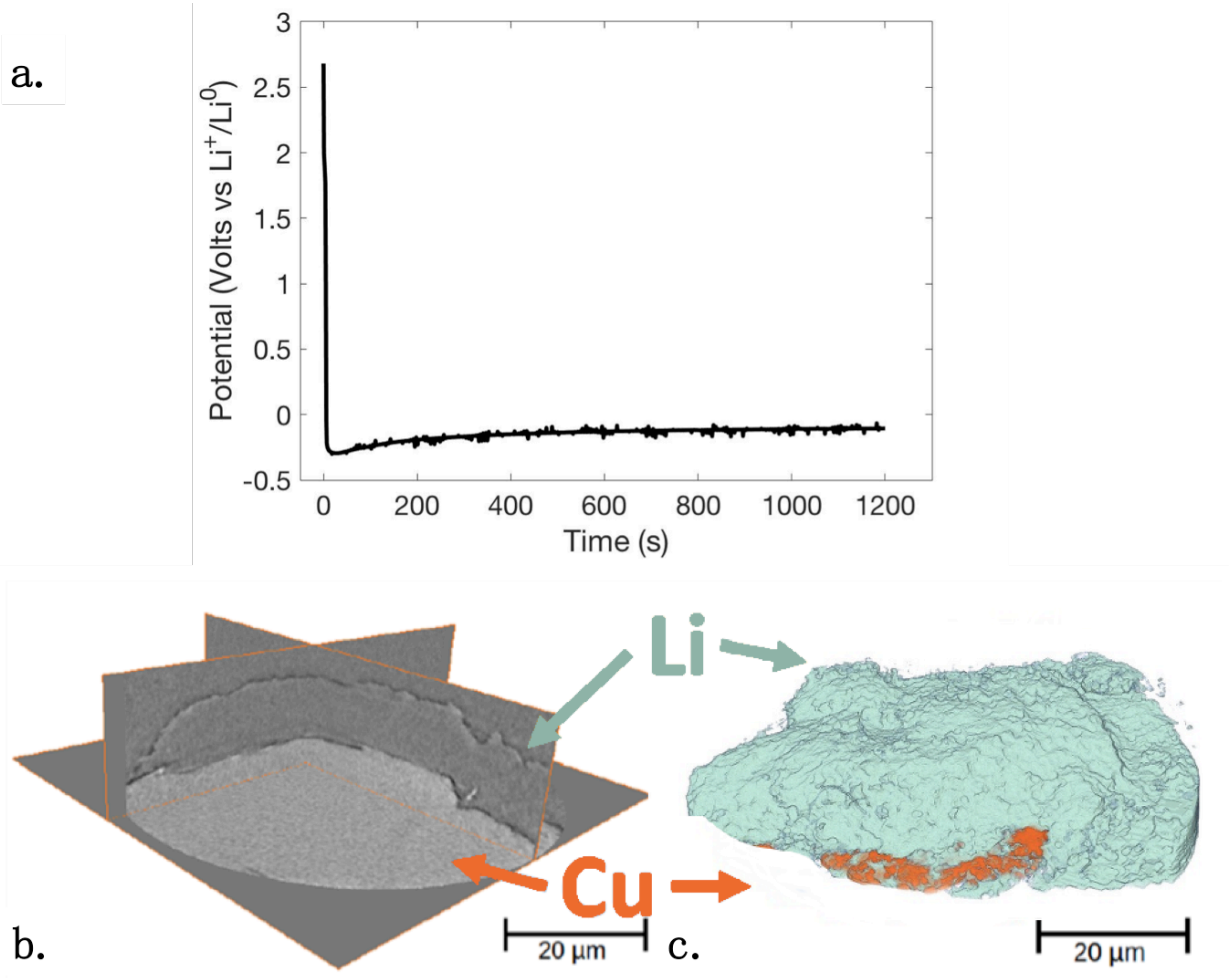

Figure 5.2. (a) Representative potential/time series of the electrodeposition of a Li foundation layer on the tip of a Cu wire at –2.4 mA/cm^2 for 1200 s at 33 °C, (b) Orthogonal virtual slices of the 3D reconstructed image of the Li foundation layer, (c) Phase contrast corrected and segmented surface rendering image of Li (light blue) on the Cu wire (orange).

This result confirms that the in-situ Li electrodeposition allows us to generate initial Li metal electrodes with only micrometer-scale roughness for subsequent studies on Li

cycling and dendrite growth, and that nano-CT with Zernike phase contrast can be used for imaging.

5.3.2 Imaging of Li films electrodeposited at 5 and 10°C

Similar procedures were used to deposit additional Li onto the initial Li foundation layer, but at the lower temperatures of 10 and 5°C with a current of 63 µA (-5 mA/cm^2) for 476 s, equaling a total theoretical thickness of 7 µm. The potential-time series for the -5 mA/cm^2 deposition is show in Figure 5.3a for the deposition at 10°C, and the one for the deposition at 5°C appears similar. The image of the film deposited at 10°C on the Cu wire in Figure 5.3b starts to show the presence of many large voids in the Li film. As evident in the image, the voids, which are not a result of cycling in this case, are quite large with internal dimensions on the order of 5-10 micrometers.

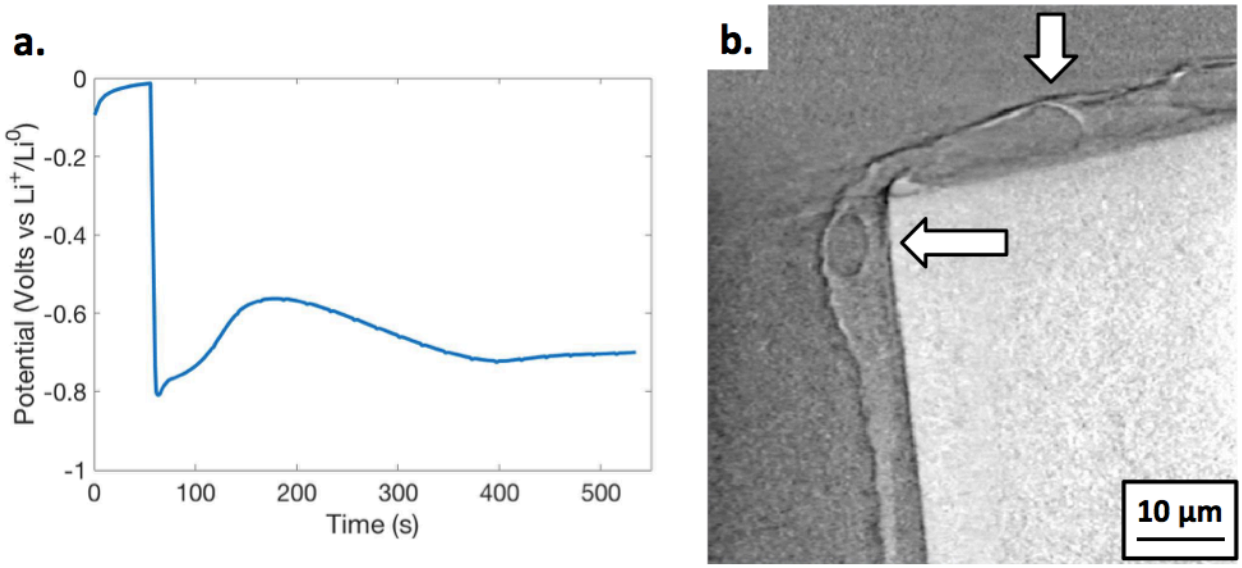

Figure 5.3. (a) Voltage time series for a -5 mA/cm^2 deposition of Li onto a ~8 µm formation layer of Li on the Cu wire at 10°C and (b) a virtual slice of nano-CT data.

5.3.3 Imaging of cycled Li films

Table 5.1 lists the samples with their respective electrochemical cycling conditions, where LCD and HCD indicate low and high current density (2.4 mA/cm^2 and 40 mA/cm^2), respectively. The Li electrodeposition/stripping steps were 60 s at either 2.4 mA/cm^2 or 40 mA/cm^2, corresponding the electrodeposition/stripping of an additional 0.2- or 3-μm-thick layer of Li over the initial formation layer of Li. For all samples, 29 cycles with 60 s deposition and dissolution steps were performed followed by one additional deposition. For one sample, labeled 33°C/LCD-HCD, the first 29 cycles at ambient temperature were performed with the low current density and the final deposition was at the high current density. Reductive current values are denoted as negative (–) values.

Figure 5.4 shows the potential time-series for the samples in Table 5.1. The results for the LCD samples in Figures 5.4a and 5.4b are nearly identical with each cycle occurring at potentials between 0.2 and -0.2 V vs Li^+/Li^0 because the cycling conditions were the same aside for the final Li-deposition step. For the cycling at higher current density (40 mA/cm^2) shown in Figures 5.4c and 5.4d, the first cycles are between -0.6 and 0.6 V for 5^{o}C and -1 and 1 V for 33^{o}C, with the higher potentials relative to the LCD samples reflective of the greater overpotential caused by the higher current density of the charge/discharge step. The higher potential for 33^{o}C versus 5^{o}C is likely due to difference in the electrode spacing in the bath and the corresponding ohmic overpotential. It is important to note that this experiment uses a two electrode arrangement and the voltages reported include the ohmic voltage drop through the

electrolyte. Assuming a 10 mS/cm electrolyte conductivity in this two electrode bath cell, the ohmic overpotential could reach values on the order of 1 V, which suggests the observed whole cell voltage is dominated by ohmic overpotential during the steady plateaus.

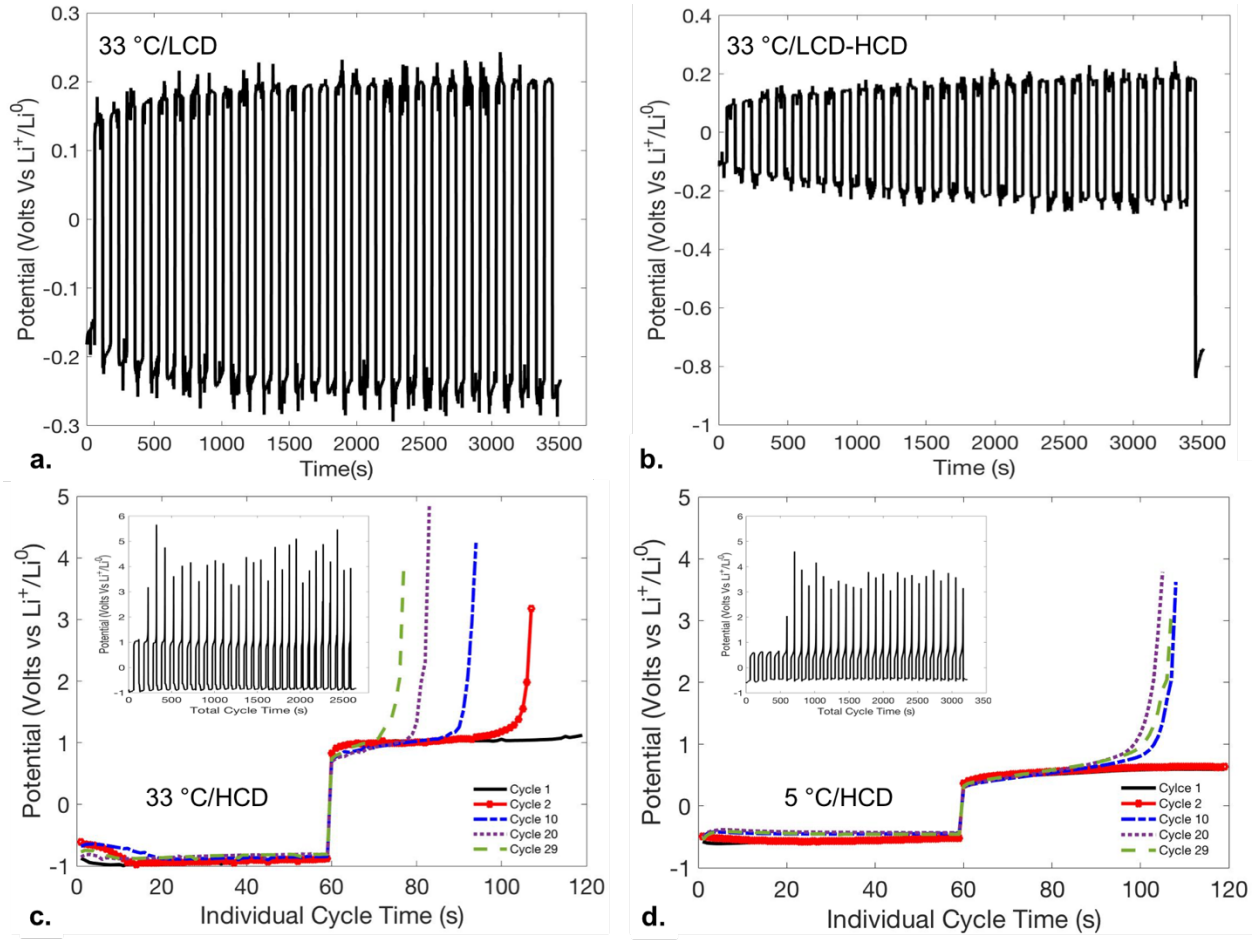

Figure 5.4. Cell voltage times series for (a.) 33°C/LCD, (b.) 33°C/LCD-HCD, (c.) 33°C/HCD with select potential transients, and (d.) 5°C/HCD with select potential transients.

On the 2nd cycle for 33°C and the 5th cycle for 5°C, a sharp rise in voltage occurs after an initial period of stable Li stripping. Due to delays in triggering the end of the stripping

cycle, the whole cell voltage rises to 3-6 V before electrodeposition resumes at negative voltage. The time spent above 3 V is minimal (1 s), but this corresponds to the potential at which the Cu substrate is thermodynamically prone to dissolution (3.3 V vs Li^+/Li^0)[137]. Though we see no evidence of significant or sustained side reactions, it is possible that these very brief excursions to high potential can alter the electrode interface through minor amounts of side reactions, including electrolyte decomposition and copper dissolution. In a worst case scenario, considering a 1 s duration of potential rise above the Cu dissolution reversible potential, each stripping could remove roughly 10 nm of copper. However, since the voltage does not plateau, it appears that the current during the high voltage transient is instead dominated by capacitive current that is charging the electric double layers at the electrode/electrolyte interfaces. At the most extreme voltage spike, a high estimate of the capacitance is 0.9 F/g, which is reasonable for the lower surface area copper wire when compared to the higher surface area carbons typically measured for their capacitance in organic electrolytes – typically at 10s-100s of F/g[138]. In contrast, the potential during Li electrodeposition remains comparatively constant throughout the cycles with the only apparent effect of cycling being a reduction in the overpotential at the beginning of the electrodeposition step.

Figure 5.5 presents the segmented nano-CT reconstructed images for all of the cycled samples from Table 5.1, including the orthogonal gray-scale virtual slices and the segmented 3D surface renderings after correcting the Zernike phase contrast images. Figures 5.5a and 5.5b show the structure resulting from the 33°C/LCD cycling (corresponding to the electrochemistry in Fig 5.4a). As discussed in the experimental

section, the 60 s, 2.4 mA/cm^2 deposition and dissolution should add and remove, respectively, a ~0.2 µm-thick Li deposit onto the original ~4-8µm thick initial layer. Considering the additional thickness observed in the deposition of the base layer likely due to non-uniform deposition, this LCD layer could be 0.4 µm thick at the tip of the wire. In either case, the relative amount of Li electrodeposited or removed during the cycle is small relative to the initial Li layer. The resulting structures after cycling exhibit a uniform Li layer, free of any notable internal voids or features, which appears to have conformally deposited onto the Cu wire.

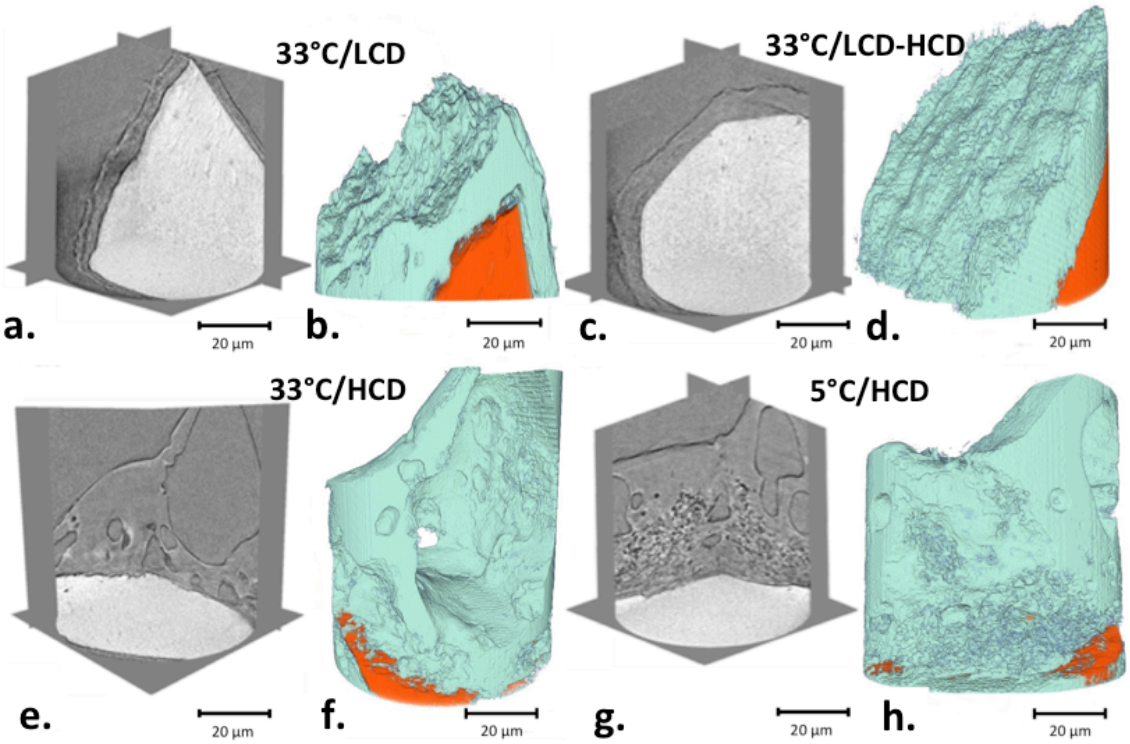

Figure 5.5. Orthogonal virtual slices (a., c., e., g.) and the respective segmented images from Zernike phase contrast correction (b., d., f., h.). Samples cycled at LCD (a. through d.) exhibit uniform and conformal Li layers, while those cycled at HDC (e. through h) depict non-uniform porous Li morphologies at 33°C and 5°C. The 5°C/HCD induces a significant proportion of clustered small voids.

Figures 5.5c and 5.5d for the 33°C/LCD-HCD show two images for the sample that underwent the same LCD cycling, but with an HCD during the last deposition (corresponding to the electrochemistry in Fig. 5b). The final high current density deposition should have deposited a 3.2 μm thick Li layer, corresponding to an additional thickness of 3 to 6 μm depending on the uniformity of the current density. The thicker film (~8 μm) is evident in the images when compared to the 33°C/LCD images in Figures 5.5a and 5.5b.

Figures 5.5e-5.5h show the dramatic change in structure observed when all of the cycling was done at HCD (40 mA/cm^2). The HDC conditions should ideally add and remove 3 μm of Li thickness if the Li addition and removal were uniform. The 33°C/HCD electrodes in Figures 5.5e and 5.5f show a non-uniform Li morphology containing large voids, similar to those observed during the single deposition experiments, shown in Figure 5.3. In these images, we can observe that the length scales of the continuous void and solid domains are typically greater than 5 μm and can be as a large as roughly 20 μm. Figures 5.5g and 5.5h show the images for the electrodes from 5°C/HCD cycling, where we observe a porous Li layer with a broad distribution of void sizes. Similar to the electrodes that experienced 33°C/HCD cycling, there are large voids with length scales on the order of 10 μm. However, the 5°C/HCD electrodes also have a significant portion of the clustered small (<3 μm) voids that are distributed across the entire thickness of the Li layer.

Given the notable difference in internal void morphology between the 5°C and 33°C cycling cases, we undertook a more detailed quantitative analysis to determine the utility in using nano-CT for examining voids in Li films. Figures 5.6a and 5.6b present the volume of the void domain extracted from the segmented sample, wherein the void volume was isolated as a region of interest and spatial void size distributions were evaluated on the basis of inscribed spheres. Observing the false-coloring of the spatial size distributions, we find the majority of the internal voids in the 33°C/LCD electrode are large and there are negligible small voids that would be shown as a dark shade in the image.

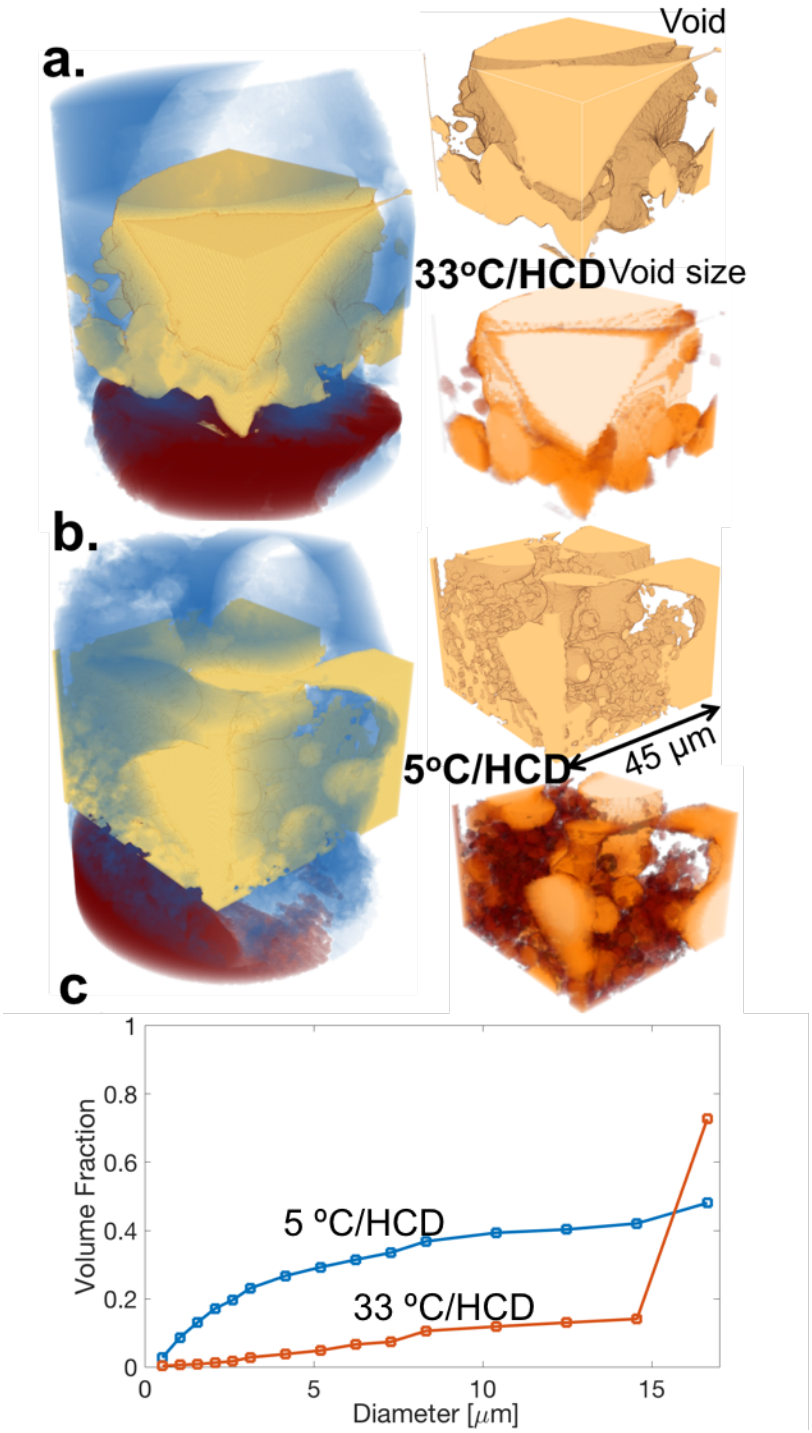

Figure 5.6. Internal void morphology analysis of a) 33°C/HCD and b) 5°C/HCD samples. Li is shown in transparent blue and Cu is opaque dark red. The representative void domains and spatial void size distributions are also shown. c) Comparison of the cumulative void size distribution on the basis of volume fraction.

In contrast, the spatial distribution shown for the 5°C/LCD electrode shows a high density of small voids that are tightly spaced. Figure 5.6c shows the cumulative distribution of volume fraction of void as function of inscribed sphere diameter. The cumulative distribution for the 33ºC sample shows that the dominant fraction (60%) of the void volume considered has diameters ranging from 3 to 8 μm. In sharp contrast with the 5ºC sample, we find that a large portion (55%) of the void volume features have diameters less than 3 μm. An additional observation is that both samples exhibit a significant contribution to the void volume with diameters of approximately 8 μm. It is important to mention that the small void features of the 5ºC sample would not be resolved by the typical resolution of micro-CT or optical microscopy, which highlights the value of nano-CT imaging.

5.4 Discussion

Dendritic growth has an inherent fragility due to its relatively tenuous connection to the electrode. It is possible that by removing the samples from the electrolyte they were cycled in and transferring them to the nano-CT, the ex-situ morphology imaged there differs from its original state. The time between cycling of the samples and imaging varied, but was on the order of days. If the sample continued to alter after removal from the electrolyte, for instance via surface diffusion, the changes were not drastic enough to alter the findings of this study. With sufficient energy, the samples would shift to a more stable state and continue to do so. Significant mass shifts would be revealed in the imaging, which requires that the sample remains static on the order of nanometers

for at least twelve hours. We experience no major issues with sample movement during imagining. The voids we examine here are on the order of microns. Research continues toward the ultimate goal of in-situ imaging of lithium cycling at dendritic conditions, where a more precise understanding of these phenomena could be possible. Until then, this work seeks to understand the gross change in morphology that occurs between significant shifts of temperature and current density.

For the LCD cycling, we observed no significant voids or dendrites after both 1200 s of deposition and repeated 60 s cycles. This uniform coating was also found for an additional initial Li layer sample that was deposited at 5^{o}C at the lower current density of 2.4 mA/cm^{2} for 1200 s. This suggests that at sufficiently low current densities, internal voids and dendritic structures can be suppressed and uniform morphologies can be achieved. We additionally found that a single high current deposition at 33^{o}C following low current cycling in the 33°C/LCD-HCD electrode, did not induce porous or dendritic growth (see Figures 5.5c and 5.5d).

The high current morphologies with significant internal voids observed here are a departure from the needle-like or branching tree-like structures sometimes observed previously at high currents or with extended galvanostatic electrodeposition, on the order of hours, which may not be representative of battery cycling. However, the structures resemble well the porous Li produced by Lopez et al.[139] after 50 cycles of Li deposition and dissolution at a current density of 2.0 mA/cm^{2} using an ethlylene carbonate: ethyl methyl carbonate (EC:EMC) electrolyte. Causes of porosity during

electrodeposition can generally be classified into two classifications: crystallographic and inclusion[140]. Crystallographic porosity is a result of lattice effects or structural defects stemming from the substrate. Inclusion porosity arises from foreign or electronically insulating species, such as gases[141], that persist throughout the deposition process for some finite amount of time and forms voids. In fact, gases evolved during the electrodeposition process often influence the porosity of the resulting morphology[142 143]. We rationalized that both porosity classifications can contribute to the porous Li structures observed at high current densities. Concerning contributions from crystallographic porosity, the structural defects and surface roughness of the Cu wire can cause interfacial voids between the Cu substrate and the Li deposit. Regarding contributions from inclusion porosity, gas evolution at the electrode-electrolyte interface can act as non-conducting regions preventing lithium-ion transport. Gaseous species, including CO_2, CO, C_2H_4, and H_2 have been observed and reported as products of electrolyte decomposition[50 144 145, 146 146 147]. Repeated cycling has been reported to rupture unstable regions of the SEI, exposing the electrode to further electrolyte decomposition[148 36] that can generate gas[149 139]. Alternatively, the role of electrochemical oxidation of the underlying copper wire towards gas generation could be a contributing factor but has not been observed in this work.

Given our observations and the prior work discussed above, we conclude that the internal morphologies from high current density cycling are most likely due to gas evolution during electrodeposition that patterns the Li. This conclusion is based on similar voids being observed in the 10°C/CC experiment with extended deposition at a

moderate current density of 5 mA/cm^2, where no stripping was performed. At the lower current density of 2.4 mA/cm^2, it is possible that the gaseous byproducts of SEI formation do not become sufficiently concentrated for bubble nucleation or accumulation due to the minimal formation of additional SEI. Our additional ex-situ macro-scale experiments with degassed EC:DEC electrolyte showed notable gas evolution within the porous Li layers formed during extended electrodeposition of Li on Cu foil. On the other hand, no gas evolution was observed at the Li metal counter electrode during dissolution. Previous work has shown that the likely gasses to expect are ethylene and carbon monoxide[150-152]. Relevant reactions for the formation of these gasses include:

$$2(EC\text{-}Li^+) + 2e^- \rightarrow Li_2EDC^* + C_2H_4$$

$$EC + 2e^- \rightarrow OC_2H_4O^{2-} + CO$$

$$EC + 2Li^+ + 2e^- \rightarrow Li_2CO_3 + C_2H_4$$

$$Li_2CO_3 + 2Li \rightarrow 2Li_2O + CO$$

*Where EDC = Dilithium Ethylene Glycol Dicarbonate

It is apparent that temperature has an effect on the size of the voids formed by evolved gases. Comparison of samples after high current cycling at 5ºC and 33ºC revealed similar large void structures (>6 μm diameter). However, the 5°C sample contained many small voids (<3 μm diameter). Significant groupings of these small void structures appear close to the Cu. However, a small grouping of these small void structures are also found at the outer surface of the Li layer (farthest from Cu). These observations

can be rationalized by considering gas evolution and the temperature dependence of the electrolyte viscosity and surface tension. At low temperatures, the cyclic carbonate organic electrolytes exhibit a higher viscosity[153]. The increased viscosity may inhibit the rate of gas bubble coalescence and their departure from the electrode surface, since bubble coalescence is observed to be inversely related to liquid viscosity[154].

Another interesting result is the increasing voltage trend during dissolution at high current density, which has also been found in prior work [155, 156]. It reflects a loss of accessible Li that cannot be recovered, which increases the overpotential, causing the voltage limit to be reached and ending the dissolution step[157]. The asymmetric voltage profile (deposition vs. dissolution segments) exhibited from the high current density samples can signify capacity fade and could be indicative of localized dissolution processes leading to non-uniform morphologies. Figures 5.5e-h clearly show a large abundance of Li on the Cu wire electrode and therefore the increased voltage is not due to a complete dissolution of Li from the wire. Thus, mechanisms related to the sharp increase in voltage likely relate to the formation of dead Li through electronic isolation and increase the electronic component of the ohmic overpotential. From the nano-CT images, there is no apparent discontinuity within the interior of the Li metal that would result in electronic isolation. Based on the images showing many voids at the Cu|Li interface, the key mechanism for electronic isolation is reduction in contact area between the Li and Cu wire due to Li dissolution localized at the interface between the two metals. We submit that the alternative hypothesis of evolved gas blocking the surface and causing rapid voltage rise can be ruled out due to the consistent

instantaneous return to low overpotential electrodeposition following the high voltage transients. Our preferred hypothesis, which relies on electronic isolation of the Li at the interface, allows for electrodeposition to immediately resume though deposition of Li onto the copper current collector. This is consistent with the voltage response we saw and better explains the observed asymmetry.

These findings have relevant implications for batteries with either Li metal anodes or graphite anodes under charging conditions where electroplating is incited (cold, fast charging). The differences in the internal void morphology may significantly impact the effective mechanical properties of the cycled Li layers. For instance, tighter packing of smaller voids with low temperatures may yield a stiffer Li growth with a higher propensity to puncture or bypass the separator and short the cells, causing battery failure. Such implications should be investigated in future work. Additional areas of future work include investigating other electrolytes, additives, and charging conditions.

5.5 Conclusion

We show that the cycling current density and temperature has a significant impact on the morphology of lithium metal film deposits. In our experiment, we observe distinct morphologies ranging from uniform lithium plating at low current density to non-uniform, spherical voids of varying diameters at high current density. The high current density samples exhibit non-uniform morphology with large internal voids with diameters in excess of 8 μm. In addition, high current density cycling at a low temperature of 5°C exacerbates void formation. Although the large internal void structures existed at both

temperatures, the 5°C morphology exhibits additional smaller voids, less than 3 μm in diameter, with the highest concentration near the lithium-copper interface. Our approach employing nano-CT allows for sub-micrometer internal features to be resolved, while still being able to image the full thickness of the electrode. Our results indicate the significant impact that current density and temperature have on Li electrodeposition morphology and how secondary effects, such as gas generation, can affect void size and location. Furthermore, our analysis of cycling versus deposition has provided insight into possible electronic isolation mechanisms leading to capacity loss and potentially abusive high voltage transients during discharge (stripping). In turn, the observed morphologies may impact the stiffness and mechanical integrity of cycled Li electrodes to a greater or lesser degree, thus, altering the ability of localized Li electrodeposition and dendrites to cause catastrophic battery failure.

6. The Predictability of Unstable Lithium Deposition

6.1 Introduction

As explained in the introduction, widespread research has been conducted in (1) observation to better understand the mechanisms of dendrite growth[7, 50, 51, 56, 72, 158, 159] and (2) testing dendrite prevention strategies[18, 82, 85, 87-89, 92, 94, 96, 97, 160, 161] so that the lithium anode can ultimately be reinstated. Dendrites in traditional metals systems such as copper and zinc are distinguished by their arborescent characteristics[162, 163]. In the case of lithium, a broader range of morphologies may be relevant to understanding battery failure. Traditional dendritic growth is a well-known safety hazard[164], but any irregular lithium growth can have detrimental effects for the cell: an increased surface area of lithium will reduce cell capacity by breaking down the electrolyte to form more Solid Electrolyte Interphase (SEI)[6, 72], or result in 'dead lithium'[74, 75].

In order to guarantee dendrite growth can be detected, many observational studies use relatively higher currents in their experiments, where dendrites are more likely to occur, compared to more standard cell conditions. These current densities reach up to 50 mA/cm^2, as can be seen in Figure 6.1 – much higher than the typical currents used in experiments designed to test methods of preventing dendrites. In addition to the significance of current density, a propensity for dendritic growth has also been predicted[13] and shown[50],[134] to rely on temperature as well. (See also: Chapter 5)

Current Density of Dendrite Observation Papers (mA/cm²)	Ref	Current Density of Dendrite Prevention Papers (mA/cm²)	Ref
0.057	51	0.065	85
0.076	51	0.1	87
0.175	7	0.1	88
1	56	0.1	18
1	158	0.1	92
2.61	72	0.5	89
5	50	0.5	97
6.3	159	1	87
10	72	1	94
10	158	1	96
12.5	159	1	160
25	159	2	161
25	158	3	160
50	72	10	82

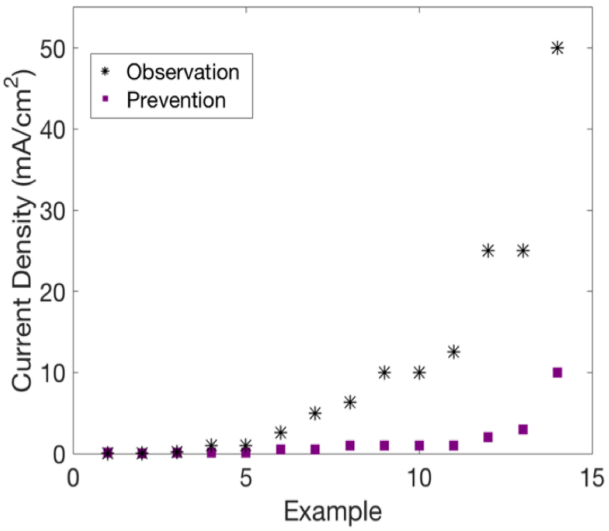

Figure 6.1. A comparison of current densities used in studies of dendrite observation and prevention.

Ideally, a technique would exist that could observe irregular lithium deposition and the effect of various prevention strategies, but these studies require modifications in cell assembly. Therefore, they cannot include the effects of typical cell conditions such as the polymer separator in a liquid electrolyte, the internal cell pressure, etc. As it stands, the fact that many studies use their own unique set of testing conditions makes it difficult to compare results, or use the findings of the observation studies to assist the development of a prevention method. From a practical perspective, a preventative technique is most directly concerned with impeding the formation of any irregular lithium morphology that will cause the cell to fail, regardless if it would be classically considered dendritic. The question is then, how likely is this irregular growth to occur at a particular set of conditions and to what extent does the prevention method under consideration alter this probability. In this chapter, I present a baseline of how likely irregular lithium

growth is to occur at a selection of temperatures and current densities. In Chapter 7, I use this baseline to distinguish between different potential dendrite prevention methods.

6.2 Experimental

6.2.1 Cell Assembly

The cells were assembled in an Argon glovebox using 2032 coin cell casings, with a hopper spring and 1 mm spacer. The electrolyte was 1 M LiPF6 in 1:1 EC:DMC from Sigma Aldrich. The separator was 25 μm Celgard, from MTI. Both electrodes were 0.6 mm thick Lithium chips, also from MTI. The counter electrode was 16 mm in diameter and the working electrode was 13 mm in diameter, in order to ensure complete electrode overlap. The cases were crimped in an MSK-110 hydraulic crimping machine to 750 psi.

6.2.2 Cell Testing

The cells were tested using the parameters outlined in Table 6.1, using a Biologic VMP3 potentiostat. Ten cells were tested under each condition, for a total of 80 cells. The surface of the working electrode was prepared by a low current deposition (0.1 mA/cm^2) for one minute. Then, the relevant current density for that particular test was applied and continuous lithium deposition occurred until a voltage response indicated that irregular growth had begun, or the cell shorted. In either case, the point at which the cell voltage begins to significantly deviate from its previous trajectory is denoted as ‘cell failure’, as shown in Figure 6.2.

Table 6.1. Cycling parameters of interest

Parameter	Setting
Current	0.1, 0.5, 1, 2.5 mA/cm^2
Temperature	0°C, Room Temperature (RT)

6.2.3 Cell Disassembly

A selection of cells from the boundary cases (the highest and lowest of temperature and current density) were opened to observe the deposition's effect on the lithium surface. Three cells were opened in each case, and representative photographs were taken for Figure 6.4. The coin cell case walls were cut into using a Dremmel 7700 tool in an Argon glovebox. The cell was then prised open and the electrodes removed. This process was likely a destructive one to the more delicate dendritic morphologies that could occur, and so the images shown in Figure 6.4 cannot represent the full picture of the electrode's state at the time the test was finished.

6.3 Results

Figure 6.2 shows the two main types of 'failure' referred to in this study. Figure 6.2a, a direct short, was observed primarily at the lower current of 0.1 mA/cm^2 and occasionally at 0.5 mA/cm^2. A more gradual voltage response towards shorting is shown in Figure 6.2b. This behavior was observed occasionally in the 0.5 mA/cm^2 cases, and was the primary response in the 1.0 and 2.5 mA/cm^2 cases. In this study, we were interested in

the extent that lithium deposition could occur stably before we observed signs of irregular growth and so we denoted the first instance of sudden voltage change as cell failure.

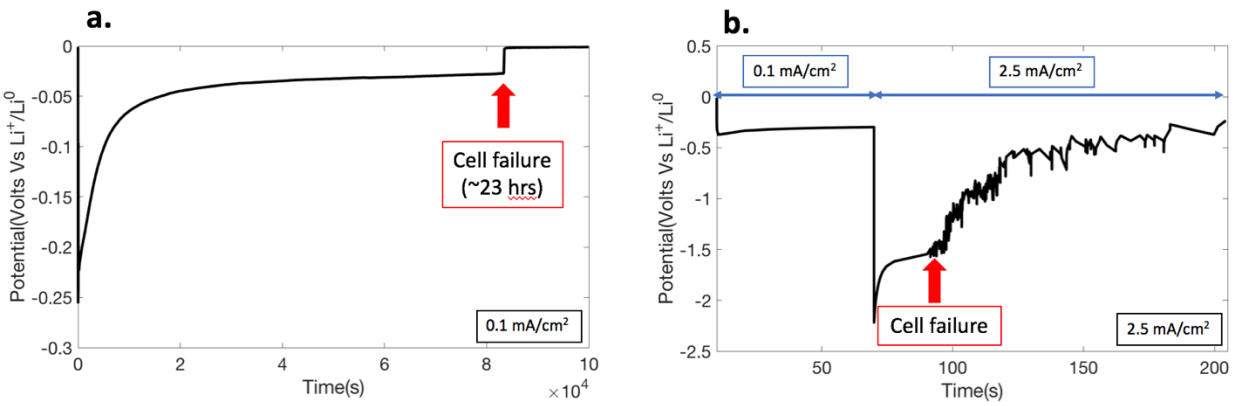

Figure 6.2. Voltage time series examples of the typical onset of irregular growth seen in these experiments. (a) A directly shorted cell, seen primarily in the 0.1 mA/cm^2 experiments and (b) a more gradual decrease in the overpotential, seen in the 1.0 and 2.5 mA/cm^2 experiments. The 0.5 mA/cm^2 experiments exhibited a mixture of each behavior.

Although ten cells were tested for each condition, at the lower temperature there were some examples which did not show failure within the expected time frame (ie continuous deposition with no indication of unstable deposition for up to an order of magnitude beyond the average deposition of failure). The extent to which this behavior was observed in each case is shown in Table 6.2. For the 0.1 mA/cm^2 cells, it was not possible to continue testing for an order of magnitude longer than the average, as there was not enough lithium in the cell. Instead, the deposition continued for over twice the average amount of time before stopping the test.

Table 6.2. Cells which did not exhibit signs of unstable deposition at 0°C

Current (mA/cm^2)	Cells with Continuous Stable Deposition
0.1	4/10
0.5	1/10
1.0	1/10
2.5	0/10

Using the deposition time until failure and the current density tested, we then calculated how much lithium was deposited stably before failure. This value was then averaged across the area of the electrode. Figure 6.3 shows the individual points of failure for each test and the average at each condition of how much lithium was deposited before failure in μg/cm^2 – not including those cells shown in Table 6.2 where failure did not occur. At the lower currents (0.1 and 0.5 mA/cm^2), stable deposition occurs for longer at RT than at 0°C, in line with the statement that potentially dangerous dendritic growth is more likely at lower temperatures. However, at the higher currents (1.0 and 2.5 mA/cm^2), stable deposition occurs for longer at 0°C than RT.

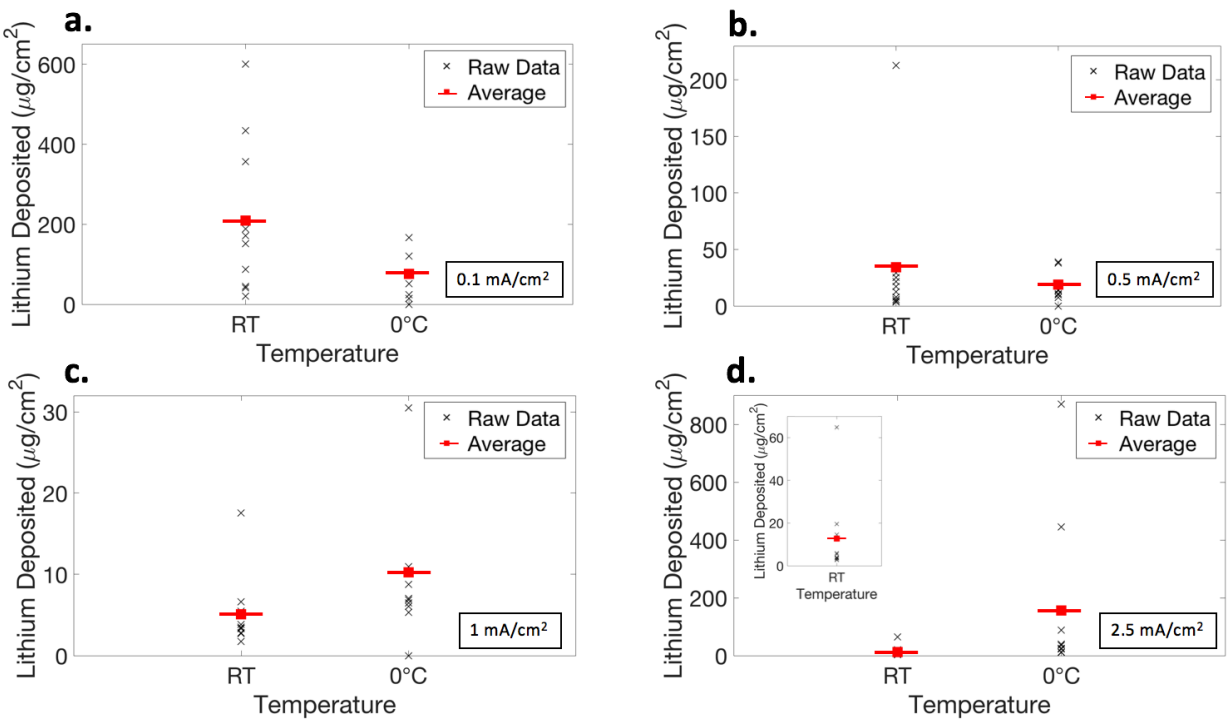

Figure 6.3. The amount of lithium deposited stably (in μg/cm^2) before failure for the (a) 0.1 (b) 0.5 (c) 1 and (d) 2.5 mA/cm^2 tests at RT and 0°C.

The stability of the deposition in each cell varied greatly, as can be observed in Figure 6.3. Table 6.3 quantifies this by showing the average amount of lithium deposited stably before failure for each condition and the standard deviation of that data.

Table 6.3. Extent of Continuous Stable Lithium Deposition Before Failure

Current Density (mA/cm^2)	RT (μg/cm^2)	0°C (μg/cm^2)
0.1	210 ± 193 (92%)	76 ± 57 (77%)
0.5	34 ± 63 (190%)	19 ± 12 (62%)
1.0	5.1 ± 4.6 (90%)	10 ± 7.8 (76%)
2.5	13 ± 19 (150%)	156 ± 284 (180%)

The cells were then opened in order to examine the electrode's surface for signs of what caused these failures. Figure 6.4 shows distinct signs of irregular growth on the surface of the 0.1 mA/cm^2 electrodes. There are no such signs on the 2.5 mA/cm^2 sample electrodes, but, as mentioned above, the process used to cut open the cells could have damaged any morphology that was particularly delicate.

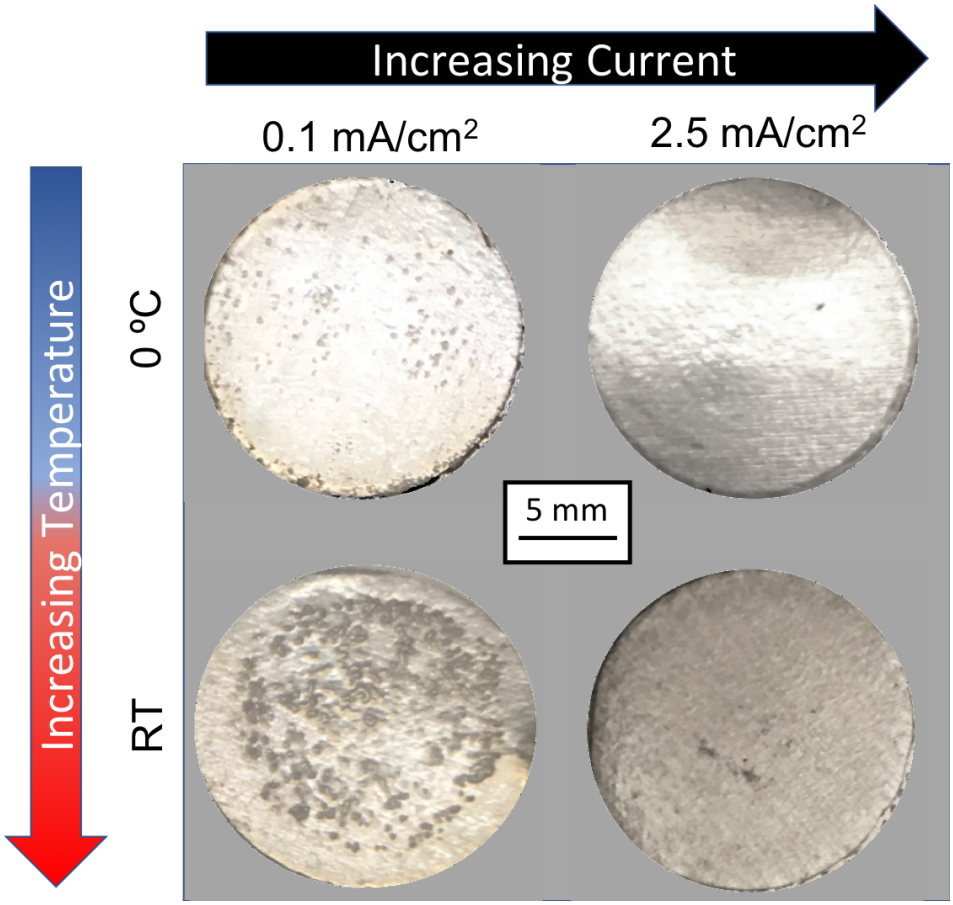

Figure 6.4. Photographs of the working lithium electrodes from the opened cells, representing the test conditions of 0.1 and 2.5 mA/cm^2 at RT and 0°C.

6.4 Discussion

A primary takeaway from this data is its variability, seen in Table 6.3, which exists even after fabricating tens of cells in the same controlled conditions in terms of electrolyte, separator, pressure, etc. There still remain variables which cannot easily be accounted for, such as the state of the lithium electrode's surface, which result in an imprecise metric of predicting the onset of irregular lithium growth. This emphasizes the importance of replicate tests when determining the effectiveness of a dendrite prevention method, particularly at the lower currents when stable lithium deposition may occasionally continue indefinitely. Furthermore, in order for a dendrite prevention method to be shown as significantly deviating from the baseline, the average amount of stable growth before failure would have to exceed at least twice that shown in the bare lithium case.

The voltage response at the onset of failure is indicative of the nature of the failure itself. The electrode examples given for the 0.1 mA/cm^2 samples in Figure 6.4 clearly show lithium growth on the surface that is not uniform, and yet there is no evidence of this build up in terms of a voltage response shown in Figure 6.2a until the sudden full short of the cell. Conversely, there is no visual sign of buildup on the surface of the 2.5 mA/cm^2 samples, but there is a significant voltage shift that begins to occur shortly after deposition. It has previously been noted by Wood et al[165], that dendritic nucleation results in a decreased overpotential for further dendritic growth when compared to bulk lithium. Such high surface area morphology could also prove fragile in the event of

outside forces being applied, and thus absent in our optical analysis of the electrode surface after opening the cell.

Temperature's effect on the extent of stable deposition before failure varies with current density. At the lower currents of 0.1 and 0.5 mA/cm^2, more lithium is deposited stably before failure on average at RT than at 0°C; whereas, at the higher currents of 1.0 and 2.5 mA/cm^2, the inverse case is true. Previous studies have considered the morphology changes and concluded that dendritic growth is more likely at sub-ambient temperatures[13, 70], but have not been able to directly observe the effect of external pressure on these morphologies. When the effect of pressure was looked at more closely, it was found that increased pressure lead to increased cell cyclability[48, 55, 70, 79]. Therefore, it may reasonably be concluded that although dendritic growth may be more likely at sub-ambient temperature, its morphology may be significantly altered by the combined effects of pressure and current density. The difference in the temperature stability ranges from Figure 6.3 could then be explained by the fact that certain morphologies could then prove more or less able to short the cell in the presence of a polymer separator.

6.5 Conclusions

A proposed method for creating a baseline of stable lithium deposition without signs of dendritic or irregular growth at different temperatures and current densities was outlined and collected, for the purposes of comparison to the performance of proposed lithium

dendrite prevention strategies. The voltage response observed during testing indicated that cell failure occurred by different mechanisms at different current densities of deposition – more clearly dendritic as the current density increased. Significant variation in the amount of stable lithium deposition that could occur before signs of irregular or dendritic growth were observed indicates that multiple trials of the same dendrite prevention method should be collected to compare with the baseline. In certain conditions, stable growth without failure continued for up to an order of magnitude beyond the average amount observed in the trials. The effect of temperature on the extent of stable deposition before signs of failure were observed is dependent on the current density at which the deposition is occurring: at 0.1 and 0.5 mA/cm^2, more stable deposition on average occurs at RT than at 0°C; whereas, at the higher currents of 1.0 and 2.5 mA/cm^2, the inverse case is true. Overall, our results indicate the difficulty in applying generalizations to the prediction of irregular lithium growth, and underline the importance of having a baseline for comparison that was constructed with the same or similar conditions to those one wants to test. As has previously been shown by observational studies, the morphology of lithium deposition varies widely in different deposition conditions. Though such studies found dendritic growth most likely to occur at high currents and low temperatures, we propose the introduction of cell pressure and the presence of a polymer separator in liquid electrolyte, which previous studies have not been able to directly observe, significantly affect the deposition morphology and the propensity for cell failure.

7. Using a Baseline to Predict Cell Performance

7.1 Introduction

As discussed in §2.3.1, polymer coatings on the lithium electrode have been used as an artificial, more stable SEI to prevent dendrite growth during cycling[108-111]. We investigated a new candidate polymer for its potential to improve cell performance: Poly(ethylene oxide lithium sulfonyl(trifluoromethylsulfonyl)imide) (PEO-TFSI-Li^+). This PEO based polymer was chosen due to PEO's increased stability at operating voltage conditions up to 4.5 V[166, 167] and high reported transference number[168]. Beyond the choice of polymer structure, one must further consider such variables as the effect of molecular weight and coating thickness on cell performance. Determining a cell's performance directly by long term cycling is time and resource intensive, particularly with a larger sample set. Trends in performance are not yet known or can't be relied upon. Traditional instrumentation methods to characterize the film (ie SEM, AFM, etc) either have to be specially modified to prevent atmospheric exposure or limited by the fact that there is a high likelihood of altering the lithium surface before the characterization begins.

A more efficient means of distinguishing polymer films that show potential as good artificial SEIs could streamline this process. Previous work has established that any irregular growth can ultimately lead to cell failure, either through shorting or capacity fade. In Chapter 6, a baseline was established to determine the extent of stable

deposition in a symmetrical bare lithium cell before the onset of irregular or dendritic growth at particular temperatures and current densities. Here, I show that the performance of a cell during a single deposition – specifically, how it compares to a baseline in terms of deposition stability – can predict its long term cyclability

7.2 Experimental

7.2.1 Polymer Coating

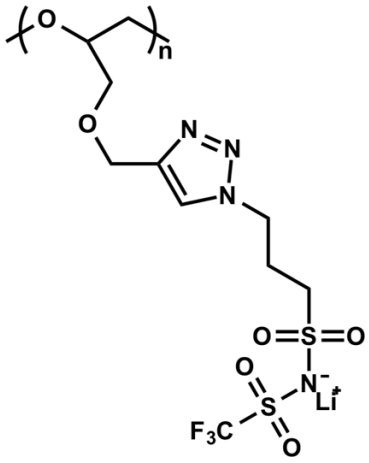

Figure 7.1 Structure of PEO-TFSI-Li^+.

PEO-TFSI-Li^+ (the structure of which is shown in Figure 7.1) was synthesized by our collaborators in the Matyjaszewskia lab, specifically Jacob Flum and Sipei Li. Polymers with several different molecular weights were tested, as shown in Table 7.1. For brevity and clarity, all coated polymer samples will be referred to by their molecular weights. A lithium chip coated with the sample 1 polymer is the 11k sample, etc.

Table 7.1 Molecular Weights of PEO-TFSI-Li^+ samples

Sample	1	2	3	4	5	6
Molecular Weight (g/mol)	11,000	23,000	37,000	52,000	74,000	129,000

It was then dissolved into a 2% by weight solution of dimethyl sulfoxide (DMSO) and transferred into an argon glovebox. There it was drop cast onto 16 mm diameter lithium chips from MTI in volumes of 0.075 mL and 0.175 mL. These will be referred to as the thinner and thicker films, respectively. Deposition volumes were chosen to fully cover the surface of the lithium chips. The films dried at 50 °C overnight.

7.2.2 Cell Assembly and Testing

The coated Li electrodes were assembled into 2032 coin cells in an Argon glovebox, using a hopper spring and 1 mm spacer. The separator was 25 μm Celgard, from MTI. The cases were crimped in an MSK-110 hydraulic crimping machine to 750 psi. Symmetrical cycling was performed at a current density of ±1.0 mA/cm^2, with each plating/stripping segment lasting 30 minutes. Continual deposition tests were run, as in Chapter 6, with one minute at 0.1 mA/cm^2 and then continued at 1.0 mA/cm^2 until signs of irregular lithium growth were observed – referred to here as failure. All electrochemical tests were performed at room temperature.

7.3 Results

7.3.1 Direct Determination of Sample Performance

The dried films showed significant variation in terms of surface homogeneity, as can be seen in Figure 7.2. Some show a marked inclination to agglomerate at certain sections

on the lithium chip (Samples 1 and 4), while other are relatively homogeneous but more concentrated at the edges of the chip (3 and 6). Images shown are of the thinner film samples, but the thicker film samples of the same molecular weight showed the same drying patterns.

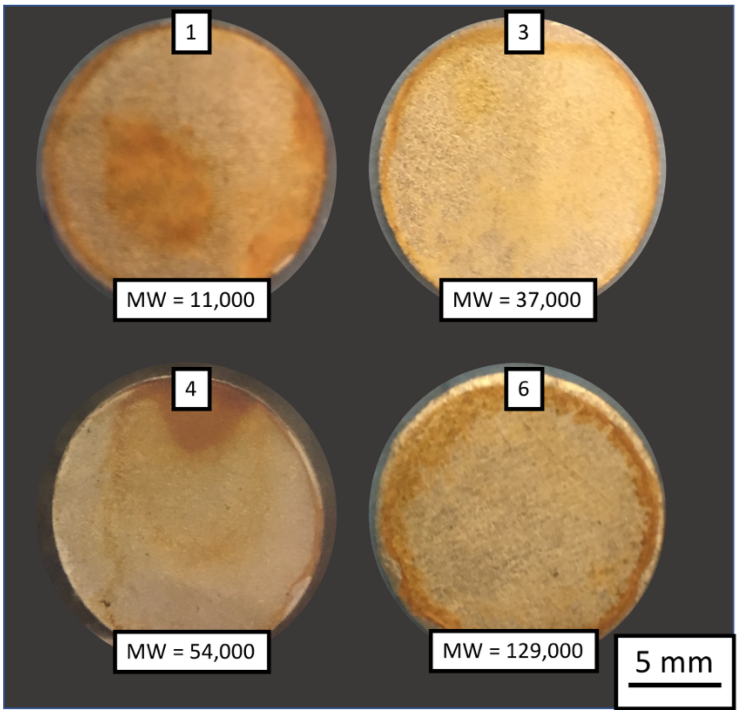

Figure 7.2. Photographs of dried thinner film (0.075 mL volume deposited) samples on lithium chips, from solutions of polymer samples with molecular weights of [1] 11k, [3] 37k, [4] 54k and [6] 129k g/mol.

Figure 7.3 shows the cycling performance of the two relatively homogeneous films compared to the performance of a bare symmetrical lithium cell. The bare lithium data shows clear signs of irregular growth within the first few cycles (Figure 7.3a or c) – indicated in the spikes of voltage response to the plating/stripping current – and later (Figure 7.3b or d) appears to be at least partially or soft shorted, acting as a quasi-

resistor. Comparing the performance of the coated samples in Figure 7.3a or c, the 129k sample in 7.3c shows initial stable cycling, while the 37k sample in 7.3a shows signs of unstable deposition from the beginning. By the later cycles, shown in 7.3b and 7.3d, both coated samples have failed and show quasi-resistive behavior. Cells made from the coatings that dried into inhomogeneous films (ie 54k shown in Figure 7.1) failed within the first few cycles. Cells were also made to determine the effect of coating thickness for the higher molecular weight samples. Preliminary results showed the thinner film had more stable cycling behavior. Further testing focused on investigating thinner film performance for the different molecular weight samples.

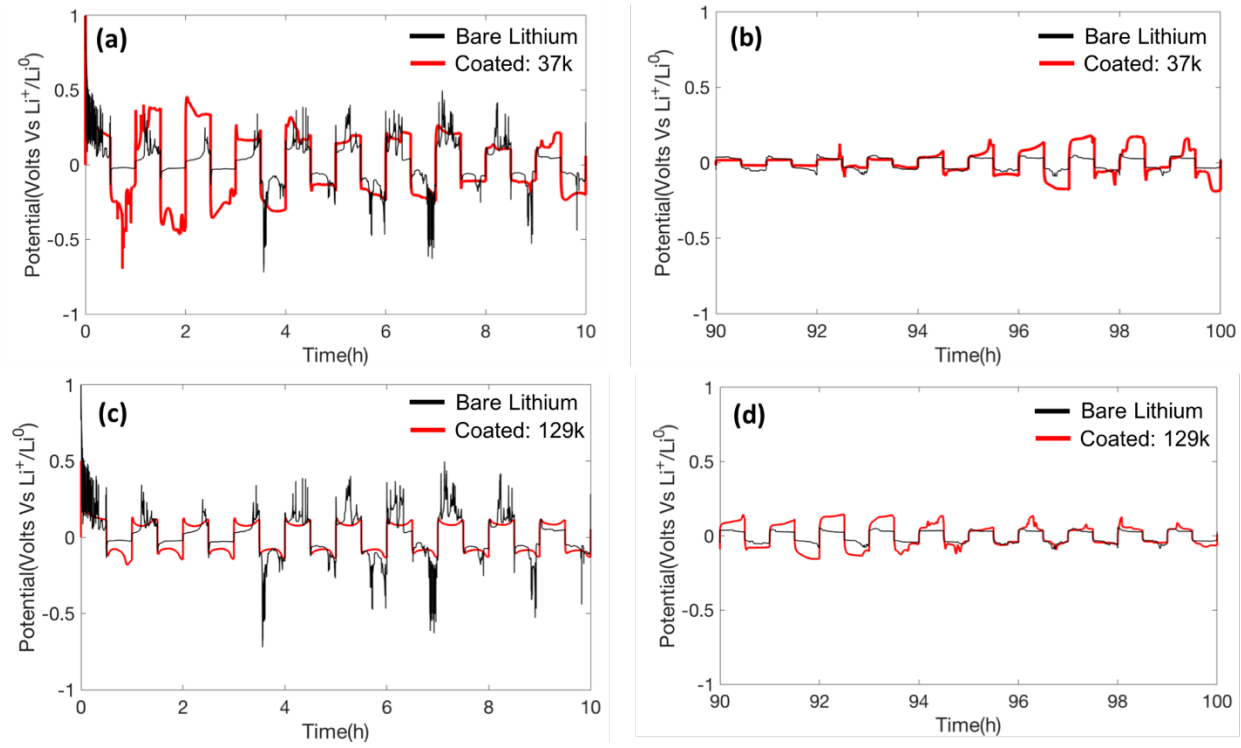

Figure 7.3. Cycling performance of two optically homogeneous coatings on lithium compared to that of bare lithium. All tests conducted at 1.0 mA/cm^2. (a) Cycles 1-10 and (b) cycles 90-100 of the 37k sample. (c) Cycles 1-10 and (d) cycles 90-100 of the 129k sample.

7.3.2 Indirect Prediction of Sample Performance

We will now consider the indirect method of determining sample cycling performance: the extent of stable lithium growth in a continuous deposition before failure. Two sample coatings are considered at either end of the molecular weight spectrum (11k and 74k) to see if the proposed deposition to failure test can (1) distinguish between them and (2) relate to their cycling performance. Figure 7.4 shows examples of the deposition to failure test results for the two samples. As in Chapter 6, the first evidence of irregular lithium deposition is denoted as cell failure. The test clearly distinguishes between them: the 11k sample fails at 0.02 hours and the 74k sample fails at 0.2 hours.

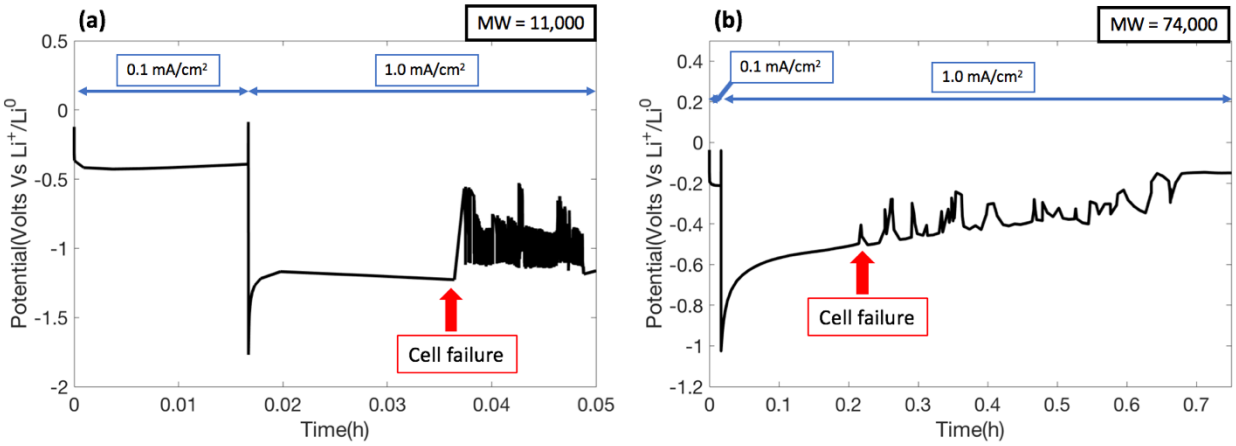

Figure 7.4. Voltage time series examples of the typical onset of irregular growth seen in these experiments at 1.0 mA/cm^2 for the (a) 11k and (b) 74k samples.

Duplicate deposition to failure tests were conducted for each sample, to ensure the behavior seen in Figure 7.4 was repeatable. The amount of lithium deposited before failure was then calculated for each cell and averaged over the total area of the

electrode. Figure 7.5 shows the stable deposition values for the two coated cases (11k and 74k) and the bare lithium case (see §6.3). The 11k sample is not distinguishable from the bare lithium, whereas the 74k sample clearly has an increased amount of stable lithium deposited before failure. The average amount of lithium deposition before failure for each sample was 5 μg/cm^2 (bare), 6 μg/cm^2 (11k) and 43 μg/cm^2 (74k).

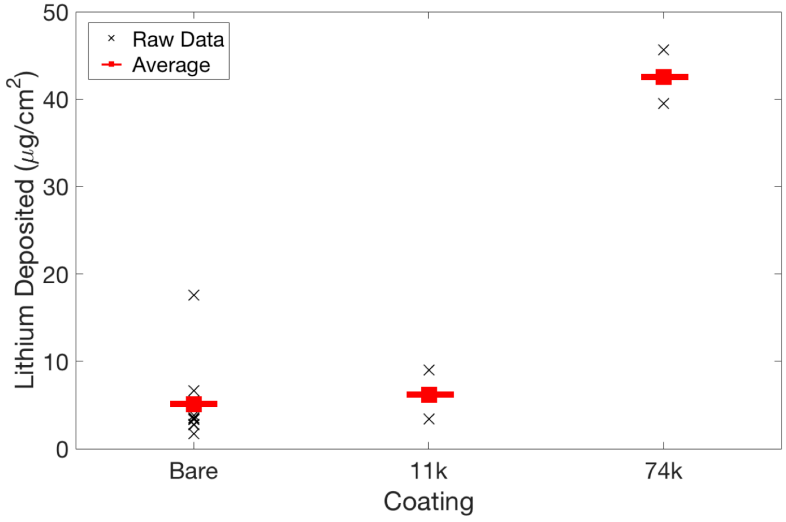

Figure 7.5. Stable lithium deposited before failure (in μg/cm^2) at 1.0 mA/cm^2 for the bare, 11k and 74k samples

Figure 7.6 shows the cycling performance of these coated samples compared to bare lithium. In 7.6a, one can see that the 11k sample shows unstable cycling with high overpotential from the beginning of cycling. In contrast, the 74k has stable cycling with a steady low overpotential value of ~120 mV for the first hundred cycles. Ultimately, this cell was cycled for 400 more cycles with no major signs of irregular deposition – though the overpotential did slowly increase to 250 mV.

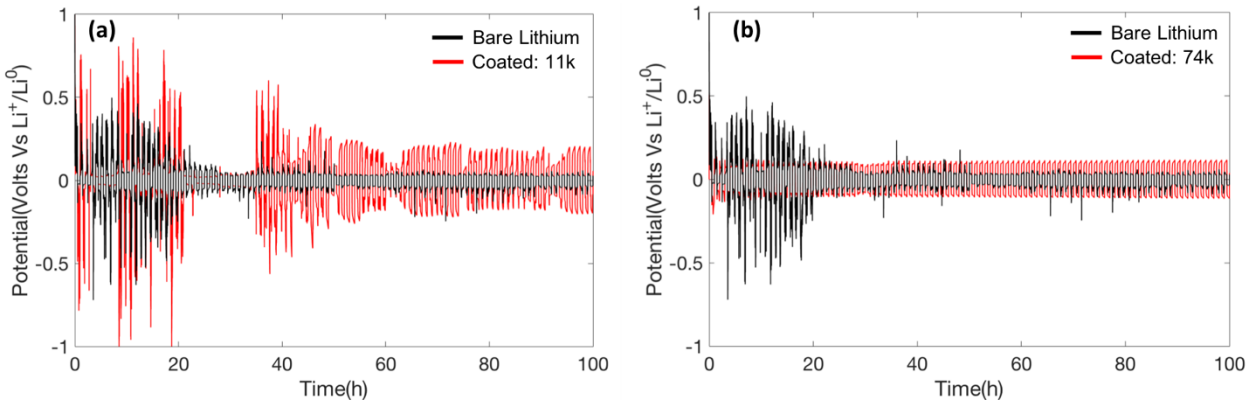

Figure 7.6 Cycling performance of the first 100 cycles of (a) 11k and (b) 74k samples compared to bare lithium at 1.0 mA/cm^2.

7.4 Discussion

Ideally, an artificial SEI will work to prevent dendritic or irregular growth by homogenizing current density across the surface of the electrode. It is reasonable to expect, then, that a polymer film acting as an artificial SEI will be most effective when the film itself creates a complete homogeneous coating of the electrode. In Figure 7.2, it was shown that there was not a linear connection between the molecular weight of the polymer and its dried coating homogeneity. Cell testing showed that inhomogeneous coatings failed quickly, but homogeneity did not directly link to improved cell performance compared to a bare lithium cell. Figure 7.3a shows the relatively homogeneous coating of the 37k sample indicated irregular lithium deposition within the first ten cycles. The 129k sample also had a relatively homogeneous dried film. Although it had more stable cycling behavior than bare lithium in the first ten cycles (Figure 7.3c), its performance significantly degraded as cycling continued and by 100 cycles it is no improvement from the 37k sample (Figure 7.3d and Figure 7.3b). A thicker film of 129k performed worse than a thinner film, likely due to the increased

impedance across the film's thickness. From these results, we can conclude that the homogeneity of the samples is not sufficient to predict their performance.

The deposition to failure test performed here is an accessible screening technique to distinguish between potential films, as it involves only the materials and instruments required to electrochemically test cells in the first place. Additionally, Figure 7.4 indicates that this technique can distinguish between samples in the time scale of tens of minutes as opposed to tens of hours. These data corresponded to an eight-fold increase in stable lithium deposition for the 74k sample when compared with bare lithium or the 11k sample, shown in Figure 7.5. To prove this test's viability as a potential screening technique, the cells were then cycled to compare their long-term performance in Figure 7.6. The 74k sample shows drastically improved cycling stability compared to the bare lithium and 11k samples, in line with its improvement in terms of continuous lithium deposition stability. While this is not enough to prove a direct correlation between these two phenomena, there is theoretical grounding beyond this data to believe they are linked. A well-functioning artificial SEI should lead to stable current distribution throughout any plating and stripping processes during cycling, and so an extended plating process is designed to test the limits of that increased stability. This test has further potential applications to other dendrite prevention methods, when provided with an appropriate baseline.

7.5. Conclusion

A new method to distinguish between polymer coatings on lithium electrodes for their potential as artificial SEIs to prevent dendritic or irregular lithium deposition was introduced. Initial tests to distinguish samples by the homogeneity of their films failed, as did attempts to find a direct relationship between polymer molecular weight and cycling performance. However, an increase in the extent of stable continuous lithium deposition was seen in parallel to increased cycling performance. We believe there is a direct relation between these data, as the deposition to failure test is an intensified version of a cell testing regime. This test has the advantages of being both quick and accessible to any lab already conducting electrochemical tests. While it cannot take the place of cell cycling, it has the potential to be a useful tool to screen for which samples are most promising to push into long term cycling tests. Furthermore, it could easily be used more broadly when developing other dendrite prevention techniques.

8. Conclusions

This work investigated how failure occurs at lithium battery interfaces in order to better understand how to design failure prevention methods. Using nano-CT, we were able to non-destructively examine the internal morphology of anode materials to reveal how subsurface features influenced cell performance and failure. The inherent variability present within even a modest sample size led this work to shift focus into how to better test and report on failure prevention methods, specifically for dendritic type failure.

The first two hypotheses of this work are addressed in Chapter 4, where the nano-CT was used to examine the extent of SEI growth within internal pores of a cycled graphite electrode. Hypothesis one stated that any growth of the SEI would increase the absorption signal of the sample by introducing higher Z elements into the structure and this could be used to track the SEI's effect on the internal pores of the electrode. This is supported by the data: a distinct increase in absorption signal was noticed after cycling, which can be concluded to have come from SEI growth. This was ultimately most compelling when it was combined with the data showing pore volume shrinkage after cycling in the phase contrast data. Concluding that significant SEI growth occurred at internal pores in the sample disproved the second hypothesis, which stated that the SEI had such a strong preference to form on the surface that the internal pores were unaffected.

In Chapter 5, we expand upon the capabilities of the nano-CT and explore Hypotheses 3 and 4. Previous studies of lithium by micro-CT indicated there might be some relevant

subsurface phenomena occurring during dendrite growth. Here we prove that the nano-CT has the capability of resolving such subsurface features using the phase contrast mode, confirming the third hypothesis. The fourth hypothesis stated that these subsurface features are relevant to dendrite growth, which is partially supported by this data. The formation of gas bubbles under the surface of the electrode would disrupt electronic contact and create hot spots of high local current density. However, actual in-operando imaging would be required to observe the direct link between these voids and dendritic behavior. Development of an appropriate cell for such imaging has continued after the work in chapter 5 was completed.

Specialized imaging techniques provide compelling evidence in the development of a fuller understanding of lithium battery failure, but they are also only available to a limited subsection of the battery research community. Examining the breadth of research that has been conducted on lithium dendrite observation and prevention alone, we noted the lack of a unifying series of testing parameters that would allow for data to be compared. In Chapter 6, we decided to test the feasibility of creating a baseline of lithium deposition performance to determine the likelihood of failure at a particular set of testing parameters in symmetrical cell conditions. The prediction being tested here was that a predilection towards irregular or dendritic lithium growth would ultimately be determined by a host of factors that could not be completely controlled for and so the baseline values would be more correctly reported as a range rather than as single data points. This was confirmed by the data collected, where the lowest standard deviation in a data set was 62%.

The baseline was created with hypothesis five in mind, which is that the extent of continuous stable lithium deposition before dendritic growth in a cell is a metric that can be used to determine long term cell performance. In Chapter 7, this hypothesis was tested directly and partially confirmed. A particular set of polymers were tested for their potential as artificial SEI to prevent dendritic failure in cells. No trend in polymer properties was observed that could easily be used to predict performance. Instead, the results of the deposition to failure test (established in Chapter 6) were collected for different polymer samples to determine if and how they deviate from the baseline. The sample which showed an increased extent of stable continuous deposition also showed an increase in stable cell cycling performance. The sample which had a congruent extent of stable deposition to the baseline had sporadic cell behavior that failed quickly. While this is not enough to conclusively correlate the two behaviors, it is a promising preliminary confirmation.

Future work on the creation of a baseline test should expand this data set with other potential dendrite prevention methods to create a more concrete connection between deposition to failure and cell cycling results. Should these tests prove out the connection we believe to be there, more work would have to be done on refining the creation of a workable baseline in different conditions than those already tested. Wider statistical trials would be required to determine the number of cells needed for each set of conditions to accurately represent the range of potential behaviors. At a broader perspective, as the battery community continues to investigate these phenomena,

attempts to reach a consensus on standardized language to discuss irregular or dendritic lithium growth will hopefully coalesce into an agreed upon set of terms.

References

1. Bruce, P. G.; Freunberger, S. A.; Hardwick, L. J.; Tarascon, J. M., Li-O-2 and Li-S batteries with high energy storage. *Nat Mater* **2012,** *11* (1), 19-29.
2. O'Hayre, R.; Cha, S.-W.; Colella, W.; Prinz, F., *Fuel Cell Fundamentals*. 2nd ed.; John Wiley & Sons: New york, 2009.
3. Peled, E.; Golodnitsky, D.; Ardel, G., Advanced model for solid electrolyte interphase electrodes in liquid and polymer electrolytes. *J Electrochem Soc* **1997,** *144* (8), L208-L210.
4. Argonne-National-Laboratory; Center for Electrical Energy Storage: Tailored Interfaces Energy Frontier Research Center http://www.cse.anl.gov/%5C/cees/index.html.
5. Akolkar, R., Mathematical model of the dendritic growth during lithium electrodeposition. *J Power Sources* **2013,** *232*, 23-28.
6. Cohen, Y. S.; Cohen, Y.; Aurbach, D., Micromorphological studies of lithium electrodes in alkyl carbonate solutions using in situ atomic force microscopy. *J Phys Chem B* **2000,** *104* (51), 12282-12291.
7. Harry, K. J.; Hallinan, D. T.; Parkinson, D. Y.; MacDowell, A. A.; Balsara, N. P., Detection of subsurface structures underneath dendrites formed on cycled lithium metal electrodes. *Nat Mater* **2014,** *13* (1), 69-73.
8. Tkachuk, A.; Duewer, F.; Cui, H. T.; Feser, M.; Wang, S.; Yun, W. B., X-ray computed tomography in Zernike phase contrast mode at 8 keV with 50-nm resolution using Cu rotating anode X-ray source. *Z Kristallogr* **2007,** *222* (11), 650-655.
9. Nano-CT: Xradia UltraXRM-L200 http://www.cmu.edu/me/xctf/facility/index.html.
10. Linden, D.; Reddy, T. B., *Handbook of Batteries*. 4 ed.; McGraw-Hill: New York, 2011.
11. Balakrishnan, P. G.; Ramesh, R.; Kumar, T. P., Safety mechanisms in lithium-ion batteries. *J Power Sources* **2006,** *155* (2), 401-414.
12. Yoshio, M. B., Ralph J., Kozawa, Akiya, *Lithium-Ion Batteries: Science and Technology*. Springer Science & Business Media: 2010.
13. Akolkar, R., Modeling dendrite growth during lithium electrodeposition at sub-ambient temperature. *J Power Sources* **2014,** *246*, 84-89.
14. Balbuena, P. B. W., Yixuan, *Lithium-Ion Batteries: Solid-Electrolyte Interphase*. Imperial College Press: London, 2004.
15. Broussely, M.; Biensan, P.; Bonhomme, F.; Blanchard, P.; Herreyre, S.; Nechev, K.; Staniewicz, R. J., Main aging mechanisms in Li ion batteries. *J Power Sources* **2005,** *146* (1-2), 90-96.
16. Agubra, V.; Fergus, J., Lithium Ion Battery Anode Aging Mechanisms. *Materials* **2013,** *6* (4), 1310-1325.
17. Marchioni, F.; Star, K.; Menke, E.; Buffeteau, T.; Servant, L.; Dunn, B.; Wudl, F., Protection of lithium metal surfaces using chlorosilanes. *Langmuir* **2007,** *23* (23), 11597-11602.
18. Ding, F.; Xu, W.; Graff, G. L.; Zhang, J.; Sushko, M. L.; Chen, X. L.; Shao, Y. Y.; Engelhard, M. H.; Nie, Z. M.; Xiao, J.; Liu, X. J.; Sushko, P. V.; Liu, J.; Zhang, J. G., Dendrite-Free Lithium Deposition via Self-Healing Electrostatic Shield Mechanism. *J Am Chem Soc* **2013,** *135* (11), 4450-4456.

19. Chen, K.-H.; Wood, K. N.; Kazyak, E.; LePage, W. S.; Davis, A. L.; Sanchez, A. J.; Dasgupta, N. P., Dead lithium: mass transport effects on voltage, capacity, and failure of lithium metal anodes. *J Mater Chem A* **2017**.
20. M. Wakihara, O. Y., *Lithium Ion Batteries: Fundamentals and Performance*. Kodansha Ltd.: Tokyo, 2007.
21. Nykvist, B.; Nilsson, M., Rapidly falling costs of battery packs for electric vehicles. *Nat Clim Change* **2015,** *5* (4), 329-332.
22. Ciez, R. E.; Whitacre, J. F., Comparison between cylindrical and prismatic lithium-ion cell costs using a process based cost model. *J Power Sources* **2017,** *340*, 273-281.
23. Wood, D. L.; Li, J. L.; Daniel, C., Prospects for reducing the processing cost of lithium ion batteries. *J Power Sources* **2015,** *275*, 234-242.
24. Sakti, A.; Michalek, J. J.; Fuchs, E. R. H.; Whitacre, J. F., A techno-economic analysis and optimization of Li-ion batteries for light-duty passenger vehicle electrification. *J Power Sources* **2015,** *273*, 966-980.
25. Zheng, H. H.; Li, J.; Song, X. Y.; Liu, G.; Battaglia, V. S., A comprehensive understanding of electrode thickness effects on the electrochemical performances of Li-ion battery cathodes. *Electrochimica Acta* **2012,** *71*, 258-265.
26. Girishkumar, G.; McCloskey, B.; Luntz, A. C.; Swanson, S.; Wilcke, W., Lithium - Air Battery: Promise and Challenges. *J Phys Chem Lett* **2010,** *1* (14), 2193-2203.
27. Xu, W.; Wang, J. L.; Ding, F.; Chen, X. L.; Nasybutin, E.; Zhang, Y. H.; Zhang, J. G., Lithium metal anodes for rechargeable batteries. *Energ Environ Sci* **2014,** *7* (2), 513-537.
28. Manthiram, A.; Fu, Y. Z.; Su, Y. S., Challenges and Prospects of Lithium-Sulfur Batteries. *Accounts Chem Res* **2013,** *46* (5), 1125-1134.
29. FY 2013 Progress Report for Advanced Combustion Engine Research and Development. Energy, D. o., Ed. Washington DC, 2013.
30. Huggins, R. A., *Advanced Batteries*. Springer Science+Business Media: New York, 2009.
31. Valøen, L. O.; Shoesmith, M. I., The effect of PHEV and HEV duty cycles on battery and battery pack performance. In *PHEV 2007 Conference*, 2007.
32. Blomgren, G. E., The Development and Future of Lithium Ion Batteries. *J Electrochem Soc* **2017,** *164* (1), A5019-A5025.
33. CRC handbook of chemistry and physics. Chapman and Hall/CRCnetBASE: Boca Raton, FL, 1999; pp CD-ROMs.
34. Nylander, T.; Kekicheff, P.; Ninham, B. W., The Effect of Solution Behavior of Insulin on Interactions between Adsorbed Layers of Insulin. *J Colloid Interf Sci* **1994,** *164* (1), 136-150.
35. Brissot, C.; Rosso, M.; Chazalviel, J. N.; Lascaud, S., Dendritic growth mechanisms in lithium/polymer cells. *J Power Sources* **1999,** *81*, 925-929.
36. Vetter, J.; Novak, P.; Wagner, M. R.; Veit, C.; Moller, K. C.; Besenhard, J. O.; Winter, M.; Wohlfahrt-Mehrens, M.; Vogler, C.; Hammouche, A., Ageing mechanisms in lithium-ion batteries. *J Power Sources* **2005,** *147* (1-2), 269-281.
37. Abarbanel, D. W.; Nelson, K. J.; Dahn, J. R., Exploring Impedance Growth in High Voltage NMC/Graphite Li-Ion Cells Using a Transmission Line Model. *J Electrochem Soc* **2016,** *163* (3), A522-A529.

38. Aurbach, D.; Markovsky, B.; Salitra, G.; Markevich, E.; Talyossef, Y.; Koltypin, M.; Nazar, L.; Ellis, B.; Kovacheva, D., Review on electrode-electrolyte solution interactions, related to cathode materials for Li-ion batteries. *J Power Sources* **2007,** *165* (2), 491-499.
39. Xiong, D. J.; Petibon, R.; Nie, M.; Ma, L.; Xia, J.; Dahn, J. R., Interactions between Positive and Negative Electrodes in Li-Ion Cells Operated at High Temperature and High Voltage. *J Electrochem Soc* **2016,** *163* (3), A546-A551.
40. Burns, J. C.; Kassam, A.; Sinha, N. N.; Downie, L. E.; Solnickova, L.; Way, B. M.; Dahn, J. R., Predicting and Extending the Lifetime of Li-Ion Batteries. *J Electrochem Soc* **2013,** *160* (9), A1451-A1456.
41. Li, S. R.; Chen, C. H.; Xia, X.; Dahn, J. R., The Impact of Electrolyte Oxidation Products in LiNi0.5Mn1.5O4/Li4Ti5O12 Cells. *J Electrochem Soc* **2013,** *160* (9), A1524-A1528.
42. Dedryvere, R.; Foix, D.; Franger, S.; Patoux, S.; Daniel, L.; Gonbeau, D., Electrode/Electrolyte Interface Reactivity in High-Voltage Spinel LiMn1.6Ni0.4O4/Li4Ti5O12 Lithium-Ion Battery. *J Phys Chem C* **2010,** *114* (24), 10999-11008.
43. M. R. Palacín, A. d. G., Why do batteries fail? *Science* **2016,** *351* (6273).
44. Hendricks, C.; Williard, N.; Mathew, S.; Pecht, M., A failure modes, mechanisms, and effects analysis (FMMEA) of lithium-ion batteries. *J Power Sources* **2015,** *297*, 113-120.
45. Pinson, M. B.; Bazant, M. Z., Theory of SEI Formation in Rechargeable Batteries: Capacity Fade, Accelerated Aging and Lifetime Prediction. *J Electrochem Soc* **2013,** *160* (2), A243-A250.
46. Chattopadhyay, S.; Lipson, A. L.; Karmel, H. J.; Emery, J. D.; Fister, T. T.; Fenter, P. A.; Hersam, M. C.; Bedzyk, M. J., In Situ X-ray Study of the Solid Electrolyte Interphase (SEI) Formation on Graphene as a Model Li-ion Battery Anode. *Chem Mater* **2012,** *24* (15), 3038-3043.
47. Wranglén, G., Dendrites and growth layers in the electrocrystallization of metals. *Electrochimica Acta* **1960,** *2* (1), 130-143.
48. Cheng, X. B.; Zhang, R.; Zhao, C. Z.; Zhang, Q., Toward Safe Lithium Metal Anode in Rechargeable Batteries: A Review. *Chem Rev* **2017,** *117* (15), 10403-10473.
49. Rosso, M.; Brissot, C.; Teyssot, A.; Dolle, M.; Sannier, L.; Tarascon, J. M.; Bouchetc, R.; Lascaud, S., Dendrite short-circuit and fuse effect on Li/polymer/Li cells. *Electrochimica Acta* **2006,** *51* (25), 5334-5340.
50. Love, C. T.; Baturina, O. A.; Swider-Lyons, K. E., Observation of Lithium Dendrites at Ambient Temperature and Below. *Ecs Electrochem Lett* **2015,** *4* (2), A24-A27.
51. Hernandez-Maya, R.; Rosas, O.; Saunders, J.; Castaneda, H., Dynamic Characterization of Dendrite Deposition and Growth in Li-Surface by Electrochemical Impedance Spectroscopy. *J Electrochem Soc* **2015,** *162* (4), A687-A696.
52. Laman, F. C.; Brandt, K., Effect of Discharge Current on Cycle Life of a Rechargeable Lithium Battery. *J Power Sources* **1988,** *24* (3), 195-206.
53. Crowther, O.; West, A. C., Effect of electrolyte composition on lithium dendrite growth. *J Electrochem Soc* **2008,** *155* (11), A806-A811.
54. Wood, K. N.; Noked, M.; Dasgupta, N. P., Lithium Metal Anodes: Toward an Improved Understanding of Coupled Morphological, Electrochemical, and Mechanical Behavior. *Acs Energy Lett* **2017,** *2* (3), 664-672.
55. Li, S.; Jiang, M. W.; Xie, Y.; Xu, H.; Jia, J. Y.; Li, J., Developing High-Performance Lithium Metal Anode in Liquid Electrolytes: Challenges and Progress. *Adv Mater* **2018,** *30* (17).

56. Howlett, P. C.; MacFarlane, D. R.; Hollenkamp, A. F., A sealed optical cell for the study of lithium-electrode electrolyte interfaces. *J Power Sources* **2003,** *114* (2), 277-284.
57. Dolle, M.; Sannier, L.; Beaudoin, B.; Trentin, M.; Tarascon, J. M., Live scanning electron microscope observations of dendritic growth in lithium/polymer cells. *Electrochem Solid St* **2002,** *5* (12), A286-A289.
58. Yamaki, J.; Tobishima, S.; Hayashi, K.; Saito, K.; Nemoto, Y.; Arakawa, M., A consideration of the morphology of electrochemically deposited lithium in an organic electrolyte. *J Power Sources* **1998,** *74* (2), 219-227.
59. Stark, J. K.; Ding, Y.; Kohl, P. A., Nucleation of Electrodeposited Lithium Metal: Dendritic Growth and the Effect of Co-Deposited Sodium. *J Electrochem Soc* **2013,** *160* (9), D337-D342.
60. Mehdi, B. L.; Qian, J.; Nasybulin, E.; Park, C.; Welch, D. A.; Faller, R.; Mehta, H.; Henderson, W. A.; Xu, W.; Wang, C. M.; Evans, J. E.; Liu, J.; Zhang, J. G.; Mueller, K. T.; Browning, N. D., Observation and Quantification of Nanoscale Processes in Lithium Batteries by Operando Electrochemical (S)TEM. *Nano Lett* **2015,** *15* (3), 2168-2173.
61. Ge, M.; Lu, Y.; Ercius, P.; Rong, J.; Fang, X.; Mecklenburg, M.; Zhou, C., Large-Scale Fabrication, 3D Tomography, and Lithium-Ion Battery Application of Porous Silicon. *Nano Letters* **2014,** *14* (1), 261-268.
62. Phaneuf, M. W., Applications of focused ion beam microscopy to materials science specimens. *Micron* **1999,** *30* (3), 277-288.
63. Song, B.; Sui, T.; Ying, S.; Li, L.; Lu, L.; Korsunsky, A. M., Nano-structural changes in Li-ion battery cathodes during cycling revealed by FIB-SEM serial sectioning tomography. *Journal of Materials Chemistry A* **2015,** *3* (35), 18171-18179.
64. Chandrashekar, S.; Trease, N. M.; Chang, H. J.; Du, L.-S.; Grey, C. P.; Jerschow, A., 7Li MRI of Li batteries reveals location of microstructural lithium. *Nat Mater* **2012,** *11* (4), 311-315.
65. Key, B.; Bhattacharyya, R.; Morcrette, M.; Seznéc, V.; Tarascon, J.-M.; Grey, C. P., Real-Time NMR Investigations of Structural Changes in Silicon Electrodes for Lithium-Ion Batteries. *Journal of the American Chemical Society* **2009,** *131* (26), 9239-9249.
66. Finegan, D. P.; Scheel, M.; Robinson, J. B.; Tjaden, B.; Hunt, I.; Mason, T. J.; Millichamp, J.; Di Michiel, M.; Offer, G. J.; Hinds, G.; Brett, D. J.; Shearing, P. R., In-operando high-speed tomography of lithium-ion batteries during thermal runaway. *Nat Commun* **2015,** *6*, 6924.
67. Ebner, M.; Marone, F.; Stampanoni, M.; Wood, V., Visualization and Quantification of Electrochemical and Mechanical Degradation in Li Ion Batteries. *Science* **2013,** *342* (6159), 716-720.
68. Eastwood, D. S.; Bayley, P. M.; Chang, H. J.; Taiwo, O. O.; Vila-Comamala, J.; Brett, D. J. L.; Rau, C.; Withers, P. J.; Shearing, P. R.; Grey, C. P.; Lee, P. D., Three-dimensional characterization of electrodeposited lithium microstructures using synchrotron X-ray phase contrast imaging. *Chemical Communications* **2015,** *51* (2), 266-268.
69. Maire, E.; Withers, P. J., Quantitative X-ray tomography. *Int Mater Rev* **2014,** *59* (1), 1-43.
70. Ota, H.; Shima, K.; Ue, M.; Yamaki, J., Effect of vinylene carbonate as additive to electrolyte for lithium metal anode. *Electrochimica Acta* **2004,** *49* (4), 565-572.

71. Park, H. E.; Hong, C. H.; Yoon, W. Y., The effect of internal resistance on dendritic growth on lithium metal electrodes in the lithium secondary batteries. *J Power Sources* **2008,** *178* (2), 765-768.
72. Bai, P.; Li, J.; Brushett, F. R.; Bazant, M. Z., Transition of lithium growth mechanisms in liquid electrolytes. *Energ Environ Sci* **2016**.
73. Steiger, J.; Kramer, D.; Monig, R., Mechanisms of dendritic growth investigated by in situ light microscopy during electrodeposition and dissolution of lithium. *J Power Sources* **2014,** *261*, 112-119.
74. Lee, Y. M.; Seo, J. E.; Lee, Y. G.; Lee, S. H.; Cho, K. Y.; Park, J. K., Effects of triacetoxyvinylsilane as SEI layer additive on electrochemical performance of lithium metal secondary battery. *Electrochem Solid St* **2007,** *10* (9), A216-A219.
75. Kushima, A.; So, K. P.; Su, C.; Bai, P.; Kuriyama, N.; Maebashi, T.; Fujiwara, Y.; Bazant, M. Z.; Li, J., Liquid cell transmission electron microscopy observation of lithium metal growth and dissolution: Root growth, dead lithium and lithium flotsams. *Nano Energy* **2017,** *32*, 271-279.
76. Wang, S. H.; Yin, Y. X.; Zuo, T. T.; Dong, W.; Li, J. Y.; Shi, J. L.; Zhang, C. H.; Li, N. W.; Li, C. J.; Guo, Y. G., Stable Li Metal Anodes via Regulating Lithium Plating/Stripping in Vertically Aligned Microchannels. *Adv Mater* **2017,** *29* (40).
77. Lu, L. L.; Ge, J.; Yang, J. N.; Chen, S. M.; Yao, H. B.; Zhou, F.; Yu, S. H., Free-Standing Copper Nanowire Network Current Collector for Improving Lithium Anode Performance. *Nano Lett* **2016,** *16* (7), 4431-4437.
78. Zhamu, A.; Chen, G. R.; Liu, C. G.; Neff, D.; Fang, Q.; Yu, Z. N.; Xiong, W.; Wang, Y. B.; Wang, X. Q.; Jang, B. Z., Reviving rechargeable lithium metal batteries: enabling next-generation high-energy and high-power cells. *Energ Environ Sci* **2012,** *5* (2), 5701-5707.
79. Li, Z.; Huang, J.; Liaw, B. Y.; Metzler, V.; Zhang, J. B., A review of lithium deposition in lithium-ion and lithium metal secondary batteries. *J Power Sources* **2014,** *254*, 168-182.
80. Mayers, M. Z.; Kaminski, J. W.; Miller, T. F., Suppression of Dendrite Formation via Pulse Charging in Rechargeable Lithium Metal Batteries. *J Phys Chem C* **2012,** *116* (50), 26214-26221.
81. Jeong, S. K.; Seo, H. Y.; Kim, D. H.; Han, H. K.; Kim, J. G.; Lee, Y. B.; Iriyama, Y.; Abe, T.; Ogumi, Z., Suppression of dendritic lithium formation by using concentrated electrolyte solutions. *Electrochem Commun* **2008,** *10* (4), 635-638.
82. Qian, J. F.; Henderson, W. A.; Xu, W.; Bhattacharya, P.; Engelhard, M.; Borodin, O.; Zhang, J. G., High rate and stable cycling of lithium metal anode. *Nat Commun* **2015,** *6*.
83. Park, M. S.; Ma, S. B.; Lee, D. J.; Im, D.; Doo, S. G.; Yamamoto, O., A Highly Reversible Lithium Metal Anode. *Sci Rep-Uk* **2014,** *4*.
84. Tikekar, M. D.; Archer, L. A.; Koch, D. L., Stability Analysis of Electrodeposition across a Structured Electrolyte with Immobilized Anions. *J Electrochem Soc* **2014,** *161* (6), A847-A855.
85. Lu, Y. Y.; Das, S. K.; Moganty, S. S.; Archer, L. A., Ionic Liquid-Nanoparticle Hybrid Electrolytes and their Application in Secondary Lithium-Metal Batteries. *Adv Mater* **2012,** *24* (32), 4430-4435.
86. Schaefer, J. L.; Yanga, D. A.; Archer, L. A., High Lithium Transference Number Electrolytes via Creation of 3-Dimensional, Charged, Nanoporous Networks from Dense Functionalized Nanoparticle Composites. *Chem Mater* **2013,** *25* (6), 834-839.

87. Basile, A.; Bhatt, A. I.; O'Mullane, A. P., Stabilizing lithium metal using ionic liquids for long-lived batteries. *Nat Commun* **2016,** *7*.
88. Zhang, Y. H.; Qian, J. F.; Xu, W.; Russell, S. M.; Chen, X. L.; Nasybulin, E.; Bhattacharya, P.; Engelhard, M. H.; Mei, D. H.; Cao, R. G.; Ding, F.; Cresce, A. V.; Xu, K.; Zhang, J. G., Dendrite-Free Lithium Deposition with Self-Aligned Nanorod Structure. *Nano Lett* **2014,** *14* (12), 6889-6896.
89. Lu, Y. Y.; Tu, Z. Y.; Archer, L. A., Stable lithium electrodeposition in liquid and nanoporous solid electrolytes. *Nat Mater* **2014,** *13* (10), 961-969.
90. Guo, J.; Wen, Z. Y.; Wu, M. F.; Jin, J.; Liu, Y., Vinylene carbonate-LiNO3: A hybrid additive in carbonic ester electrolytes for SEI modification on Li metal anode. *Electrochem Commun* **2015,** *51*, 59-63.
91. Li, N. W.; Yin, Y. X.; Yang, C. P.; Guo, Y. G., An Artificial Solid Electrolyte Interphase Layer for Stable Lithium Metal Anodes. *Adv Mater* **2016,** *28* (9), 1853-1858.
92. Lee, D. J.; Lee, H.; Song, J.; Ryou, M. H.; Lee, Y. M.; Kim, H. T.; Park, J. K., Composite protective layer for Li metal anode in high-performance lithium-oxygen batteries. *Electrochem Commun* **2014,** *40*, 45-48.
93. Kazyak, E.; Wood, K. N.; Dasgupta, N. P., Improved Cycle Life and Stability of Lithium Metal Anodes through Ultrathin Atomic Layer Deposition Surface Treatments. *Chem Mater* **2015,** *27* (18), 6457-6462.
94. Lee, H.; Lee, D. J.; Kim, Y. J.; Park, J. K.; Kim, H. T., A simple composite protective layer coating that enhances the cycling stability of lithium metal batteries. *J Power Sources* **2015,** *284*, 103-108.
95. Thompson, R. S.; Schroeder, D. J.; Lopez, C. M.; Neuhold, S.; Vaughey, J. T., Stabilization of lithium metal anodes using silane-based coatings. *Electrochem Commun* **2011,** *13* (12), 1369-1372.
96. Umeda, G. A.; Menke, E.; Richard, M.; Stamm, K. L.; Wudl, F.; Dunn, B., Protection of lithium metal surfaces using tetraethoxysilane. *J Mater Chem* **2011,** *21* (5), 1593-1599.
97. Wu, M. F.; Wen, Z. Y.; Liu, Y.; Wang, X. Y.; Huang, L. Z., Electrochemical behaviors of a Li3N modified Li metal electrode in secondary lithium batteries. *J Power Sources* **2011,** *196* (19), 8091-8097.
98. Huang, C.; Xiao, J.; Shao, Y. Y.; Zheng, J. M.; Bennett, W. D.; Lu, D. P.; Saraf, L. V.; Engelhard, M.; Ji, L. W.; Zhang, J. G.; Li, X. L.; Graff, G. L.; Liu, J., Manipulating surface reactions in lithium-sulphur batteries using hybrid anode structures (vol 5, 3343, 2014). *Nat Commun* **2014,** *5*.
99. Zheng, G. Y.; Lee, S. W.; Liang, Z.; Lee, H. W.; Yan, K.; Yao, H. B.; Wang, H. T.; Li, W. Y.; Chu, S.; Cui, Y., Interconnected hollow carbon nanospheres for stable lithium metal anodes. *Nat Nanotechnol* **2014,** *9* (8), 618-623.
100. Fan, L.; Zhuang, H. L. L.; Gao, L. N.; Lu, Y. Y.; Archer, L. A., Regulating Li deposition at artificial solid electrolyte interphases. *J Mater Chem A* **2017,** *5* (7), 3483-3492.
101. Stephan, A. M.; Nahm, K. S., Review on composite polymer electrolytes for lithium batteries. *Polymer* **2006,** *47* (16), 5952-5964.
102. Fergus, J. W., Ceramic and polymeric solid electrolytes for lithium-ion batteries. *J Power Sources* **2010,** *195* (15), 4554-4569.

103. Quartarone, E.; Mustarelli, P., Electrolytes for solid-state lithium rechargeable batteries: recent advances and perspectives. *Chem Soc Rev* **2011,** *40* (5), 2525-2540.
104. Baskakova, Y. V.; Yarmolenko, O. V.; Efimov, O. N., Polymer gel electrolytes for lithium batteries. *Russ Chem Rev+* **2012,** *81* (4), 367-380.
105. Hou, G. M.; Ma, X. X.; Sun, Q. D.; Ai, Q.; Xu, X. Y.; Chen, L. N.; Li, D. P.; Chen, J. H.; Zhong, H.; Li, Y.; Xu, Z. B.; Si, P. C.; Feng, J. K.; Zhang, L.; Ding, F.; Ci, L. J., Lithium Dendrite Suppression and Enhanced Interfacial Compatibility Enabled by an Ex Situ SEI on Li Anode for LAGP-Based All-Solid-State Batteries. *Acs Appl Mater Inter* **2018,** *10* (22), 18610-18618.
106. Yang, C. P.; Liu, B. Y.; Jiang, F.; Zhang, Y.; Xie, H.; Hitz, E.; Hu, L. B., Garnet/polymer hybrid ion-conducting protective layer for stable lithium metal anode. *Nano Res* **2017,** *10* (12), 4256-4265.
107. Zheng, G. Y.; Wang, C.; Pei, A.; Lopez, J.; Shi, F. F.; Chen, Z.; Sendek, A. D.; Lee, H. W.; Lu, Z. D.; Schneider, H.; Safont-Sempere, M. M.; Chu, S.; Bao, Z. N.; Cui, Y., High-Performance Lithium Metal Negative Electrode with a Soft and Flowable Polymer Coating. *Acs Energy Lett* **2016,** *1* (6), 1247-1255.
108. Liu, K.; Pei, A.; Lee, H. R.; Kong, B.; Liu, N.; Lin, D. C.; Liu, Y. Y.; Liu, C.; Hsu, P. C.; Bao, Z. A.; Cui, Y., Lithium Metal Anodes with an Adaptive "Solid-Liquid" Interfacial Protective Layer. *J Am Chem Soc* **2017,** *139* (13), 4815-4820.
109. Zhu, B.; Jin, Y.; Hu, X. Z.; Zheng, Q. H.; Zhang, S.; Wang, Q. J.; Zhu, J., Poly(dimethylsiloxane) Thin Film as a Stable Interfacial Layer for High-Performance Lithium-Metal Battery Anodes. *Adv Mater* **2017,** *29* (2).
110. Li, N. W.; Shi, Y.; Yin, Y. X.; Zeng, X. X.; Li, J. Y.; Li, C. J.; Wan, L. J.; Wen, R.; Guo, Y. G., A Flexible Solid Electrolyte Interphase Layer for Long-Life Lithium Metal Anodes. *Angew Chem Int Edit* **2018,** *57* (6), 1505-1509.
111. Tu, Z.; Choudhury, S.; Zachman, M. J.; Wei, S.; Zhang, K.; Kourkoutis, L. F.; Archer, L. A., Designing Artificial Solid-Electrolyte Interphases for Single-Ion and High-Efficiency Transport in Batteries. *Joule* **2017,** *1*, 394-406.
112. Frisco, S.; Kumar, A.; Whitacre, J. F.; Litster, S., Understanding Li-Ion Battery Anode Degradation and Pore Morphological Changes through Nano-Resolution X-ray Computed Tomography. *J Electrochem Soc* **2016,** *163* (13), A2636-A2640.
113. Verma, P.; Maire, P.; Novak, P., A review of the features and analyses of the solid electrolyte interphase in Li-ion batteries. *Electrochimica Acta* **2010,** *55* (22), 6332-6341.
114. Lee, J. T.; Nitta, N.; Benson, J.; Magasinski, A.; Fuller, T.; Yushin, G., Comparative study of the solid electrolyte interphase on graphite in full Li-ion battery cells using XPS, SIMS, and electron microscopy. *Carbon* **2013,** *23*.
115. Eastwood, D. S.; Bradley, R. S.; Tariq, F.; Cooper, S. J.; Taiwo, O. O.; Gelb, J.; Merkle, A.; Brett, D. J. L.; Brandon, N. P.; Withers, P. J.; Lee, P. D.; Shearing, P. R., The application of phase contrast X-ray techniques for imaging Li-ion battery electrodes. *Nucl Instrum Meth B* **2014,** *324*, 118-123.
116. Shearing, P. R.; Howard, L. E.; Jorgensen, P. S.; Brandon, N. P.; Harris, S. J., Characterization of the 3-dimensional microstructure of a graphite negative electrode from a Li-ion battery. *Electrochem Commun* **2010,** *12* (3), 374-377.

117. Chen-Wiegart, Y. C. K.; Liu, Z.; Faber, K. T.; Barnett, S. A.; Wang, J., 3D analysis of a LiCoO2-Li(Ni1/3Mn1/3Co1/3)O-2 Li-ion battery positive electrode using x-ray nano-tomography. *Electrochem Commun* **2013,** *28*, 127-130.
118. Aurélien Etiemble, A. T., Thierry Douillard, Hassane Idrissi, Eric Maire, and Lionel Roué, Evolution of the 3D Microstructure of a Si-Based Electrode for Li-Ion Batteries Investigated by FIB/SEM Tomography. *J Electrochem Soc* **2016,** *163* (8), A1550-A1559.
119. Lim, C.; Yan, B.; Yin, L. L.; Zhu, L. K., Geometric Characteristics of Three Dimensional Reconstructed Anode Electrodes of Lithium Ion Batteries. *Energies* **2014,** *7* (4), 2558-2572.
120. Jiao, L. A.; Li, X.; Ren, L. L.; Kong, L. Y.; Hong, Y. L.; Li, Z. W.; Huang, X. B.; Tao, X. F., 3D structural properties study on compact LiFePO(4)s based on X-ray computed tomography technique. *Powder Technol* **2015,** *281*, 1-6.
121. Babu, S. K.; Mohamed, A. I.; Whitacre, J. F.; Litster, S., Multiple imaging mode X-ray computed tomography for distinguishing active and inactive phases in lithium-ion battery cathodes. *J Power Sources* **2015,** *283*, 314-319.
122. Ebner, M.; Geldmacher, F.; Marone, F.; Stampanoni, M.; Wood, V., X-Ray Tomography of Porous, Transition Metal Oxide Based Lithium Ion Battery Electrodes. *Adv Energy Mater* **2013,** *3* (7), 845-850.
123. Shearing, P. R.; Brandon, N. P.; Gelb, J.; Bradley, R.; Withers, P. J.; Marquis, A. J.; Cooper, S.; Harris, S. J., Multi Length Scale Microstructural Investigations of a Commercially Available Li-Ion Battery Electrode. *J Electrochem Soc* **2012,** *159* (7), A1023-A1027.
124. Tariq, F.; Yufit, V.; Kishimoto, M.; Shearing, P. R.; Menkin, S.; Golodnitsky, D.; Gelb, J.; Peled, E.; Brandon, N. P., Three-dimensional high resolution X-ray imaging and quantification of lithium ion battery mesocarbon microbead anodes. *J Power Sources* **2014,** *248*, 1014-1020.
125. Gonzalez, J.; Sun, K.; Huang, M.; Lambros, J.; Dillon, S.; Chasiotis, I., Three dimensional studies of particle failure in silicon based composite electrodes for lithium ion batteries. *J Power Sources* **2014,** *269*, 334-343.
126. Chen-Wiegart, Y. C. K.; Shearing, P.; Yuan, Q. X.; Tkachuk, A.; Wang, J., 3D morphological evolution of Li-ion battery negative electrode LiVO2 during oxidation using X-ray nano-tomography. *Electrochem Commun* **2012,** *21*, 58-61.
127. Schroder, D.; Arlt, T.; Krewer, U.; Manke, I., Analyzing transport paths in the air electrode of a zinc air battery using X-ray tomography. *Electrochem Commun* **2014,** *40*, 88-91.
128. Gonzalez, J.; Sun, K.; Huang, M.; Dillon, S.; Chasiotis, I.; Lambros, J., X-ray microtomography characterization of Sn particle evolution during lithiation/delithiation in lithium ion batteries. *J Power Sources* **2015,** *285*, 205-209.
129. Malmgren, S.; Ciosek, K.; Lindblad, R.; Plogmaker, S.; Kühn, J.; Rensmo, H. k.; Edström, K.; Hahlin, M., Consequences of air exposure on the lithiated graphite SEI. *Electrochimica Acta* **2013,** *105*, 83-91.
130. Herstedt, M.; Abraham, D. P.; Kerr, J. B.; Edström, K., X-ray photoelectron spectroscopy of negative electrodes from high-power lithium-ion cells showing various levels of power fade. *Electrochimica Acta* **2004,** *49*, 5097-5110.
131. Kumar, A. S.; Mandal, P.; Zhang, Y. J.; Litster, S., Image segmentation of nanoscale Zernike phase contrast X-ray computed tomography images. *J Appl Phys* **2015,** *117* (18).

132. Abe, K.; Yoshitake, H.; Kitakura, T.; Hattori, T.; Wang, H. Y.; Yoshio, M., Additives-containing functional electrolytes for suppressing electrolyte decomposition in lithium-ion batteries. *Electrochimica Acta* **2004,** *49* (26), 4613-4622.
133. Li, B.; Xu, M. Q.; Li, B. Z.; Liu, Y. L.; Yang, L.; Li, W. S.; Hu, S. J., Properties of solid electrolyte interphase formed by prop-1-ene-1,3-sultone on graphite anode of Li-ion batteries. *Electrochimica Acta* **2013,** *105*, 1-6.
134. Frisco, S.; Liu, D. X.; Kumar, A.; Whitacre, J. F.; Love, C. T.; Swider-Lyons, K. E.; Litster, S., Internal Morphologies of Cycled Li-Metal Electrodes Investigated by Nano-Scale Resolution X-ray Computed Tomography. *Acs Appl Mater Inter* **2017,** *9* (22), 18748-18757.
135. Levi, M. D.; Aurbach, D., The application of electroanalytical methods to the analysis of phase transitions during intercalation of ions into electrodes. *Journal of Solid State Electrochemistry* **2007,** *11* (8), 1031-1042.
136. Chen, L.; Liu, Y.; Ashuri, M.; Liu, C.; Shaw, L. L., Li2S encapsulated by nitrogen-doped carbon for lithium sulfur batteries. *J. Mater. Chem. A* **2014,** *2* (42), 18026-18032.
137. Zhao, M. C.; Kariuki, S.; Dewald, H. D.; Lemke, F. R.; Staniewicz, R. J.; Plichta, E. J.; Marsh, R. A., Electrochemical stability of copper in lithium-ion battery electrolytes. *J Electrochem Soc* **2000,** *147* (8), 2874-2879.
138. Choi, N. S.; Chen, Z. H.; Freunberger, S. A.; Ji, X. L.; Sun, Y. K.; Amine, K.; Yushin, G.; Nazar, L. F.; Cho, J.; Bruce, P. G., Challenges Facing Lithium Batteries and Electrical Double-Layer Capacitors. *Angew Chem Int Edit* **2012,** *51* (40), 9994-10024.
139. Lopez, C. M.; Vaughey, J. T.; Dees, D. W., Morphological Transitions on Lithium Metal Anodes. *J. Electrochem. Soc.* **2009,** *156* (9), A726-A729.
140. Dini, J. W., *Electrodeposition: The Materials Science of Coatings and Substrates*. Noyes Publications: 1993.
141. Daniel, C.; Besenhard, J. O., *Handbook of Battery Materials*. Wiley: 2012.
142. Tsai, W. L.; Hsu, P. C.; Hwu, Y.; Chen, C. H.; Chang, L. W.; Je, J. H.; Lin, H. M.; Groso, A.; Margaritondo, G., Electrochemistry: Building on bubbles in metal electrodeposition. *Nature* **2002,** *417* (6885), 139-139.
143. Hsu, P.-C.; Seol, S.-K.; Lo, T.-N.; Liu, C.-J.; Wang, C.-L.; Lin, C.-S.; Hwu, Y.; Chen, C. H.; Chang, L.-W.; Je, J. H.; Margaritondo, G., Hydrogen Bubbles and the Growth Morphology of Ramified Zinc by Electrodeposition. *Journal of The Electrochemical Society* **2008,** *155* (5), D400-D407.
144. Dedryvère, R.; Laruelle, S.; Grugeon, S.; Gireaud, L.; Tarascon, J. M.; Gonbeau, D., XPS Identification of the Organic and Inorganic Components of the Electrode/Electrolyte Interface Formed on a Metallic Cathode. *Journal of The Electrochemical Society* **2005,** *152* (4), A689.
145. Teng, X.; Zhan, C.; Bai, Y.; Ma, L.; Liu, Q.; Wu, C.; Wu, F.; Yang, Y.; Lu, J.; Amine, K., In Situ Analysis of Gas Generation in Lithium-Ion Batteries with Different Carbonate-Based Electrolytes. *ACS Appl Mater Interfaces* **2015,** *7* (41), 22751-5.
146. Michalak, B.; Berkes, B. B.; Sommer, H.; Bergfeldt, T.; Brezesinski, T.; Janek, J., Gas Evolution in LiNi0.5Mn1.5O4/Graphite Cells Studied In Operando by a Combination of Differential Electrochemical Mass Spectrometry, Neutron Imaging, and Pressure Measurements. *Anal Chem* **2016,** *88* (5), 2877-83.

147. Kozen, A. C.; Lin, C.-F.; Pearse, A. J.; Schroeder, M. A.; Han, X.; Hu, L.; Lee, S.-B.; Rubloff, G. W.; Noked, M., Next-Generation Lithium Metal Anode Engineering via Atomic Layer Deposition. *ACS Nano* **2015,** *9* (6), 5884-5892.
148. Zheng, G.; Lee, S. W.; Liang, Z.; Lee, H. W.; Yan, K.; Yao, H.; Wang, H.; Li, W.; Chu, S.; Cui, Y., Interconnected hollow carbon nanospheres for stable lithium metal anodes. *Nat Nanotechnol* **2014,** *9* (8), 618-23.
149. Zeng, Z.; Liang, W.-I.; Liao, H.-G.; Xin, H. L.; Chu, Y.-H.; Zheng, H., Visualization of Electrode–Electrolyte Interfaces in LiPF6/EC/DEC Electrolyte for Lithium Ion Batteries via in Situ TEM. *Nano Letters* **2014,** *14* (4), 1745-1750.
150. Ota, H.; Sakata, Y.; Otake, Y.; Shima, K.; Ue, M.; Yamaki, J., Structural and functional analysis of surface film on Li anode in vinylene carbonate-containing electrolyte. *J Electrochem Soc* **2004,** *151* (11), A1778-A1788.
151. Lee, C.; Mun, B.; Ross, P. N., The chemical reaction of diethyl carbonate with lithium intercalated graphite studied by X-ray photoelectron spectroscopy. *J Electrochem Soc* **2002,** *149* (10), A1286-A1292.
152. Wang, A. P.; Kadam, S.; Li, H.; Shi, S. Q.; Qi, Y., Review on modeling of the anode solid electrolyte interphase (SEI) for lithium-ion batteries. *Npj Comput Mater* **2018,** *4*.
153. Ue, M.; Sasaki, Y.; Tanaka, Y.; Morita, M., Nonaqueous Electrolytes with Advances in Solvents. In *Electrolytes for Lithium and Lithium-Ion Batteries*, Jow, R. T.; Xu, K.; Borodin, O.; Ue, M., Eds. Springer New York: New York, NY, 2014; pp 93-165.
154. Orvalho, S.; Ruzicka, M. C.; Olivieri, G.; Marzocchella, A., Bubble coalescence: Effect of bubble approach velocity and liquid viscosity. *Chemical Engineering Science* **2015,** *134*, 205-216.
155. Sagane, F.; Ikeda, K.-i.; Okita, K.; Sano, H.; Sakaebe, H.; Iriyama, Y., Effects of current densities on the lithium plating morphology at a lithium phosphorus oxynitride glass electrolyte/copper thin film interface. *Journal of Power Sources* **2013,** *233*, 34-42.
156. Qian, J.; Henderson, W. A.; Xu, W.; Bhattacharya, P.; Engelhard, M.; Borodin, O.; Zhang, J. G., High rate and stable cycling of lithium metal anode. *Nat Commun* **2015,** *6*, 6362.
157. Bieker, G.; Winter, M.; Bieker, P., Electrochemical in situ investigations of SEI and dendrite formation on the lithium metal anode. *Physical Chemistry Chemical Physics* **2015,** *17* (14), 8670-8679.
158. Leenheer, A. J.; Jungjohann, K. L.; Zavadil, K. R.; Sullivan, J. P.; Harris, C. T., Lithium Electrodeposition Dynamics in Aprotic Electrolyte Observed in Situ via Transmission Electron Microscopy. *Acs Nano* **2015,** *9* (4), 4379-4389.
159. Cheng, J.-h.; Assegie, A. A.; Huang, C.-J.; Lin, M.-H.; Tripathi, A. M.; Wang, C.-C.; Tang, M.-T.; Song, Y.-F.; Su, W.-N.; Hwang, B.-J., Visualization of Lithium Plating and Stripping via in operando transmission x-ray microscopy. *J Phys Chem C* **2017**.
160. Tatsuma, T.; Taguchi, M.; Iwaku, M.; Sotomura, T.; Oyama, N., Inhibition effects of polyacrylonitrile gel electrolytes on lithium dendrite formation. *J Electroanal Chem* **1999,** *472* (2), 142-146.
161. Osaka, T.; Homma, T.; Momma, T.; Yarimizu, H., In situ observation of lithium deposition processes in solid polymer and gel electrolytes. *J Electroanal Chem* **1997,** *421* (1-2), 153-156.

162. Meilink, S. L.; Zamanzadeh, M.; Warren, G. W.; Wynblatt, P., Modeling the Failure of Electronic Devices by Dendrite Growth in Bulk and Thin-Layer Electrolytes. *Corrosion* **1988,** *44* (9), 644-651.
163. Nikolic, N. D.; Popov, K. I.; Pavlovic, L. J.; Pavlovic, M. G., Morphologies of copper deposits obtained by the electrodeposition at high overpotentials. *Surf Coat Tech* **2006,** *201* (3-4), 560-566.
164. Tarascon, J. M.; Armand, M., Issues and challenges facing rechargeable lithium batteries. *Nature* **2001,** *414* (6861), 359-367.
165. Wood, K. N.; Kazyak, E.; Chadwick, A. F.; Chen, K. H.; Zhang, J. G.; Thornton, K.; Dasgupta, N. P., Dendrites and Pits: Untangling the Complex Behavior of Lithium Metal Anodes through Operando Video Microscopy. *Acs Central Sci* **2016,** *2* (11), 790-801.
166. Freunberger, S. A.; Chen, Y. H.; Drewett, N. E.; Hardwick, L. J.; Barde, F.; Bruce, P. G., The Lithium-Oxygen Battery with Ether-Based Electrolytes. *Angew Chem Int Edit* **2011,** *50* (37), 8609-8613.
167. Croce, F.; Appetecchi, G. B.; Persi, L.; Scrosati, B., Nanocomposite polymer electrolytes for lithium batteries. *Nature* **1998,** *394* (6692), 456-458.
168. Huang, J. Y.; Zhong, L.; Wang, C. M.; Sullivan, J. P.; Xu, W.; Zhang, L. Q.; Mao, S. X.; Hudak, N. S.; Liu, X. H.; Subramanian, A.; Fan, H. Y.; Qi, L. A.; Kushima, A.; Li, J., In Situ Observation of the Electrochemical Lithiation of a Single SnO2 Nanowire Electrode. *Science* **2010,** *330* (6010), 1515-1520.